Journal of Advanced Ceramics
2023, **12**(5): 873–915
https://doi.org/10.26599/JAC.2023.9220742
ISSN 2226-4108
CN 10-1154/TQ

Review

A review on magneto-optical ceramics for Faraday isolators

Lixuan Zhang[a,b], Dianjun Hu[a,b], Ilya L. Snetkov[c,d], Stanislav Balabanov[e], Oleg Palashov[c,d], Jiang Li[a,b,*]

[a]*Transparent Ceramics Research Center, Shanghai Institute of Ceramics, Chinese Academy of Sciences, Shanghai 201899, China*
[b]*Center of Materials Science and Optoelectronics Engineering, University of Chinese Academy of Sciences, Beijing 100049, China*
[c]*Institute of Applied Physics of the Russian Academy of Sciences, Nizhny Novgorod 603950, Russia*
[d]*Lobachevsky State University of Nizhny Novgorod, Nizhny Novgorod 603950, Russia*
[e]*G.G. Devyatykh Institute of Chemistry of High-Purity Substances, Russian Academy of Sciences, Nizhny Novgorod 603951, Russia*

Received: January 14, 2023; Revised: March 4, 2023; Accepted: March 5, 2023
© The Author(s) 2023.

Abstract: As a promising magneto-optical (MO) material applied in Faraday isolators, magneto-optical ceramics possess excellent comprehensive properties and have attracted much attention these years. Herein, we review the fabrication and properties of magneto-optical ceramics including garnet, sesquioxide, and $A_2B_2O_7$ ceramics. Some of the ceramics have been proved to possess applicable performance, while further studies are still needed for most of the magneto-optical ceramics. Aiming at the application for isolators, the research status, existing problems, and development trends of magneto-optical ceramics are shown and discussed in this review.

Keywords: magneto-optical (MO) ceramics; Faraday isolators; optical quality; thermo-optical effects

1 Introduction

1. 1 Faraday effects and Faraday isolators

When a beam of incident light transmits inside or is reflected at the interface of a material with an intrinsic magnetic moment, the propagation characteristics of the light wave, such as polarization plane, phase, and scattering characteristics will change. This physical phenomenon is called the magneto-optical (MO) effect [1]. MO effects include the Faraday effect [2,3], Kerr effect [4,5], Zeeman effect [6], and Cotton–Mouton effect [7]. To date, the Faraday effect and Kerr effect are the most widely studied and applied MO effects. In 1845, Michael Faraday placed a piece of glass between a pair of magnetic poles and found that after transmitting the glass, the polarization plane of the incident light rotated. This is the first discovery of MO effect, which is then called the Faraday effect. Since the first laser device came out in 1960 [8], the studies on MO materials and devices have developed rapidly.

The Faraday effect is a phenomenon that the polarization plane rotates when linearly polarized light passes through the material along the direction of applied magnetic field (B_0) or magnetization. In the simplest case, at magnetic fields much lower than at the saturation field, the rotation angle can be calculated

* Corresponding author.
E-mail: lijiang@mail.sic.ac.cn

by Eq. (1) [2]:

$$\theta = VBl \tag{1}$$

where θ is the polarization plane rotation angle of the light, V is the Verdet constant, B is the magnetic field intensity, and l is the length of light path passing through the MO material, which usually holds for paramagnetic and diamagnetic materials with magnetic fields of ~1–2 T. At magnetic fields above the saturation field, the dependence on the magnitude of the magnetic field disappears, and the Faraday rotation angle ($\theta_F l$) is determined only by the MO length and rotation angle per unit length [1].

If the diamagnetic term is neglected, the Verdet constant of paramagnetic materials is a function of wavelength and temperature [9].

$$V(\lambda,T) = -B\lambda_0^2/(\lambda^2-\lambda_0^2) - C\lambda_0^2/[(T-T_w)(\lambda^2-\lambda_0^2)] + D/(T-T_w) \tag{2}$$

where λ is the light wavelength, T is the absolute temperature, λ_0 is the transition wavelength, T_w is the Curie–Weiss temperature, and B, C, and D are coefficients. Equation (2) is applicable when the working wavelengths are far from any resonance frequency (optical absorption bands). For the behavior of Verdet constant in absorption lines, the Verdet constant can also be predicted [10,11]; however, the wavelengths with absorptions are unusable for Faraday isolators as a low optical loss is necessary.

For paramagnetic materials, the Verdet constant can be calculated by van Vleck and Hebb [12] and Borrelli [13]:

$$V = (K/T)(N n_{eff}^2/g)\Sigma_n C_n/(\nu^2 - \nu_n^2)^2 \tag{3}$$

where $K = 4\pi^2\mu_B\nu^2/(3chk)$, n_{eff} (= $g[J(J+1)]^{1/2}$) is the effective Bohr magneton, N is the volume concentration of the paramagnetic ions, g is the Lande splitting coefficient, C_n denotes the transition moments, ν is the frequency, ν_n is the frequency corresponding to the splitting of excited states, J is the total angular momentum quantum number, k is the Boltzmann constant, μ_B is the Bohr magneton number, c is the speed of light in vacuum, and h is the Planck constant. According to Eq. (3), the Verdet constant is proportional to N and n_{eff}, which means that the Verdet constant of paramagnetic materials increases with the increasing N. In addition, in order to obtain MO materials with high Verdet constant, the paramagnetic ions should possess high n_{eff}^2/g.

The Faraday effect has been widely used in isolators [14], MO current sensors [15], switches [16–18], modulators [19], and other low-power optical fiber transmission systems for improving the quality of optical signal and resisting interference. Faraday isolators are widely applied based on the nonreciprocity of Faraday effect [20–23]. Figure 1 shows the scheme of a Faraday isolator. In the most simplified case, a free-space (FS) Faraday isolator consists of a polarizer, an MO element placed in magnetic field, and an analyzer. The incident wave passes the polarizer A and becomes a linearly polarized light beam. The green arrows express the direction of the light beam, and the black arrows are the polarization direction. After passing through the MO material under an adjusted magnetic field, the polarization plane of beam rotates 45° and passes the polarizer B (as an analyzer). On the backward path, the light beam has the same rotation direction and rotation angle. As a result, the polarization plane of the light beam is perpendicular to that of the polarizer A, and optical isolation is realized from the Malus' law.

$$I = I_0\exp(-\alpha l)\cos^2(\beta \pm \theta_F l) \tag{4}$$

where I is the output intensity of the light beam, I_0 is

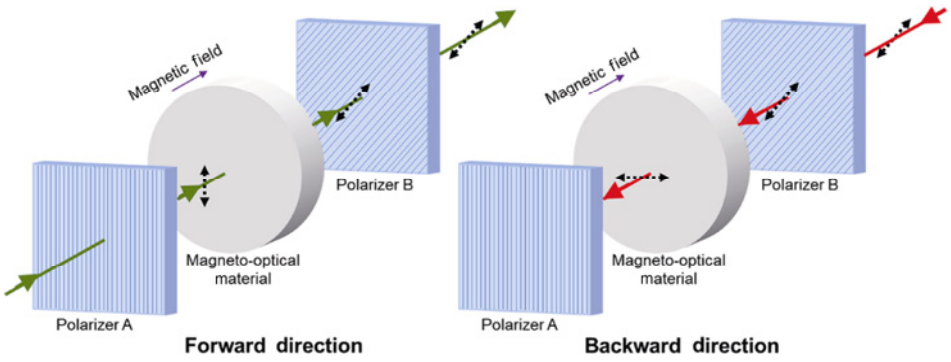


Fig. 1 Structure diagram of optical isolator.

the incident intensity, α is the optical absorption coefficient, l is the length of MO material, β is the included angle of the polarizer and analyzer, and θ_F is the Faraday rotation angle per unit length. As a result, $\theta_F l$ is the Faraday rotation angle. In the case of FS Faraday isolators, $\beta = \theta_F l = 45°$; hence for the forward transmission, $I_F = I_0 e^{-\alpha l}$, and for the backward transmission, $I_B = 0$.

With the rapid development of laser materials and laser systems in recent years [24–28], the output power is increasing day by day in laser devices. High-power lasers have broad application prospects, including laser processing [29], scientific research (e.g., gravitational wave detection [30]), inertial confinement fusion (ICF) [31], and laser weapon [32,33]. In the case of high-output-power laser, the back-reflected beam could damage the front-end system destructively, including the resonator and seed source [34,35]. Accordingly, the research and design of MO materials and Faraday isolators is much-anticipated, especially the devices with excellent performance under high power.

1. 2 Magneto-optical materials for Faraday isolators

As the core components in the Faraday isolators, MO materials have been researched widely. MO glasses, MO single crystals, organic soft MO materials, and MO ceramics are now most discussed MO materials. Each kind of material has its advantages and weaknesses. MO glasses and MO crystals have developed earlier and have mature preparation technology, while others are still in the stage of research. Though still under development, MO ceramics have got great attention and are highly expected to be put into the practical application in the foreseeable future.

MO glass is one of the earliest used MO materials owing to its high optical quality and excellent dimensional scalability [36,37]. By doping Pb^{2+}, Sb^{3+}, Te^{4+}, Bi^{3+}, or Tl^{+}, the glasses show diamagnetic [38–41], but their Verdet constants are small, and thus the diamagnetic glasses are unfavorable for application; by doping paramagnetic ions like Pr^{3+}, Ce^{3+}, Nd^{3+}, Tb^{3+}, Dy^{3+}, Ho^{3+}, Er^{3+}, and Yb^{3+}, the glasses show paramagnetism, and the value of the Verdet constant is higher than those of the diamagnetic glasses [42–46]. From Eq. (3), choosing ions with high n_{eff}^2/g like Tb^{3+}, Dy^{3+}, Ho^{3+}, and Er^{3+} and increasing the concentration of them as much as possible are effective ways to improve the Verdet constant of paramagnetic glasses. It is noteworthy that the absorption band of doping ions should be considered. MO glasses with a certain doping ion have a certain application wave band, e.g., the absorption peaks of Ho^{3+} are located at 2000, 642, 540, 491, 477, 461, 457, 447, 421, and 361 nm. Ho^{3+}-doped MO glasses therefore cannot be applied in these certain wavelengths. Limited by the doping concentration on the premise of ensuring high optical quality, improving the Verdet constant of glasses is difficult [47–49]. Besides, the Verdet constant is greatly affected by temperature in paramagnetic glasses, and the thermal conductivity (k) of glasses is low. Though glasses have been applied in isolators owing to their high optical quality and reasonable cost, the demand of high-performance Faraday isolators is still challenging to be satisfied for glasses.

Single crystals have been applied in Faraday isolators for many years as well. MO crystals can possess higher Verdet constants and better thermal properties compared with glasses due to the crystal structure with higher concentrations of paramagnetic ions. In addition, the laser damage threshold of crystals can be higher than those of glasses, so MO crystals are promising candidate materials for high-performance Faraday isolators [50,51], such as $Tb_3Ga_5O_{12}$ (TGG) [52], $Tb_3Sc_2Al_3O_{12}$ (TSAG) [53–55], KTb_3F_{10} (KTF) [56,57], $LiTbF_4$ (TLF) [58], CeF_3 [49,59–61], and PrF_3 [62]. TGG crystals are widely discussed and applied in these years as they possess high Verdet constants (-136 rad·T^{-1}·m^{-1} at 633 nm and -38 rad·T^{-1}·m^{-1} at 1064 nm), wide transparent bands (500–1500 nm), and high thermal conductivity (4.5 W·m^{-1}·K^{-1}) [2,14,49,52, 63,64]. Though MO crystals have occupied major markets, the fabrication of MO crystals is facing many problems [65–74], including component volatilization, incongruent melting, high melting point, phase transition, time-consuming, size limitation, and cracking.

There emerged new soft MO materials recently by fabricating novel molecular, polymetric, and nanocomposite materials [75], including organic small molecules [76–78], conjugated polymers [79–82], ferrofluids [83], and polymer-magnetic nanoparticle nanocomposites [84–86]. Soft MO materials offer distinctive advantages from classical inorganic materials, so they show interesting potential for the application in Faraday isolators. However, a lack of established fundamental material physics leads to difficulties in material design. Though high Verdet constants have been reported in many soft MO materials, the service-

concerned performance except Verdet constant is rarely mentioned, and their comprehensive performance is still not enough for the device requirements, e.g., the optical quality and thermal properties. So, soft MO materials have not been widely developed and are still far from the practical application.

As a kind of new and developing material, transparent ceramics attracted much attention, and paramagnetic MO ceramics possess most of the excellent properties of MO crystals [87–93]. The Verdet constant, thermal conductivity, thermo-optical properties, and laser damage threshold of MO ceramics are almost equal to those of the crystals with the same composition. What is more, by using the fabrication method of transparent ceramics, it is possible to obtain incongruent melting and high-melting-point materials [94–98], which greatly expands the range of MO material selection. Unlike the difficulty in obtaining large size MO crystals, the size of the ceramics is limited only by the size of the available equipment in theory. Ceramic fabrication equipment is standardized and suitable for the fabrication of ceramics from different materials, and the fabrication method allows scale-up production and moves to mass production of MO elements. All these advantages make MO ceramics a new competitive candidate for the application in high-performance Faraday isolators. To date, garnet, sesquioxide, and $A_2B_2O_7$ ceramics are widely studied and have been proved to possess high optical quality and Verdet constants, so they are considered potential materials for Faraday isolators. Besides, there were some studies of MO ceramics with other structures, such as ZnSe [35], MgO [99], and $Cd_{0.55}Mn_{0.45}Te$ [100]. However, due to the low Verdet constants of ZnSe and MgO polycrystalline ceramics, large effective length and strong magnetic field are needed, which may increase the complexity of the devices. For other ceramics with high Verdet constants like $Cd_{0.55}Mn_{0.45}Te$ ceramics, the high optical loss makes it not well suited for Faraday isolators. Therefore, garnet, sesquioxide, and $A_2B_2O_7$ ceramics will be mainly discussed in this paper as they possess both good MO properties and high optical quality.

1. 3 Important parameters of magneto-optical ceramics for Faraday isolators

For the application of Faraday isolators, there are several important parameters for MO ceramics, including Verdet constant, optical loss, extinction ratio (I), thermal conductivity, thermo-optical constant, thermally induced depolarization property, magneto-optical figure of merit (FoM), and laser-induced damage threshold.

From Eq. (1), it is clear that we can adjust V, B, and l to achieve the 45° rotation. As long MO materials bring adverse effect such as higher optical loss, more complex system, more severe thermal lens, and thermally induced depolarization of radiation, we can adjust B and l to satisfy the rotation requirement. Enhancing the magnetic field by increasing the dimensions of the magnetic system is not a wise choice because of the logarithmic dependence of the maximum attainable field on the ratio of the outer and inner magnet diameters [101,102]. Finally, choosing MO ceramics with higher Verdet constants is a more optimal way to meet the 45° rotation and shorten the length of MO element. So, the Verdet constant is one of the most important parameters for MO materials.

In high-power laser systems, the optical quality is strictly required. For practical use, MO ceramics should possess low scattering loss and high optical uniformity to preserve the quality and power of the transmitted radiation and low absorption loss to avoid thermally induced effects. Optical quality also affects the extinction ratio, which is a key parameter to evaluating the ability of MO materials to shut down the return wave: The MO material is placed between two parallel polarizers, the light beam passes from one polarizer to another, and the output power is P_1; similarly, the MO material between two perpendicular polarizers is put, and the output power is P_2. The I is defined as

$$I = 10\lg(P_1/P_2) \tag{5}$$

where P_1/P_2 is also called the depolarization ratio (γ).

Because of the absorption loss and high laser power (P_{las}) under the practical condition, MO material is nonuniformly heated. This results in the thermal stress, and hence the thermally induced depolarization arises (especially from the piezo-optic effect). For the rotation angle (φ), thermally induced depolarization in a cubic MO material can be calculated by Eq. (6) [103,104]:

$$\gamma = (A/8)(\sin\varphi^2/\varphi^2)\alpha Q L P_{las} X/(\lambda\kappa) \tag{6}$$

where A is a coefficient dependent on the laser beam spatial profile, λ is the wavelength of the laser beam, κ is the thermal conductivity of the MO material, Q is the thermo-optical constant, L is the length of the MO material, and X is a function of crystallographic axis orientation (for the case of single crystal; for ceramics,

$X = (2 + 3\xi)/5$, where ξ is the piezo-optical anisotropy parameter). From Eq. (6), we can know that ideal MO materials should possess low α, low Q, and high κ. In addition, the Verdet constant changes as the temperature changes, which means that the Verdet constant is not uniform in the MO ceramics when heated, so this effect also contributes to the thermally induced depolarization. But in most cases, the contribution is significantly less than that from thermally induced depolarization. Thermal lens is another effect originating from the temperature gradient in MO ceramics, which leads to the wave front distortions. The optical power (D) of the arising thermal lens may be calculated by Eq. (7) [104]:

$$D = 1/F = [L\alpha P_{las}/(2\pi r_h^2 \kappa)][P - S(1 - \xi)Q] \quad (7)$$

where F is the focal length, P is the thermo-optical constant responsible for thermal lens, r_h is the laser beam radius, and S is the orientation-dependent constant. Thermal lens effect does not cause pronounced polarization distortions, but it introduces power dependent aberrations to the laser radiation [52]. Vojna *et al*. [49] summarized the simplified physical phenomena involved in the absorption-induced thermal effects in magneto-active media, as shown in Fig. 2. It is clear that the thermal effect originated from the light absorption will deteriorate the performance of Faraday isolators in various ways.

For comparison and classification of MO materials, FoM is used as a rule. FoM was first introduced in the form of FoM = V/α_0, where α_0 is the linear absorption coefficient; however, in this form, it does not allow a correct assessment of a possible isolation ratio provided by FI at a high average power, as only linear absorption of material is taken into account. In order to take this into account, FoM is defined as [101]:

$$\mu = \begin{cases} \left|\dfrac{Vk}{\alpha Q}\right|, & |\xi| \geqslant 1 \\ \left|\dfrac{Vk}{\alpha Q\xi}\right|, & |\xi| < 1 \end{cases} \quad (8)$$

where μ is the FoM related to the photo-elastic effect. FoM takes the Verdet constant, thermal conductivity, absorption coefficient, thermo-optical constant, and piezo-optical anisotropy ratio into account to fully assess MO materials. Higher μ indicates better performance as a Faraday rotator. In this form, the FoM value is inversely proportional to the minimum of the root of thermally induced depolarization in the [001] orientation caused by the photo-elastic effect. This classification gives the correct result for MO materials with $\xi > 0$ [105]. The critical power (P_{max}) is a more suitable parameter for theoretical comparison of any MO materials (arbitrary ξ), but more complicated to calculate. For the known analytical dependence of γ_{min} on laser power, by specifying the value of B_0, one can find that $P_{las} = P_{max}$, at which $\gamma = 0.001$ ($I = 30$ dB) [101]. Since, on average, thermally induced effects in ceramics behave like in isotropic medium (glass), Eq. (8) can be used as an FoM up to the replacement of the thermo-optical characteristic Q to $Q_{eff} = Q(2 + 3\xi)/5$ (or that determined experimentally [106]).

When the laser with high power acts on the MO material, it will be damaged and even cracked in the worst cases. For MO materials applied in high-power laser systems, it is important to evaluate the laser damage performance. The laser-induced damage threshold is a limitation, at which a material will be damaged by a laser given the fluence, intensity, and wavelength. For MO ceramics, laser-induced damage threshold depends on the basic properties of ceramics, as well as the microstructure, interior defect, and surface flaw.

To summarize, ideal MO ceramics should possess high Verdet constant, low optical loss, high extinction ratio, high thermal conductivity, low thermo-optical constant, high magneto-optical FoM, high laser-induced damage threshold, small polarization distortion, and slight effect on the beam quality when operating at

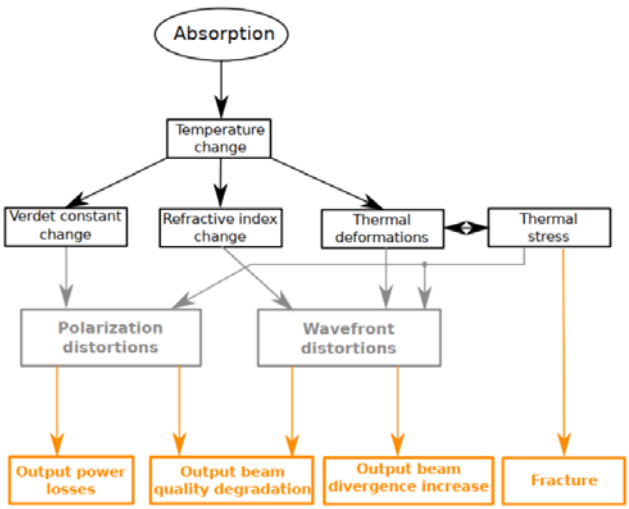


Fig. 2 Scheme of physical phenomena involved in the absorption-induced thermal effects in magneto-active media. Reproduced with permission from Ref. [49], © the authors 2019.

high-power laser. These important parameters are not only determined by the intrinsic physical properties of materials, but also depend on the fabrication technology. For MO ceramics, the fabrication technology is of great significance as the optical quality is almost entirely depends on the fabrication process. The scattering and absorption sources in MO ceramics reduce the extinction ratio and degrade the output beam quality seriously. The studies to date suggest that optical quality is in the first place for high-performance Faraday isolators.

In this paper, we update the reviews of the recent progress in MO ceramics, especially in garnet-based, sesquioxide, and $A_2B_2O_7$ ceramics. Aiming at the application in high-performance Faraday isolators, we summarized current results and difficulties in fabricating high-quality MO ceramics. The summaries will help researchers with further fabrication and study of MO ceramics.

2 Garnet-based magneto-optical ceramics

2. 1 TGG-based ceramics

2.1.1 TGG ceramics

TGG is a cubic garnet crystal with a space group of *Ia*-3*d*. Tb^{3+} occupies the dodecahedron sites, and Ga^{3+} occupies the tetrahedron sites and octahedron sites. As an MO material used in 400–1400 nm, TGG single crystal has been widely studied and applied for its higher Verdet constant and higher thermal conductivity compared with Tb-doped glasses [52,63,107–109]. To overcome the volatilization of Ga_2O_3 and to expand the aperture, TGG ceramics were fabricated and discussed. In 2003, Khazanov [110] forecasted the possibility and performance of TGG ceramics applied in Faraday isolator. The first TGG ceramics were fabricated by Ikesue *et al*. [3,93] reported in 2003, but the optical quality is not good enough for Faraday isolators. In 2004, Kagan and Khazanov [103] further developed a model and analyzed the thermally induced birefringence in polycrystalline ceramics. The result showed that the performance of TGG ceramics is almost equivalent to that of a [111]-oriented TGG single crystal if the ratio of the rod length to the grain size is larger than 300 in ceramics up to the change of ξ.

In 2007, Yasuhara *et al*. [111] measured the temperature dependence of the Verdet constant of TGG ceramics. At room temperature, the Verdet constant of TGG ceramics is 36.4 $rad \cdot T^{-1} \cdot m^{-1}$, which is the same as that of TGG single crystals. The Verdet constant increases with the decrease of temperature, and the Verdet constant of TGG ceramics is 87-time magnitude at liquid helium temperature compared with that at room temperature. The thermal conductivity of TGG ceramics was measured to be about 4.94 $W \cdot m^{-1} \cdot K^{-1}$ at room temperature, which is the same as that of TGG single crystal and is one-order higher than those of glass materials. The measured TGG ceramic sample is provided by Konoshima Chemical Co. Ltd., and the size is 5.95 mm in length and 5 mm × 1 mm in cross section. However, the optical quality of the sample is not reported. In 2011, Yoshida *et al*. [112] reported the optical properties and Faraday effect of TGG ceramics. The TGG ceramic samples with the size up to 20 mm in length and 5 mm × 5 mm in cross section (provided by Konoshima Chemical Co. Ltd.) were fabricated by slip casting and vacuum sintering. The wave-front distortion of the TGG ceramic sample (3 mm in length and 10 mm × 10 mm in cross section) was $\lambda/12$ at 632 nm. The optical in-line transmittance of the TGG ceramics and crystal was nearly equal to above 600 nm, proving the high optical quality of TGG ceramics. The optical scattering coefficients of TGG ceramics and single crystal were measured to be both 5×10^{-4} cm^{-1} at 1064 nm, but the optical scattering coefficient of TGG ceramics at 633 nm was 2.4 times that of single crystal (2.4×10^{-3} cm^{-1} vs. 1×10^{-3} cm^{-1}). The extinction ratio of TGG ceramics was more than 35 dB at 1064 nm, which was similar to that of the commercial TGG single crystals. The laser-induced damage threshold of TGG ceramics at 1064 nm was measured to be 2.3–5.1 $J \cdot cm^{-2}$ at 5 ns, comparable with that of TGG single crystal (5 $J \cdot cm^{-2}$ at 10 ns). This study proves that TGG ceramics possess good comprehensive performance and can be applied in Faraday isolators. Yasuhara and Furuse [113] then reported the thermally induced depolarization in TGG ceramics with 28 mm in length and 7 mm in diameter (from Konoshima Chemical Co. Ltd.). The results showed that the thermally induced depolarization of the TGG ceramic sample (γ = 6.1×10^{-4} when P = 117 W at 1030 nm) was comparable to that of commercially available TGG crystals. From the values of optical absorption coefficient and thermal expansion coefficient, the thermo-optical properties of TGG ceramics are nearly equal to those of high-quality TGG single crystal. Yasuhara *et al*. [114] also evaluated the temperature dependence of the thermo-optical

coefficient and the linear thermal expansion coefficient in single crystal and TGG ceramics. The results quantitatively substantiated the decrease of thermal birefringence and thermal lens effect in TGG ceramics at cryogenic temperature. A more comprehensive evaluation of the thermally induced depolarization, thermal lens effect, and stability of TGG-based Faraday rotator at high average laser power was studied by Yasuhara *et al*. [115] in 2014. The sample was a 9.15 mm long TGG ceramic rod, fabricated by Konoshima Chemical Co. Ltd. The results showed that the rotator maintained an extinction ratio of 30 dB up to 340 W, and this result was nearly the same as that of the TGG single crystals. For thermal lens effect, F = 9.5 m was estimated at a laser power of 257 W, and F = 4 m at the laser power of 600 W. This thermal lens effect can be compensated by a spherical lens system and is acceptable for a Faraday rotator working at the 600 W level.

To maintain the isolation ratio at high laser power, reducing the impact of thermally induced depolarization by external compensation is a practicable way [116]. In 2014, Snetkov *et al*. [117] used an additional optical element to compensate the thermally induced depolarization of a Faraday isolator with an MO element made of TGG ceramics (produced by Konoshima Chemical Co. Ltd.). Two additional optical elements were made of TGG single crystal and TGG ceramics, and the additional optical element was put outside magnetic field. At the laser power of 300 W, the addition of a TGG ceramic compensator allows a 5–6-fold reduction of thermally induced depolarization, and hence the power can be elevated to 900 W retaining the isolation ratio of 30 dB. In addition, by choosing optimal additional optical element parameters [116,118], it is possible to enhance the laser power up to 2 kW. Yasuhara *et al*. [119] used two 7-mm-long TGG ceramics as the MO element. The isolation ratio of 35 dB was maintained at 740 W, and it was calculated that an isolation ratio better than 30 dB at 2.7 kW can be achieved. The F of the two 7-mm TGG ceramic rods was 0.8 m with a beam radius of 0.58 mm at 400 W. The calculation results showed that when the laser power was elevated to 2.7 kW, F = 0.6 m, which could be compensated easily. In addition, the thermal lens effect can be mitigated at a larger beam diameter. Figure 3 shows the TGG ceramic sample made by Konoshima Chemical Co. Ltd. with an area greater than 100 mm × 100 mm.

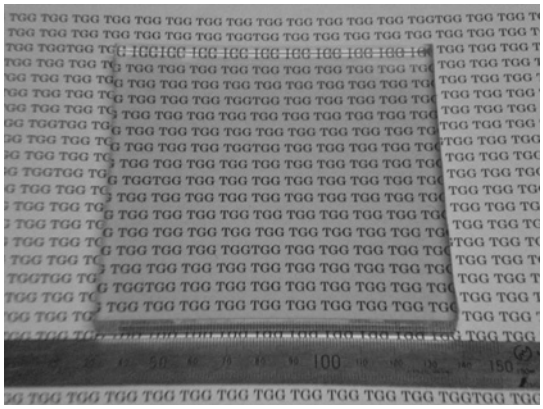


Fig. 3 TGG ceramic sample made by Konoshima Chemical Co. Ltd. Reproduced with permission from Ref. [119], © AIP Publishing LLC. 2014.

Konoshima Chemical Co. Ltd. has succeeded in the fabrication of high-quality TGG ceramics, and the isolation under high-energy laser has been proved. However, the fabrication process of these TGG ceramics was not reported in detail. Many studies have been carried out to investigate the specific preparation process and further improve the optical quality of TGG ceramics. Feng *et al*. [120] reported TGG ceramics fabricated by the solid-state reaction method in 2015. The TGG ceramics sintered at 1550 ℃ for 20 h possess the best optical quality. The in-line transmittance of the TGG sample with 1 mm in thickness was close to 72% from 500 to 1500 nm. The TGG ceramics were covered by a yellow shell after vacuum sintering due to the volatilization of Ga_2O_3, if the mixed powders were not calcined in a muffle furnace to form TGG phase. However, the process, calcining the mixed powders into TGG phase, seems not suitable as the obtained ceramic sample is opaque.

The co-precipitation method is a good way to synthesize nano-powders for preparing high-quality transparent ceramics [121–132]. Li *et al*. [133–135] fabricated TGG ceramics from co-precipitated nano-powders. They used a novel two-step sintering method, which was sintering the ceramics in air combined with hot isostatic pressing (HIP) post-treatment in argon. As the powders are TGG phase, and the ceramics are pre-sintered in air, the volatilization of Ga_2O_3 is mostly avoided. The parameters (calcination temperature and amount of precipitant) of synthesizing nano-powders and the pre-sintering temperature were investigated in detail. Though the precursor was agglomerated, after optimization and calcination, the particle size of TGG powders is less than 200 nm with good homogeneity

and dispersion, as shown in Figs. 4(a) and 4(b). The TGG ceramics pre-sintered at 1500 ℃ for 3 h in air reached a relative density of 95.1%, and then reached fully dense with an average gran size of 2.5 μm after HIP post-treated at 1550 ℃ for 3 h under a 150-MPa Ar atmosphere, as shown in Figs. 4(c) and 4(d), respectively. HIPed TGG ceramics pre-sintered at 1500 ℃ possess the highest in-line transmittance, which is 80.3% at 1064 nm (1.2 mm thick), as seen in Figs. 4(e) and 4(f). The Verdet constant of the samples is about −136.8 rad·T^{-1}·m^{-1} at 633 nm, and the Verdet constant is hardly affected by the optical quality. Note that the required length of TGG ceramics is 20 mm if applied at 1064 nm and under 1 T magnetic field, so the obtained TGG ceramic samples in Refs. [120,133–135] can hardly meet the requirement for a Faraday isolator.

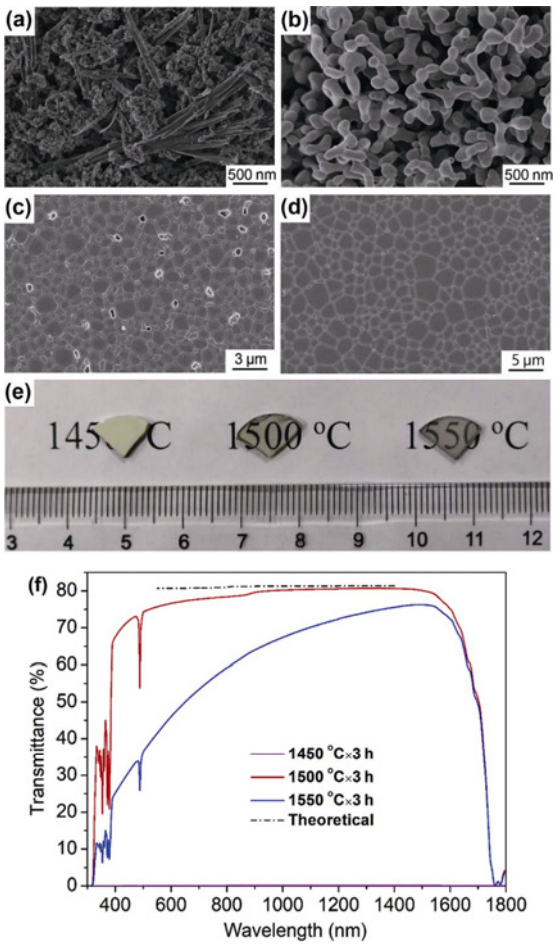


Fig. 4 Field-emission scanning electron microscopy (FESEM) micrographs of (a) as-synthesized precursor, (b) powders calcined at 1100 ℃, and TGG ceramics (c) pre-sintered at 1500 ℃ and (d) after HIP post-treatment; (e) photographs and (f) in-line transmittance of TGG ceramics. Reproduced with permission from Ref. [133], © Elsevier B.V. 2018.

Existing studies have confirmed that TGG ceramics are highly promising MO materials for Faraday isolators used in lasers with high energy. Further studies may focus on the optimization of optical quality and the enlarging of size. Though many efforts [120,133–137] have been made, there is no report about TGG ceramic samples with better performance compared with the samples fabricated by Konoshima Chemical Co. Ltd. so far as we know. As a developed MO material with almost the best comprehensive performance currently, there are still disadvantages and limitations for TGG, e.g., the Verdet constant is not high enough, and the maximum laser power that can be isolated with an isolation ratio of 30 dB (P_{max}) is inadequate for high-performance Faraday isolators. Therefore, there emerge advanced MO materials with higher Verdet constants and better thermo-optical properties. In addition, as TGG single crystals and ceramics can work only in 400–1400 nm (except the absorption peak), many MO materials with other application wave band are under study.

2.1.2 Rare-earth (RE):TGG ceramics

It has been found that doping RE ions like Dy^{3+} [138], Tm^{3+} [139], Pr^{3+} [140], Ce^{3+} [141], Ho^{3+} [142], and Nd^{3+} [143] in TGG crystals brought an increase of Verdet constant, and a similar phenomenon was also reported in TGG ceramics [144,145]. The increase of the Verdet constant is likely explained by the structural variation, magnetization dependence on the splitting of the ground configuration induced by the spin−orbit interaction, crystal field, exchange interaction, and external magnetic field [139,146]. However, there is still no evidence to prove the mechanism clearly. In 2021, Li *et al*. [145] fabricated 1.0 at% RE:TGG (RE = Pr, Tm, and Dy) ceramics by air sintering and HIP post-treatment using co-precipitated nano-powders as the raw material. GeO_2 was added as the sintering aid. The in-line transmittance of the TGG ceramics is higher than 80% at 1070 nm (1.5 mm thick), and the Verdet constant of the RE:TGG is about −143 rad·T^{-1}·m^{-1} at 632.8 nm, which is about 5% higher than that of the undoped TGG ceramics. Though the RE:TGG ceramics possessed higher Verdet constants, the thermally induced depolarization results showed that the undoped TGG ceramics after annealing possessed the best performance: The maximum power was 0.8 kW with a 30 dB extinction ratio, as shown in Fig. 5. The increased optical absorption coefficient and the decreased thermal

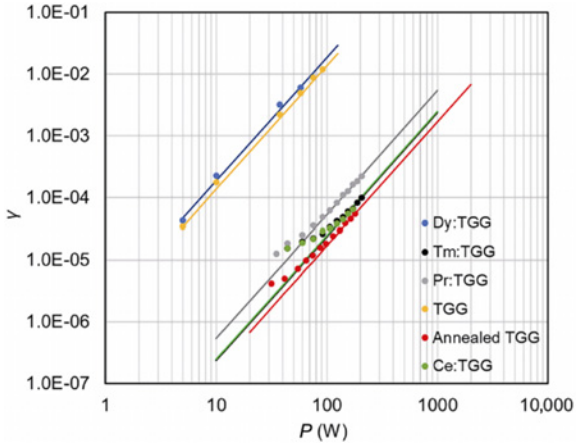


Fig. 5 Experimental (dots) and theoretical (lines) dependence of integral thermally induced depolarization on P_{las} in RE:TGG ceramics. Reproduced with permission from Ref. [145], © The Author(s) 2020.

conductivity of RE:TGG may deteriorate the thermally induced depolarization performance. It is noteworthy that the Verdet constant in TGG ceramics has lower improvement in Ref. [145] compared with the improvement of that in TGG single crystals after doping Dy^{3+} [138], Tm^{3+} [139], and Pr^{3+} [140] (increase by 30%, 30%, and 46%, respectively). To our knowledge, the thermal–optical performance of doped TGG single crystals has not been studied yet. According to the current research, there is still a question remaining uncertain that whether doping will improve the performance of TGG ceramics and crystals.

2. 2 Terbium aluminum garnet ($Tb_3Al_5O_{12}$, TAG)-based ceramics

2.2.1 TAG ceramics

TAG is a promising MO material working in 400–1400 nm of waveband due to its higher Verdet constant (about −176 rad·T^{-1}·m^{-1} at 633 nm [66,69]) and higher thermal conductivity (7.13 W·m^{-1}·K^{-1} at 293 K [69]) compared with those of TGG material and other good thermal–optical performance. So, TAG material is considered to be one of the best alternative materials for high-performance Faraday isolators. But unfortunately, TAG is an incongruent melting material [65], which means that the fabrication of TAG single crystals is very difficult. In 2001, Ganschow *et al*. [147] obtained micro-crystal TAG with 0.7 mm in diameter and up to 100 mm in length using the micro-pulling-down technique. The samples exhibited a homogeneous core, but the core was surrounded by a defective shell with alumina precipitations and eutectic inclusions. Geho *et al*. [66,148] fabricated a TAG single crystal with a diameter of 3 mm using the floating zone method. Refractive indices at various wavelengths were fitted. If the Fresnel reflection was removed on the two edges, the transmittance of TAG single crystal sample with 3 mm in length was over 95% from 500 to 1300 nm, and was 90% at 400 nm. The optical loss was considered to be the result of inhomogeneity. Ikesue and Aung [149] fabricated the $(Lu_{0.1}Tb_{0.9})_3Al_5O_{12}$ single crystal with high optical quality by a solid-state crystal growth (SSCG) method. While the sample thickness (t) was 7 mm, the Verdet constant was slightly lower than that of TAG. Liu *et al*. [69] used an improved edge-defined film-fed method to grow TAG single crystals with centimeter sizes, which is the largest TAG single crystal currently known. Above these, though many efforts have been made, the aperture, length, or optical loss of TAG single crystals still cannot meet the application requirements for Faraday isolators, especially in the high-power condition. As melting of the raw materials is not needed in the fabrication process of TAG transparent ceramics, the phase separation due to the incongruent melting can be avoided nicely. Hence, TAG ceramics have caught great attention and have been widely studied these years.

In 2011, Lin *et al*. [150] from Shanghai Institute of Optics and Fine Mechanics (SIOM) first reported the fabrication and properties of TAG ceramics, which were prepared by solid state reaction and vacuum sintering. Tetraethyl orthosilicate (TEOS) was used as the sintering aid. The in-line transmittance of TAG ceramics was close to 70% from 500 to 1500 nm (2.4 mm thick), and the thermal conductivity at room temperature was measured to be 6.5 W·m^{-1}·K^{-1}, which was higher than that of TGG single crystals. The Verdet constant of TAG ceramics at 632.8 nm was measured to be −173 rad·T^{-1}·m^{-1}, close to the values of TAG single crystals and 28.9% higher than those of TGG crystals and ceramics. When TAG ceramics are applied at 1064 nm and under 1 T magnetic field, the length of only 14 mm is needed, which is shortened by 30% compared with that of TGG. Though the improvement of the sample optical quality and sample size is needed, this work confirms the feasibility of TAG ceramics as one of the alternative materials for TGG crystals. In the next few years, a large number of studies have been carried out on the sintering aids (including SiO_2 and MgO [151–153], CeO_2 [154], ZrO_2

[155,156], and TiO_2 [157]), component optimization [158], phase and microstructure evolution [159–161], morphology of raw powders [162], and sintering method [159] for preparing TAG ceramics by the solid state reaction sintering method. Zheleznov *et al*. [163] measured the thermal–optical performance of TAG ceramics provided by SIOM. TAG ceramics with 7–15 mm in diameter and 3–4 mm in thickness were fabricated by solid state reaction and vacuum sintering. 0.4 wt% TEOS and 0.09 wt% MgO were added as the sintering aid. The Faraday isolator based on the TAG ceramics provided a stable isolation ratio of 38 dB at 300 W laser power (1070 nm), which was prior to that of TGG ceramics because the TAG sample had a higher Verdet constant (thus shorter required length), higher conductivity, and was likely to have a lower absorption coefficient. The F was predicted to be 8 m at 300 W, which was able to be compensated by a system of spherical lenses.

The co-precipitation method combined with sintering technology is another way to fabricate TAG ceramics. Dai *et al*. [164–166] from Shanghai Institute of Ceramics, Chinese Academy of Sciences (SICCAS) firstly reported the TAG ceramics fabricated from co-precipitated TAG nano-powders. They studied the decomposition process of TAG precursor. The influence of calcination temperature and R value (precipitant to the metal-ion molar ratio, $n(NH_4HCO_3)/n(M^{3+})$) on the properties of the powders and ceramics were systematically investigated. The particle size of the obtained TAG nano-powders was smaller than 100 nm after optimization, as shown in Fig. 6(a). After ball milling, adding sintering aid, sintering, and HIP post-treatment, the obtained TAG ceramics reached full-dense and showed the transmittance of 81.4% at 1064 nm, which was close to the theoretical transmittance of TAG (82.4%), as shown in Figs. 6(b)–6(d). Li *et al*. [167,168] further investigated the influences of sintering parameter, sintering aid, and chemical composition on the optical quality and microstructure of TAG ceramics. After their optimization, the in-line transmittance of TAG ceramics with a thickness of 1.7 mm reached 82.6% at 1064 nm, as shown in Fig. 6(e).

In 2017, Aung and Ikesue [169] reported optical-grade $(Tb_xY_{1-x})_3Al_5O_{12}$ (x = 0.5–1.0) ceramics with multiple sizes. These ceramics were fabricated by the solid-state reaction method. The raw powders and colloidal silica (as the sintering aid) were mixed and spray dried. After vacuum sintering and HIP treatment, the $(Tb_xY_{1-x})_3Al_5O_{12}$ (x = 0.5–1.0) ceramics showed high transparency. The measured transmittance of $(Tb_{0.6}Y_{0.4})_3Al_5O_{12}$ and TAG ceramics were almost their theoretical transmittance at 1064 nm, as shown in Fig. 7(a). Considering the large t of 11 mm, the optical loss of these ceramics was estimated to be less than 0.1% cm^{-1}, which was much smaller than that of the

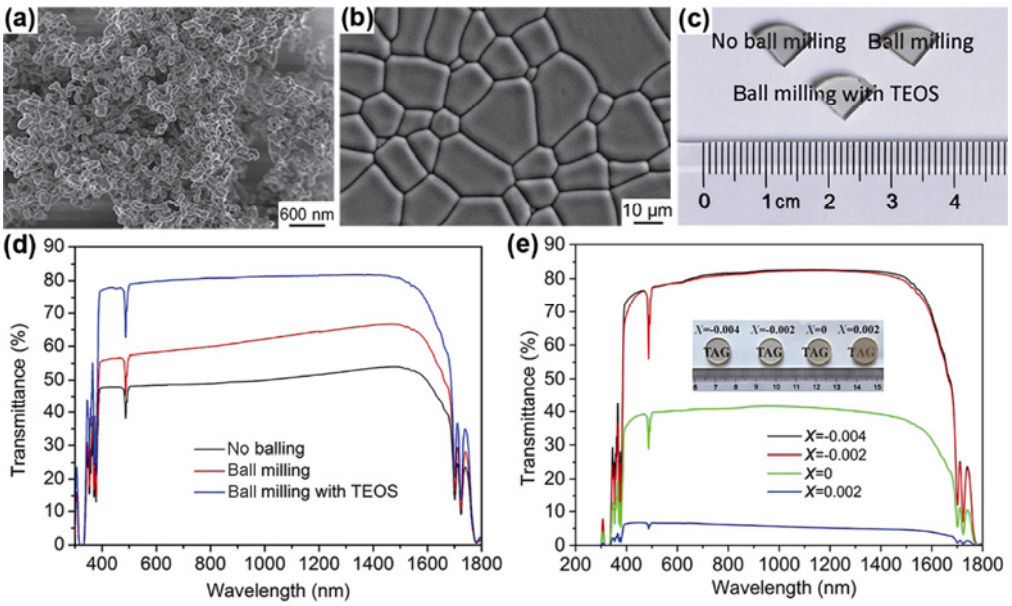


Fig. 6 FESEM micrographs of (a) as-synthesized TAG powders and (b) obtained TAG ceramics; (c) photographs and (d) in-line transmittance of TAG ceramics (1.5 mm thick); and (e) photographs and in-line transmittance of TAG ceramics after optimization (1.7 mm thick). Reproduced with permission from Ref. [166] for (a–d), © Elsevier B.V. 2018; Ref. [167] for (e), © The American Ceramic Society 2022.

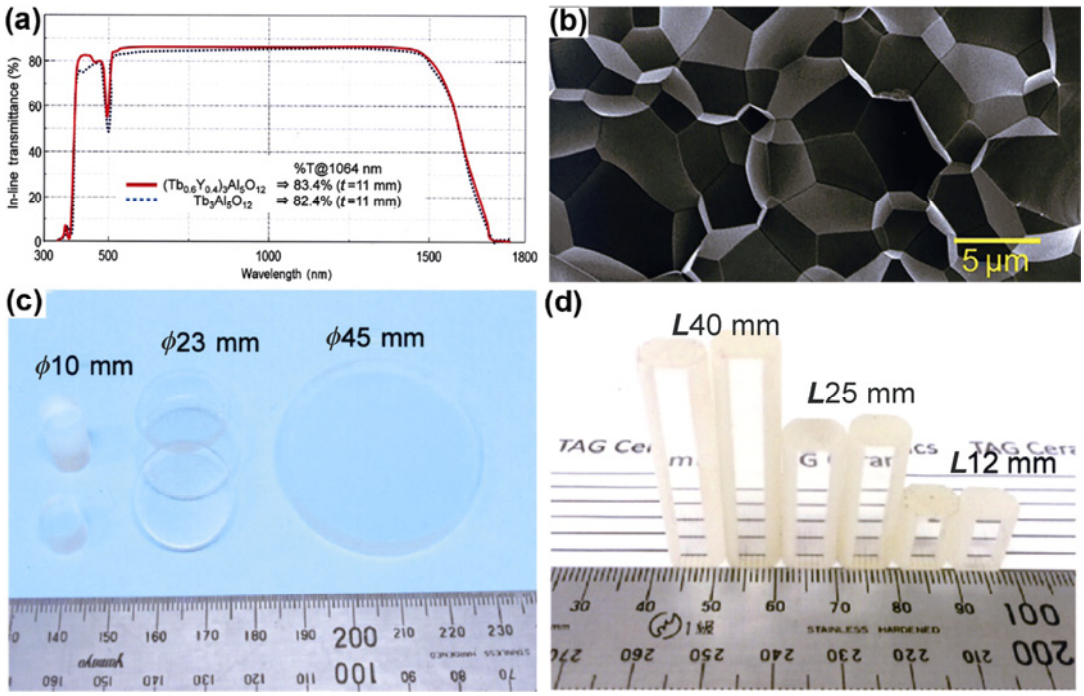


Fig. 7 (a) Transmission spectra of $(Tb_{0.6}Y_{0.4})_3Al_5O_{12}$ and TAG ceramics (t = 11 mm); (b) SEM image (fracture surface) of TAG ceramics; and appearance of (c) disk-shaped and (d) rod-shaped TAG ceramics. Reproduced with permission from Ref. [169], © The American Ceramic Society 2017.

reported TAG single crystals. The insertion loss and extinction ratio were measured to be comparable to those of commercial TGG single crystals. Figure 7(b) shows the fracture surface image of the TAG ceramics, in which the grain boundary fracture was in dominant, and the grain size was approximately 10–20 μm. The external views of TAG ceramics with long lengths and large apertures are shown in Figs. 7(c) and 7(d). These samples also showed high optical quality, and their size satisfied the requirements for Faraday isolators. Advantages such as downsizing, low cost, and better performance can be expected when TAG ceramics are used in practical devices.

In 2021, Hamamoto *et al*. [170] analyzed the thermally induced depolarization performance of TAG ceramics fabricated by Konoshima Chemical Co. Ltd. The optical transmittance of the TAG ceramic sample (3.1 mm thick) is almost identical to the theoretical transmittance. The temperature dependence of thermal conductivity of TAG ceramics was measured. The value became larger at lower temperatures and reached a peak of 50.3 $W \cdot m^{-1} \cdot K^{-1}$ at 20 K, which was significantly larger than the thermal conductivity of TGG ceramics, whose maximum value was 6.95 $W \cdot m^{-1} \cdot K^{-1}$ at 60 K. The absorption coefficient at room temperature was measured to be 2.1×10^{-3} cm^{-1} at 1070 nm. The depolarization of the isolators of "rod type" and "large thin disk type" was investigated under different magnetic flux densities and at different temperatures, as shown in Fig. 8. In a common condition (the isolator type was the rod type, and the magnetic flux density was 1 T at room temperature), the maximum acceptable power was about 100 W when the isolation ratio was 30 dB. Increasing the magnetic flux density and cooling can increase the value markedly, e.g., the power limit was over 3 kW at 77 K, as shown in Fig. 8(a). In another cooling scheme, the large thin disk type, the power limitation was enhanced by orders of magnitude, as shown in Fig. 8(b). At room temperature and under 1 T, the maximum acceptable power reached thousands of watts, and the value was over 10 kW when cooled to 150 K and under 2.5 T. These results suggested that the TAG ceramic material is one of the ideal materials for the Faraday isolators applied in high-power laser systems. Hamamoto *et al*. [170] also pointed out that the maximum power might be confined by other effects in practical work, such as nonuniformity of the material parameters or the magnetic field, beam shape distortion, mechanical stress, and residual stress. The accurate determination of all temperature-dependent properties of TAG ceramics is still needed.

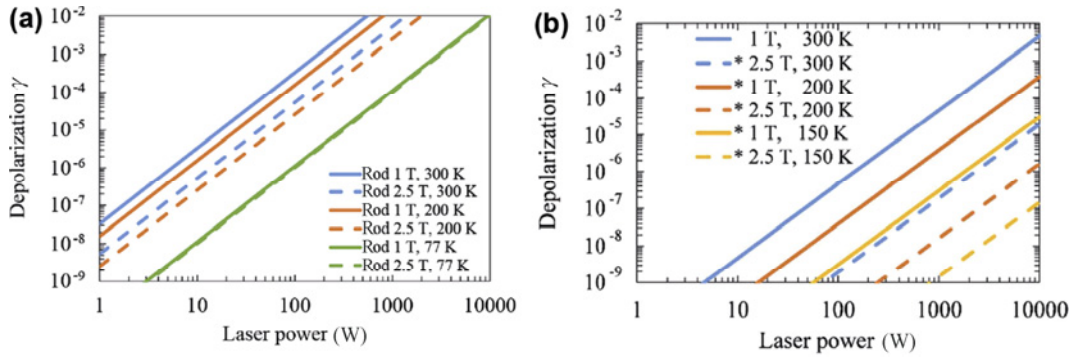


Fig. 8 γ in (a) rod type and (b) large thin disk type isolators. Reproduced with permission from Ref. [170], © Optical Society of America under the terms of the OSA Open Access Publishing Agreement 2021.

2.2.2 Doped and substituted TAG ceramics

There have been plenty of works studying TAG ceramics with ion doping and substitution. These ions were regarded as sintering aids (Si^{4+}, Mg^{2+}, Ti^{4+}, Zr^{4+}, Ce^{3+}, etc.), Verdet constant promoters (Ti^{4+}, Ce^{3+}, Pr^{3+}, Nd^{3+}, Ho^{3+}, Tm^{3+}, etc.), and component optimizers (yttrium ion (Y^{3+}), scandium ion (Sc^{3+}), Ga^{3+}, etc.).

TEOS or its decomposition products, SiO_2, has been used as the sintering aid in TAG ceramics since 2011 [150], and MgO was also added together with SiO_2 in Refs. [151,153,161,171]. As TAG has a similar crystal structure with that of YAG, the mechanism of SiO_2 and MgO promoting sintering in TAG is presumed to be similar to that in YAG ceramics [172,173]. To further improve the optical quality of TAG ceramics, many new sintering aids have been studied and discussed.

In 2016, Starobor *et al*. [174] investigated the Verdet constant and thermo-optical properties of Si-doped and Ti-doped TAG ceramics, which were provided by SIOM. These TAG ceramic samples were fabricated by the solid-state reaction method with MgO and TEOS as the sintering aid, and TEOS or TiO_2 with a series of concentrations was further added. The sample diameter was 15 mm, and the thickness was 3.1–3.6 mm. Ti-doping improved the transmittance in 700–1500 nm, but the transmission region was narrowed due to the absorption of Ti^{4+}. The Verdet constants of these doped TAG ceramics were almost the same, and were 12% higher than those of the undoped TAG ceramics at 1064 nm, which agreed with the results by Furuse *et al*. [157]. The results of the thermally induced depolarization properties showed that TAG ceramic sample with Si concentrations of 0.2% had better performance. It was estimated that an extinction ratio of 30 dB could be provided with a power up to 600 W. The FoM of Si:TAG (0.2%) is 55% greater than that of TGG ceramics. Ti-doping may cause an increase of optical absorption, and thus worsens the thermally induced depolarization property. In addition, samples with a higher doping concentration had a higher value of thermally induced depolarization, regardless of the type of doping ions, which indicated that the addition amount of sintering aid should be limited strictly. Starobor and Palashov [175] further investigated the thermal lens and thermally induced depolarization performance of Si-doped and Ti-doped TAG ceramics in the temperature range from 79 to 295 K. For TAG ceramics with 0.4 at% Si, the γ decreased more than 10 times, and the optical power of the thermal lens was more than 2 times when cooled from 295 to 79 K. This result showed that TAG ceramics can provide an isolation ratio of 30 dB at more than 6 kW.

Chen *et al*. [155,156] reported TAG ceramics with ZrO_2 as the additional sintering aid based on the sintering aid of 0.1 wt% MgO and 0.4 wt% TEOS. The results showed that ZrO_2 promoted the densification of TAG ceramics. When the sintering temperature is over 1550 ℃, a part of Zr^{4+} transforms to Zr^{3+} and substitutes Tb^{3+} sites, and excessive ZrO_2 is discharged from the ceramic matrix. These changes accelerate the grain growth and are beneficial to the improvement of optical quality. The transmittance of the Zr:TAG ceramics reached 82% at 1064 nm, which was close to the theoretical value. The grain size grew as large as 61.33 μm, much larger than that of pure TAG ceramics (35.91 μm). The laser-induced damage threshold of TAG was 5.7 $J{\cdot}cm^{-2}$ at 12 ns, and ZrO_2-doping enhanced the damage threshold to 7.26 $J{\cdot}cm^{-2}$ at 12 ns. The addition of ZrO_2 has little effect on the Verdet constant value of TAG ceramics. The thermally induced

depolarization performance of Zr:TAG ceramics was also measured [34], as shown in Fig. 9. The addition of ZrO_2 affected the thermally induced depolarization property, which can be attributed to the absorption of Zr^{3+} and the lattice distortion.

Chen *et al*. [146,154] fabricated Ce:TAG ceramics by solid state reaction and vacuum sintering. The result showed that CeO_2 was a useful sintering aid that helped remove pores and restrain grain growth. Significantly, for $(Tb_{0.997}Ce_{0.003})_3Al_5O_{12}$ ceramics, the Verdet constant was measured to be −199.55 rad·T^{-1}·m^{-1} at 632.8 nm, which was 16% higher than that of the undoped TAG. The enhancement was attributed to the crystal field changing and the quantum based superexchange interaction between Tb^{3+} and Ce^{3+}. Starobor *et al*. [104] studied the thermo-optical characteristics of TAG and Ce:TAG ceramics produced by SIOM and TGG ceramics produced by Konoshima Chemical Co. Ltd. Though Ce:TAG ceramics were reported to possess the highest Verdet constant among these ceramics, the depolarization in the undoped TAG ceramics was about twice less than that in Ce:TAG ceramics and less than that in TGG ceramics by a factor of 3.5. For thermal lens property, the arising thermal lenses were approximately the same for TAG and TGG ceramics, and about two times stronger for Ce:TAG ceramics.

In 2019, Yakovlev *et al*. [176] discussed the magneto-optical and thermo-optical properties of Ce-, Pr-, and Ho-doped TAG ceramics fabricated by SICCAS [177–179]. The photographs of the investigated ceramic samples are shown in Fig. 10(a). The Verdet constants of undoped and doped TAG ceramics with different ions and concentrations were measured to be almost

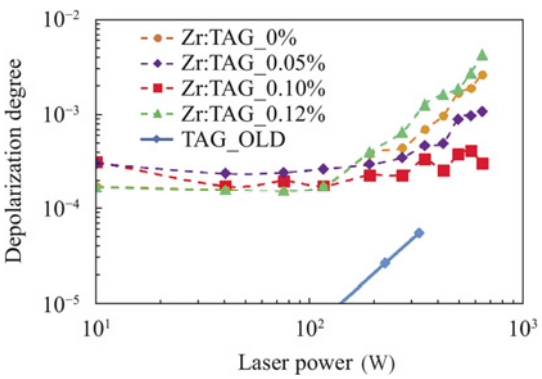


Fig. 9 Thermally induced depolarization results of Zr:TAG ceramics. Reproduced with permission from Ref. [34], © Infrared and Laser Engineering 2020.

the same, as shown in Figs. 10(b) and 10(c). This result contradicted the previous studies about the dependence of the Verdet constant on doping. They estimated the measurement error in their experiments, and the experimental accuracy of the Verdet constant for the studied samples was (on average) 4.5%. They proposed that a comparative measurement under the same experimental condition is needed in Verdet constant studies (e.g., using TGG crystal sample for comparation), which allow to minimize errors due to experimental conditions. Thermally induced depolarization measurement indicated that undoped TAG ceramics possessed the best thermo-optical performance, and their FoM was the largest, as seen in Figs. 10(d) and 10(e), respectively. Doping increased the thermally induced depolarization and decreased the FoM obviously for TAG ceramics in this study.

As Y^{3+}, Sc^{3+}, and Ga^{3+} can substitute Tb^{3+} or Al^{3+} sites in TAG and are beneficial to stabilizing the crystal lattice, avoiding the incongruent melting of TAG, the substitutions are common in TAG-based single crystals [54,67,180]. $(Tb_{1-x}Y_x)_3Al_5O_{12}$ [146,169, 181], TSAG [182], $(Tb_{1-x-y}Y_xSc_y)_3(Al_{1-z}Sc_z)_5O_{12}$ [183,184], $(Tb_{1-x-y}Lu_xSc_y)_3(Al_{1-z}Sc_z)_5O_{12}$ [185], and $Tb_3(Al_{1-x}Ga_x)_5O_{12}$ [180,186] ceramics have been studied, and the results showed that these substitution ions can also help improve the optical quality of TAG ceramics. However, the thermal conductivity and the Verdet constant decrease inevitably due to the high addition amount (> 10 at% in TAG).

Up to now, a scientific explanation is still needed for the dependence of the Verdet constant on doping. In current studies, doping ions with distinctive absorption bands in visible to near infrared (IR) have no benefit for paramagnetic ceramics as they reduce the thermal conductivity, increase the α_0, deteriorate the thermal-induced depolarization, and reduce the FoM. In order to improve the comprehensive performance of TAG ceramics, the choice of sintering aids and the addition amount needs to be carefully considered. Sintering aids without absorption bands in visible to near IR may be better choices, such as Si^{4+} and Mg^{2+}. Though studies have confirmed that TAG ceramics are excellent alternative materials for TGG crystals, there has been no TAG ceramic product commercially available up to now. Much effort is still in demand to achieve a mass production of TAG ceramics with high quality.

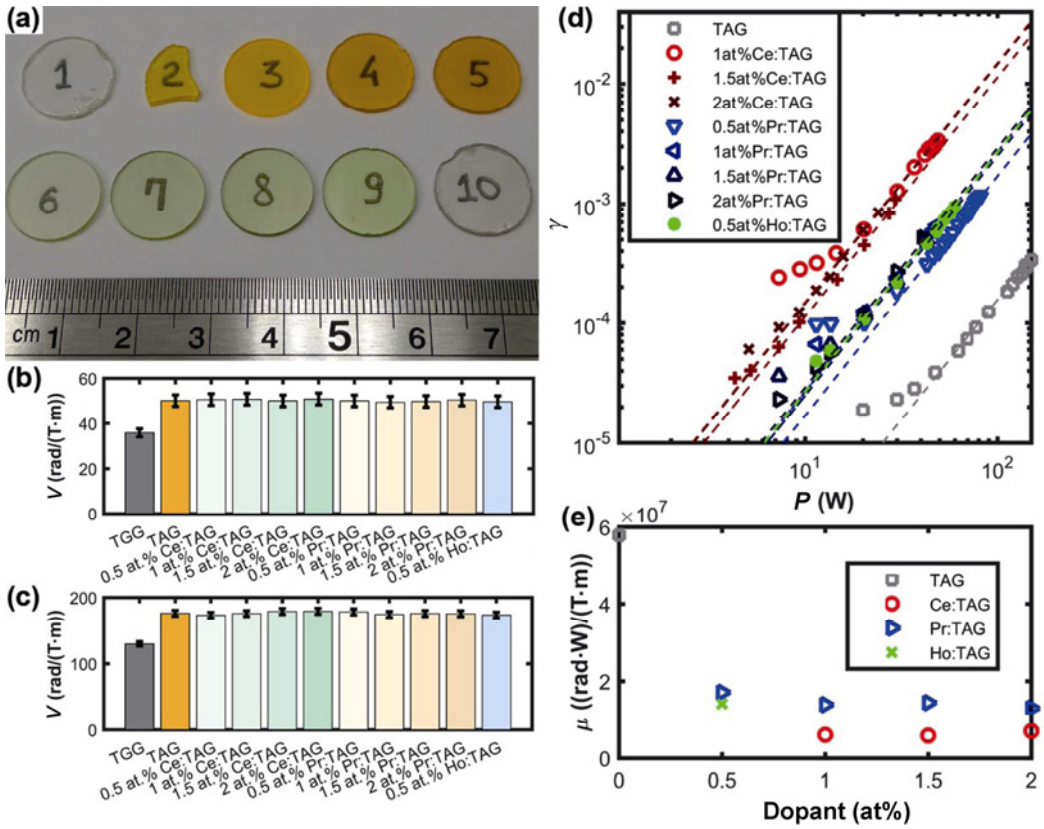


Fig. 10 (a) Photographs of investigated ceramic samples (1—TAG, 2–5—0.5, 1, 1.5, and 2 at% Pr:TAG, 6–9—0.5, 1, 1.5, and 2 at% Pr:TAG, and 10—0.5 at% Ho:TAG); measured V values for studied TGG single crystal, TAG, and RE:TAG ceramic samples at (b) 1064 nm and (c) 633 nm; (d) thermally-induced γ in studied ceramic samples; and (e) magneto-optical μ vs. concentration and type of dopant. Reproduced with permission from Ref. [176], © IEEE 2019.

2. 3 Other paramagnetic garnet ceramics

Tb^{3+} possesses large n_{eff}^2/g and wide transparent wavelength band in visible to near-IR range, so Tb-based MO materials have been extensively studied and used. Dy^{3+} and Ho^{3+} are also magnetically active RE ions with large n_{eff}^2/g. Due to the different absorption bands, they have different transparent wavelength bands and thus different application bands.

$Dy_3Al_5O_{12}$ (DyAG) single crystals have been studied for a long time as one of the most promising magnetic refrigerants for the Carnot-type magnetic refrigerator [187], and DyAG is also a potential material for Faraday isolators. Hu *et al*. [188] fabricated DyAG ceramics by the solid-state reaction method with TEOS and MgO as the sintering aids. After vacuum sintering at 1820 ℃ for 6 h, the transmittance of DyAG ceramics reached 80% in the visible-light region, as shown in Fig. 11. The Verdet constant of DyAG was measured to be −119 rad·T^{-1}·m^{-1} at 632.8 nm, which was slightly lower than that of TGG crystals (−131 rad·T^{-1}·m^{-1}).

Wang and Lu [189] reported $Ho_3Al_5O_{12}$ (HoAG) ceramics fabricated by vacuum sintering from co-precipitated powders. The appearance and in-line transmittance of HoAG ceramics are shown in Fig. 12. After optimization, the transmittance of HoAG ceramics reached 80.3% at 589 nm and around 80% in partial middle-infrared (mid-IR) spectral region. The optical quality can be further improved by optimizing the fabrication process. The Verdet constants of HoAG ceramics were measured to be −154, −36, and −16 rad·T^{-1}·m^{-1} at 635, 1064, and 1550 nm, respectively. These values are higher than those of commercial TGG crystals. The thermal conductivity was measured to be 10.5 W·m^{-1}·K^{-1} at room temperature, which was twice higher than those of TGG and TAG ceramics. These results indicate that HoAG ceramics could be used in MO devices operating in a ~1 μm laser system. The presence of absorption lines close to ~1 μm can significantly limit the use of this material due to thermally induced effects, which requires further study.

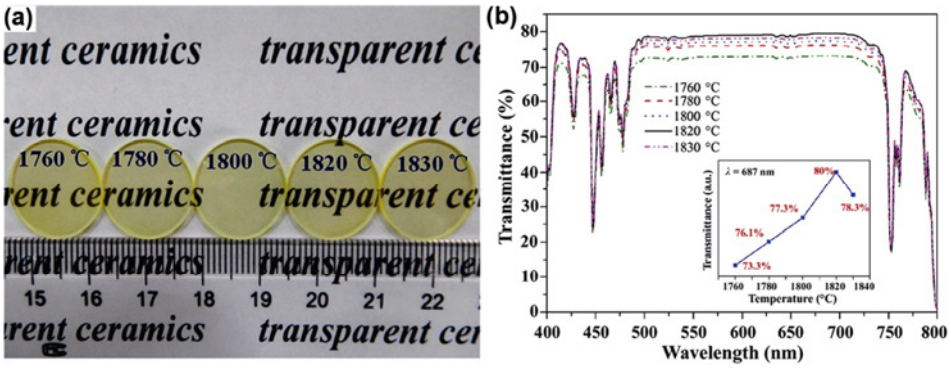


Fig. 11 (a) Photographs and (b) in-line transmittance of DyAG ceramic samples prepared at different temperatures (1 mm thick); the inset in (b) shows the change in the transmittance as the sintering temperature increases. Reproduced with permission from Ref. [188], © The American Ceramic Society 2015.

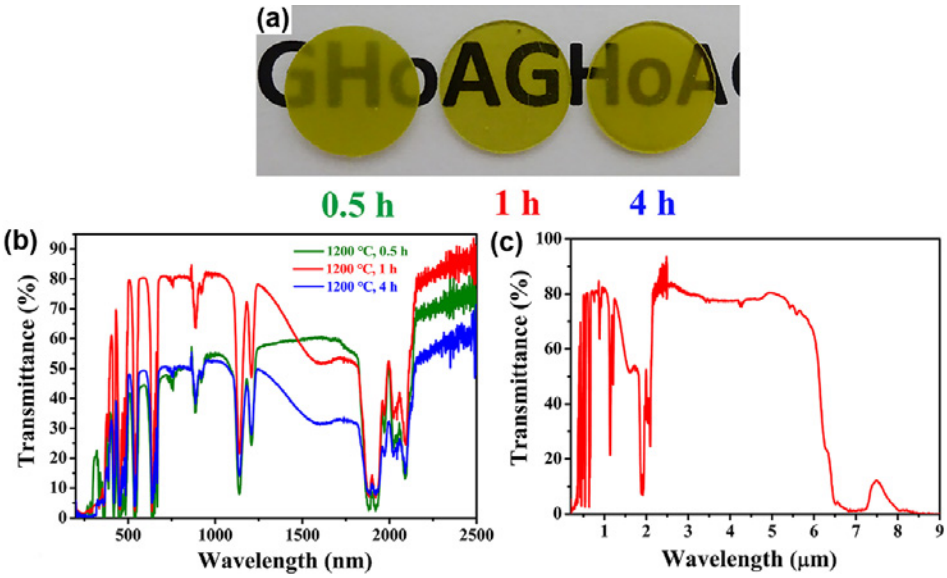


Fig. 12 (a) Appearance and (b, c) in-line transmittance of HoAG ceramics. Reproduced with permission from Ref. [189], © Acta Materialia Inc. 2021.

2. 4 $Y_3Fe_5O_{12}$ (YIG)-based magneto-optical ceramics

YIG is a ferromagnetic material with excellent magnetic properties and has been widely applied in magnetic recording, MO switch, optical fiber communication, and medical field [190–194]. Due to the absorption of Fe^{3+}, YIG cannot be used in the ultraviolet (UV) to near-IR region, but YIG still has a wide transmission range from 1.1 to 7 μm. As YIG is an incongruent melting material [195], it is hard to obtain YIG single crystals in large sizes by the Czochralski method. Up to now, the flux method [196], floating zone method [68], and edge-defined film-fed growth (EFG) method [197] have been used to synthesize YIG single crystals, and liquid phase epitaxy (LPE) method [198,199] has been widely used to produce YIG films. However, there are still some problems in the manufacture of YIG crystals and films, and the size and the optical quality of YIG materials fabricated by these methods cannot meet the updated requirement for Faraday isolators. Ceramic synthesis technology is a non-melting process, by which the incongruent melting problem is avoidable, so it is possible to fabricate transparent YIG ceramics with large sizes and high optical quality.

Yang *et al*. [200] fabricated YIG ceramics by air pressureless sintering using YIG nano-powders synthesized via the co-precipitation method. The influences of the calcination temperature on the phase compositions and morphologies of the nano-powders were investigated in detail. A loss of oxygen (O_2) during high-temperature sintering was found, which led to the transformation of Fe^{3+} to Fe^{2+}, and an iron-oxide secondary phase was

detected. The in-line transmittance of the obtained YIG ceramics was lower than 20% from 1000 to 3000 nm (0.3 mm thick), which was insufficient to meet the requirements for the application in the Faraday isolators.

In 2018, Ikesue and Aung [201] fabricated fully dense and transparent YIG ceramics by the solid-state reaction method combined with HIP post-treatment. The appearance and SEM image of the HIPed YIG ceramics are shown in Figs. 13(a) and 13(b), respectively. After pre-sintered in an O_2 atmosphere and HIP treated in a mixed gas (20% O_2–80% Ar, 147 MPa), YIG ceramics showed a high transmittance, as shown in Fig. 13(c), which was almost the same as the transmittance of YIG single crystal from 1700 to 2500 nm. In addition, YIG single crystals and ceramics showed similar MO properties, but the insertion loss of YIG ceramics was fairly larger (0.3 dB vs. 0.1 dB). If the optical quality of YIG ceramics is further improved, they will have many advantages such as extinction ratio, large scale, and mass productivity. The development of YIG ceramics will become a trigger for future technological innovation in the field of optical communication. In 2022, Ikesue and Aung [202] made an attempt on the pressureless sintering in order to fit industrial applications. They used γ-Fe_2O_3 and α-Fe_2O_3 as the starting materials to synthesize YIG ceramics by pressureless reactive sintering at an O_2 atmosphere (1 atm). The transmission spectrum of the YIG ceramics from γ-Fe_2O_3 starting material with small particle size was 71% at ~2 μm, while that of the ceramics from α-Fe_2O_3 starting material was only a few percent (1 mm thick). The result shows that the particle size and sinterability of starting materials are

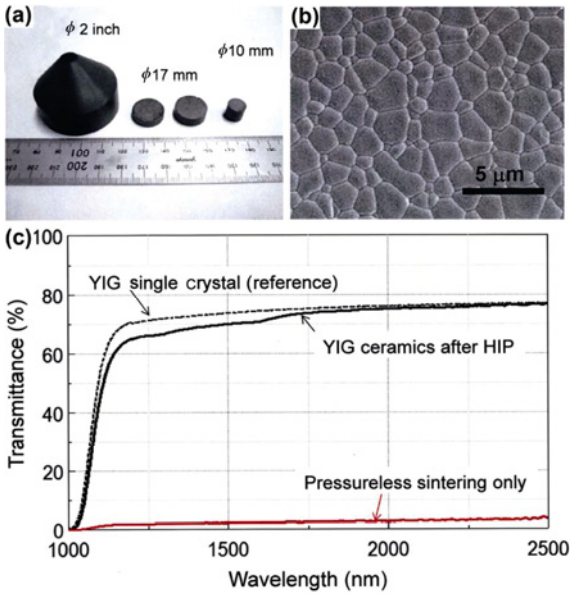


Fig. 13 (a) Appearance and (b) SEM image of YIG ceramics after HIP; (c) in-line transmittance of YIG ceramics after pressureless sintering (1 mm thick) and O_2-HIP treatment (2 mm thick) (the thickness of reference YIG crystal is 1 mm). Reproduced with permission from Ref. [201], © The American Ceramic Society 2018.

important factors for the reactive sintering method, and it is challenging to obtain high-quality YIG ceramics by a pressureless sintering method.

Bismuth (Bi) doping has been proved to be an effective way to enlarge the Faraday rotation angle of YIG film [203,204]. In 2019, Aung *et al.* [205] succeeded in fabricating $(Bi_xY_{3-x})Fe_5O_{12}$ (x = 0–1.1) ceramics by the solid-state reaction method. $(Bi_{0.4}Y_{2.6})Fe_5O_{12}$ ceramics and $(Bi_{1.1}Gd_{1.9})Fe_5O_{12}$ single crystals (fabricated by the LPE method) had almost the same optical transmittance, as shown in Fig. 14(a). The Faraday rotation direction

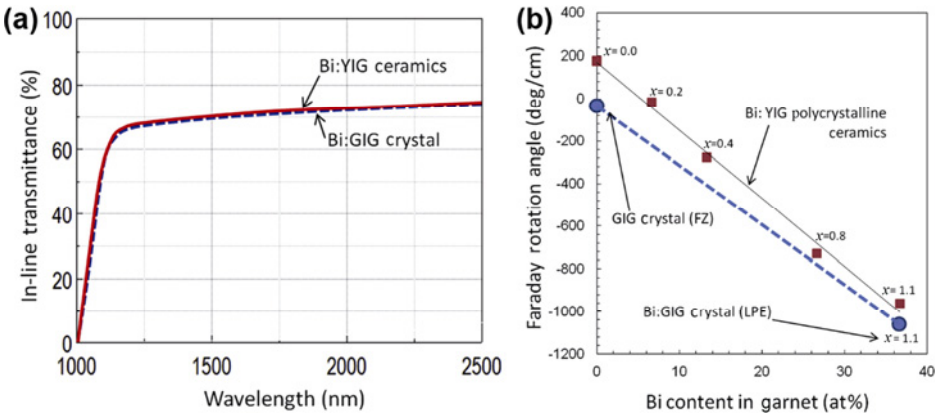


Fig. 14 (a) Transmittance spectra of Bi-doped GIG single crystal by LPE method and Bi-doped YIG ceramics by reactive sintering (the thickness of all samples is 0.35 mm); (b) Faraday rotation angle of produced $(Bi_xY_{3-x})Fe_5O_{12}$ ceramics and Bi-doped GIG single crystal vs. Bi content at 1550 nm. Reproduced with permission from Ref. [205], © Elsevier B.V. 2019.

is negative for Bi-substituted samples, and the rotation angle increased linearly with the increase of substituted Bi, from +174 (°)·cm^{-1} for x = 0 to −970 (°)·cm^{-1} for x = 1.1 at 1550 nm, as shown in Fig. 14(b). The rotation angle per unit amount of Bi in Bi-doped YIG ceramics was calculated to be −31.2 (°)·cm^{-1} in terms of 1 at% of Bi, which was almost the same as that in Bi-doped GIG (−30.0 (°)·cm^{-1}).

Zou *et al*. [206] fabricated $(Bi_xY_{3-x})Fe_5O_{12}$ (x = 0–0.9) ceramics by the hot-pressing sintering process with the solid-state reaction method. The transmittance of undoped YIG ceramics was over 40% from 1000 to 6000 nm, but the transmittance decreased with the increasing Bi concentration. A Bi-rich secondary phase was detected in $Bi_{0.9}Y_{2.1}Fe_5O_{12}$ ceramics, so the solid solution limitation of Bi in YIG ceramics should be further investigated. The Faraday rotation angles at 1064 and 1550 nm of $Bi_xY_{3-x}Fe_5O_{12}$ ceramics were also measured. The amount of rotation angle change per 1 at% Bi is −49.0 (°)·cm^{-1} at 1064 nm and −30.2 (°)·cm^{-1} at 1550 nm. These results showed that Bi substitution in YIG ceramics helps improve the MO performance; however, the optical loss due to the solid solution limitation of Bi should be carefully considered.

Ce is another effective additive element in YIG to enlarge the Faraday rotation angle, but the difference of large ion radius, thermal stability of CeO_2 peroxide, and small segregation coefficient make the fabrication of Ce-doped YIG single crystal extremely difficult [207–209]. In 2020, Ikesue *et al*. [210] reported $(Ce_xY_{3-x})Fe_5O_{12}$ (x = 0–0.24) ceramics fabricated by the solid-state reaction method. The appearance and transmission spectrum are shown in Figs. 15(a) and 15(b), respectively. The transmittance of $(Ce_{0.12}Y_{2.88})Fe_5O_{12}$ ceramic sample with a thickness of 0.5 mm was 62%–67% from 1500 to 2000 nm. As a comparator, the transmittance of Ce:YIG single crystal fabricated by the flux method with a thickness of 0.2 mm was about 72% at 1550 nm. Considering the thickness difference, the transmission characteristic of $(Ce_{0.12}Y_{2.88})Fe_5O_{12}$ ceramics is superior to that of the single crystals synthesized by the flux or FZ methods, though the Mie and Rayleigh scattering still exist. The absorption coefficient of $(Ce_{0.12}Y_{2.88})Fe_5O_{12}$ ceramics was 0.3 cm^{-1} at 1550 nm, which was much smaller than those of the Bi-substituted YIG and 8 at% Ce:YIG single crystals, as shown in Fig. 15(d). The Faraday rotation angles of $(Ce_xY_{3-x})Fe_5O_{12}$ ceramics are shown in Fig. 15(c).

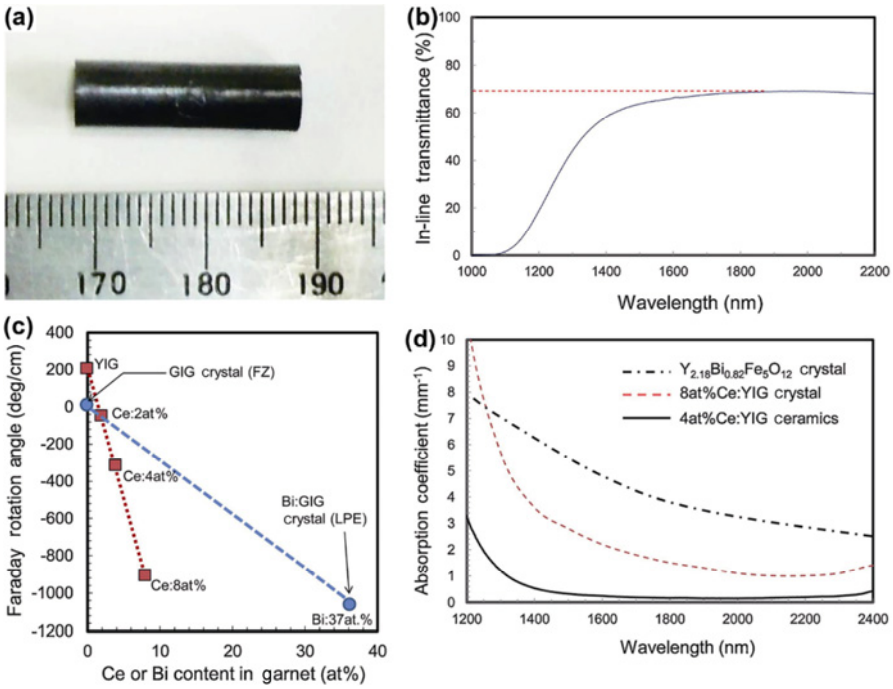


Fig. 15 (a) Appearance of Ce:YIG ceramics; (b) in-line transmission spectrum of $(Ce_{0.12}Y_{2.88})Fe_5O_{12}$ ceramics (0.5 mm thick) measuring between 1000 and 2500 nm; (c) Faraday rotation angle of produced $(Ce_xY_{3-x})Fe_5O_{12}$ ceramics and Bi-doped GIG single crystal vs. Ce or Bi content at 1550 nm; and (d) comparative data of absorption coefficient between Ce:YIG single crystal by the FZ method, Ce:YIG ceramics produced in this work, and Bi:YIG crystal as a reference ranging from 1200 to 2400 nm. Reproduced with permission from Ref. [210], © Elsevier Ltd. 2020.

Similar to that of the Bi substitution, the rotation direction turns reversed when Ce is doped, and the rotation angle reaches −990 (°)·cm^{-1} when x = 0.24 (8 at%). The amount of rotation angle change per 1 at% Ce is −144 (°)·cm^{-1}, which is much larger than that of Bi, so Ce:YIG ceramics with high Ce concentrations are promising materials with superior MO performance if the added Ce can be totally dissolved in the YIG lattice. In 2023, Tao *et al*. [211] fabricated Ce:YIG ceramics by the solid-state reaction using a hot-press sintering with an O_2/nitrogen atmosphere. The in-line transmittance of $Ce_xY_{3-x}Fe_5O_{12}$ ceramics with x = 0, 0.12, and 0.24 at 1550 nm were 72%, 66.5% and 57.6%, respectively (0.5 mm thick). Limited by the solubility of Ce^{3+} in YIG, when the Ce doping amount was higher than 8 at% (x = 0.24), a Ce-rich secondary phase was detected; and when x = 0.36, a large amount of secondary phase made the ceramics opaque.

Besides YIG, other RE-ion garnet materials may also possess good MO performance. Aung and Ikesue [212] succeeded in the fabrication of $Tb_3Fe_5O_{12}$ (TIG) ceramics by the reactive sintering method. Figure 16 shows the appearance of TIG ceramics and an in-line transmission curve of the sample with 0.9 mm in thickness. The transmittance of TIG ceramics was 51% at 1550 nm. The transmission loss of the TIG ceramic sample was estimated to be 21% mm^{-1}, and was mainly caused by residual pores. Further improvement of optical quality is needed by eliminating the residual pores. In addition, the characteristic absorption of Tb can be observed clearly in the wavelength region longer than 1.6 μm. Compared with those of YIG single crystals and ceramics, the application band of TIG ceramics is apparently constrained due to these absorptions. The Faraday rotation angle of TIG ceramics was measured to be 350 (°)·cm^{-1} at 1300 nm, which was the same as that of TIG single crystals and about 1.5 times larger than that of YIG single crystals. The solid solution limitation of doping ions and the grain boundary segregation may deteriorate the optical quality in Bi:YIG and Ce:YIG crystals and ceramics. As there are no doping ions in TIG ceramics, optical quality and homogeneity of the Faraday rotation angle are more likely to be guaranteed. After optimizing the optical quality, TIG ceramics may be a promising MO material used in 1200–1550 nm.

Current studies confirm that ceramic synthesis technology is an excellent approach to obtaining YIG-based materials with high optical quality and large sizes, as the incongruent melting problem in the growth of YIG crystals is avoided. In addition, the segregation of doping ions does not occur evidently in ceramics, so the Faraday rotation angle is homogeneous along the magnetic direction. To meet the requirement of the Faraday isolators, the optical quality of YIG-based ceramics needs to be further upgraded, such as improving the uniformity of raw powders, exploring effective sintering aids, and optimizing the sintering technology.

3 Sesquioxide ceramics

The RE elements of Dy, Tb, Ho, and Er are the most magnetically active elements, and the corresponding sesquioxides (terbium sesquioxide (Tb_2O_3), Dy_2O_3, Ho_2O_3, and Er_2O_3) have wideband gaps allowing for light transmission in the visible range and IR range. The magneto-optical sesquioxides contain only paramagnetic cations, e.g., there are only Tb^{3+} and O^{2-} in Tb_2O_3; but for TAG, there is additional Al^{3+}. As a result, N is lower in TAG, so the Verdet constant of

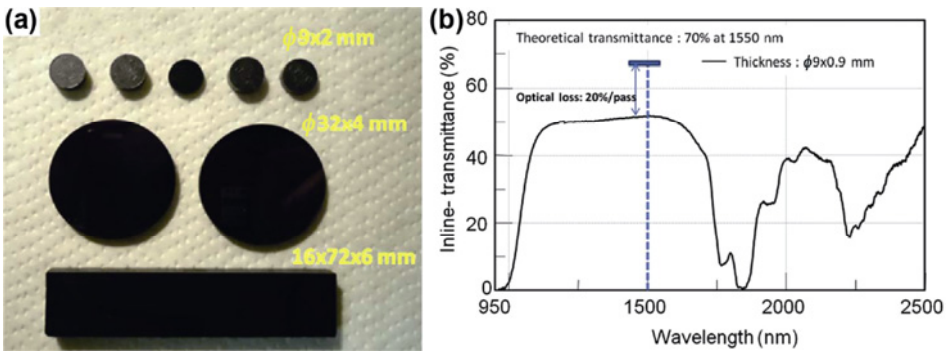


Fig. 16 (a) Appearance of TIG ceramics; (b) in-line transmittance of TIG ceramics with 0.9 mm in thickness. Reproduced with permission from Ref. [212], © Elsevier B.V. 2018.

Tb_2O_3 is much higher than that of TAG according to Eq. (3). Sesquioxides also have advantages such as high transparency and excellent thermal properties. Despite the advantages, the successful production of RE sesquioxide crystals with very high magnetic susceptibility and transparency has been rarely reported, which is limited by the high melting points and the phase transformations below the melting points and the shortcomings in processing technology. The development of transparent ceramic technology makes it possible to fabricate the magneto-optical sesquioxide ceramics with high quality.

3. 1 Tb_2O_3-based ceramics

Tb_2O_3, as one of the most promising candidate materials for Faraday isolator used in the visible and near-IR wavelength range, presents high transmittance and large Verdet constants, which are about 3.5 times larger than those of commercial TGG materials. Because of the high melting point of about 2300 ℃ and phase transitions from an orthorhombic to cubic crystal system near 1600 ℃ and an orthorhombic to hexagonal crystal system near 2100 ℃, it is difficult to grow a Tb_2O_3 single crystal. The latest report of cubic pure Tb_2O_3 crystals was published in 2015 [74], in which a flux method was used. However, the obtained Tb_2O_3 crystal was only ~5 mm × 5 mm × 1.2 mm in size, and the optical transmittance did not reach the theoretical value, so the specimen cannot meet the requirement of high-performance Faraday isolators. The research about Tb_2O_3 ceramic synthesis technology was firstly appeared in the patent in 2016 [213]. In recent years, the reports consisting of the fabrication, characterization of optical quality, MO quality, and thermo-optical properties of Tb_2O_3 ceramics were successively reported by the researchers from Russia, Japan, and China. In 2016, Snetkov *et al*. [214] firstly reported the Tb^{3+}:Y_2O_3 ceramics with Tb^{3+} ion concentrations of 10%, 20%, 30%, and 100% (pure Tb_2O_3) from the starting nano-powders produced by self-propagating high-temperature synthesis (SHS) using the acetate–nitrate salts of metals. The Tb^{3+}:Y_2O_3 ceramics prepared by hot pressing (HP) had several transmission bands consisting of 380–1750, near 5500, and 6500–8000 nm. The 100% Tb^{3+}:Y_2O_3 ceramic sample (pure Tb_2O_3) showed an in-line transmittance of 63.4% at 1064 nm. The Verdet constant had a linear dependence on the Tb^{3+} ion concentration in the Tb^{3+}:Y_2O_3 ceramics. The Verdet constant of 30% Tb^{3+}:Y_2O_3 was equal to that of TGG single crystal containing 37.5 at% of Tb^{3+} ions. The pure Tb_2O_3 ceramics had the highest value of the Verdet constant, which is more than three times higher than that of the TGG crystals or ceramics. Reference [214] proposes a new thought for promising Faraday devices. However, the optical quality of the fabricated ceramics still needed to be improved for the practical application. In Ref. [215], the cryogenic temperature characteristics of Verdet constant for Tb_2O_3 ceramics were discussed. The Verdet constant of Tb_2O_3 ceramics cooled down to the liquid nitrogen temperature increased by more than a factor of 3.2 times when comparing to the values at room temperature.

Balabanov *et al*. [216,217] focused on the preparation of Tb_2O_3 ceramics with high optical quality by the synthesis of ultrafine terbium oxide powders, and finally fabricated RE:Tb_2O_3 ceramics [218]. Tb_2O_3 nano-powders were produced by the SHS method, and the obtained powders were composed of multiphase of trigonal Tb_7O_{12} and triclinic $Tb_{11}O_{20}$, and converted to cubic Tb_4O_7 at about 200 ℃ during heating, and then transformed into the cubic Tb_2O_3 phase after calcination at 600–800 ℃ in a reducing atmosphere, finally to the monoclinic Tb_2O_3 at about 1525 ℃. The nano-powders of Tb_2O_3 solid solution with Sc_2O_3, Y_2O_3, and Lu_2O_3 were produced by the same SHS. Lu_2O_3 was found to have negligible impact on the phase formation in Tb_2O_3; on the contrary, Y^{3+} and Sc^{3+} significantly suppressed crystallization and formation of Tb_2O_3 cubic phase. The introduction of small amounts of Y_2O_3 or Lu_2O_3 benefited to the intensification of the terbium ceramics' densification. RE:Tb_2O_3 magneto-optical ceramics (RE = Y^{3+}, Lu^{3+}, Sc^{3+}, Ce^{3+}, Dy^{3+}, Ho^{3+}, Yb^{3+}, and Nd^{3+}) were successfully reported and charactered in 2020 [218], as shown in Fig. 17(c). The value of the in-line transmittance of the pure Tb_2O_3 was 80% at 1064 nm, and the transmittance slightly decreased when doped with RE ions expect Sc^{3+}, which significantly reduced the transmittance, as shown in Figs. 17(a) and 17(b). The Verdet constants at some certain wavelengths for pure Tb_2O_3 and RE:Tb_2O_3 ceramics were measured, as presented in Fig. 17(d). The Verdet constant of the pure Tb_2O_3 ceramics at 633 nm was −447.5 rad·T^{-1}·m^{-1}, 3.3 and 2.6 times higher than those of TGG single crystals and TAG ceramics, respectively. The introduction of RE ions in relatively high concentrations resulted in the decrease of the value of the Verdet constant. Doping

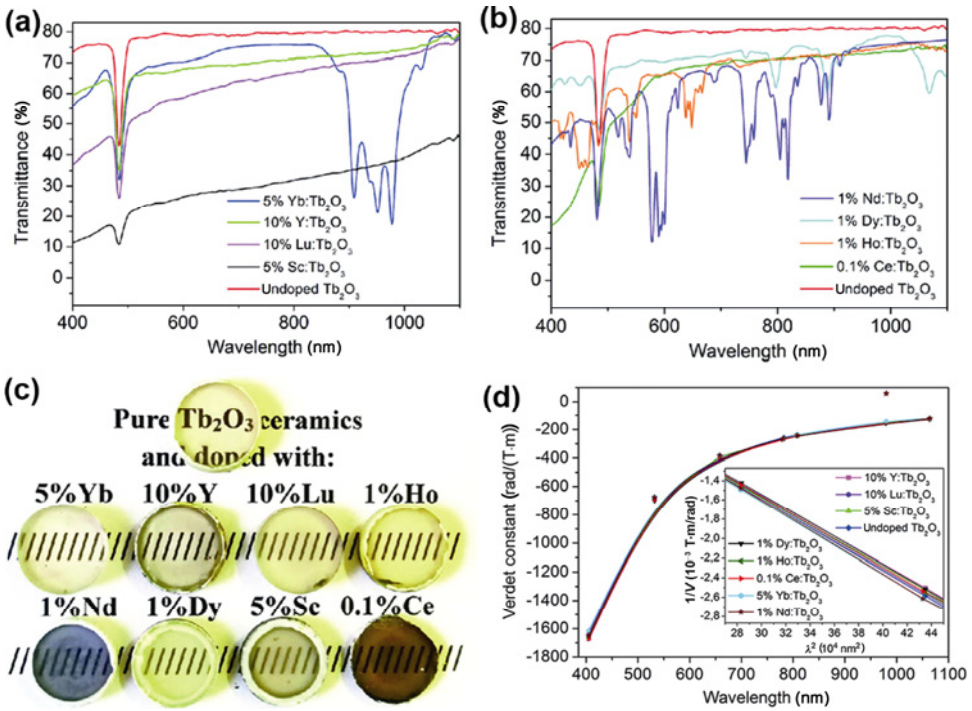


Fig. 17 In-line transmittance curves of Tb_2O_3 and RE:Tb_2O_3 transparent ceramics: (a) undoped Tb_2O_3 (2.6 mm thick), 10 at% Y^{3+}:Tb_2O_3 (1.9 mm thick), 10 at% Lu^{3+}:Tb_2O_3 (2.3 mm thick), 5 at% Sc^{3+}:Tb_2O_3 (2.3 mm thick), and 5 at% Yb^{3+}:Tb_2O_3 (2.0 mm thick); (b) undoped Tb_2O_3 (2.6 mm thick), 1 at% Dy^{3+}:Tb_2O_3 (2.0 mm thick), 0.1 at% Ce^{3+}:Tb_2O_3 (1.9 mm thick), 1 at% Ho^{3+}:Tb_2O_3 (2.0 mm thick), and 1 at% Nd^{3+}:Tb_2O_3 (2.0 mm thick). (c) Their appearance and (d) wavelength dependence of Verdet constants of Tb_2O_3 and RE:Tb_2O_3 ceramics; the inset shows the inverse of the Verdet constant ($1/V$) as a function of the wavelength square for the range of 520–670 nm. Reproduced with permission from Ref. [218], © WILEY-VCH Verlag GmbH & Co. KGaA, Weinheim 2019.

with RE ions has its good aspect of improving the sinterability and increasing the temperature of polymorphic transition of Tb_2O_3 ceramics, but also leads to the reduction of the thermal conductivity coefficient and the increase of α_0.

The thermal effects caused by the release of heat in the optical element in the laser system are important factors limiting the average power of lasers. The thermo-optical properties of Tb_2O_3 ceramics were reported by Snetkov *et al*. [106] in 2021. The thermal conductivity of Tb_2O_3 ceramics was close to that of TGG, and the thermo-optical constants of Tb_2O_3 ceramics were three times smaller than those of the TGG materials. The value of allowed power for the samples was estimated to be only P_{max} = 18–30 W (depending on the sample) due to high absorption. The P_{max} will be increased by 6.3–6.8 times compared with that of TGG, only when the absorption α_0 (= 0.0013–0.0021 cm^{-1}) is realized. Therefore, the fabrication technology of Tb_2O_3 ceramics still needs to be improved. In 2021, Snetkov *et al*. [219] developed and manufactured a traditional Faraday isolator based on Tb_2O_3 ceramics, and the experimental studies of the operation at high-power laser radiation were performed for the first time, as shown in Fig. 18. The produced Faraday isolator provided an isolation ratio better than 30 dB at the average power of laser radiation of 90 W. When arising at the average power of 90 W and spot diameter of 1.3 mm, the F of the thermal lens was 1.16 m. According to Ref. [219], we know that with the use of the existing Tb_2O_3 ceramic material with low absorption, it is possible to create traditional Faraday isolators ensuring a high isolation ratio (> 30 dB) for the continuous wave (CW) laser power of more than 200 W. However, the main drawback for Tb_2O_3 ceramics is the high value of the absorption coefficient. Considering this aspect, the Tb_2O_3 material at the moment is inferior to the TGG material when used in high-power laser systems.

The main factor limitation for the application of Tb_2O_3 ceramics in Faraday devices is the thermal effect due to the high absorption coefficient. Cryogenic cooling can increase the Verdet constant, as well as minimize the thermally induced effect. Therefore, it is

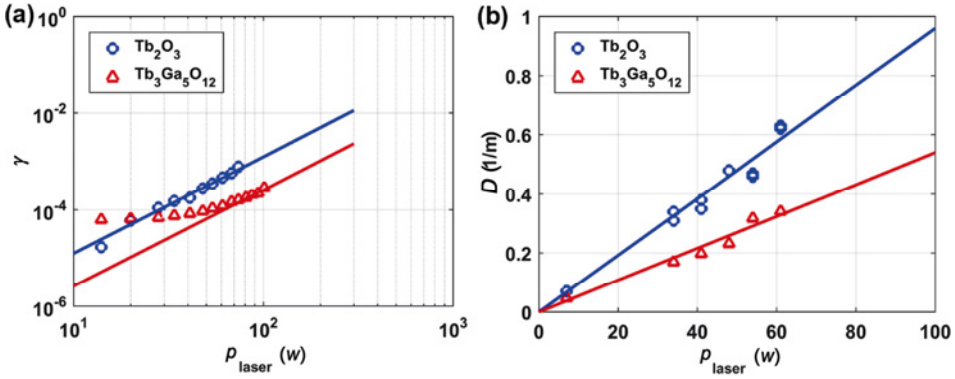


Fig. 18 (a) γ and (b) D as a function of P_{las} for Faraday isolator on Tb_2O_3 ceramics (the circles) and TGG crystal (the triangles). Reproduced with permission from Ref. [219], © Elsevier B.V. 2021.

an important work for the development of cryogenic Faraday isolators and investigating the temperature dependence of the thermo-optical constants that determines the thermal effects of Tb_2O_3-based ceramics. More details about the thermally-induced depolarization and the thermal lens at the temperature range of 81–297 K in $(Tb_{0.9}Y_{0.1})_2O_3$ ceramics were presented by Yakovlev *et al*. [220] in 2022. The α_0 and the temperature dependence of the $\alpha_0 P_{eff}/\kappa$ and $\alpha_0 Q_{eff}/\kappa$ at the 83–297 K temperature range of $(Tb_{0.9}Y_{0.1})_2O_3$ ceramics were studied. The α_0 was measured to be 0.63±0.03 cm^{-1}, and the ratio of P_{eff}/Q_{eff} was 6.44±0.61 in the studied temperature range, both independent to the temperature at 83–297 K. The thermally induced depolarization and the thermal lens on cooling to LN_2 decreased by 28 and 5.2 times, respectively, compared with those at room temperature. It is necessary for Tb_2O_3 ceramics to further increase the optical quality and decrease the absorption for the promising application in a large-aperture Faraday isolator used in a high-average and high-peak-power laser system.

Makikawa *et al*. [213] from World-Lab. Co., Ltd. began to find a novel material and filed a patent on the $(Tb_xY_{1-x})_2O_3$ (TYO; x = 0.5–1.0) ceramics in 2016. The optical-grade TYO ceramics were successfully produced for the first time in Ref. [221] published in 2017, and the total performance was latterly reported in Ref. [222] published in 2019. The TYO ceramics were prepared by vacuum sintering and the subjected HIP treatment. The values of in-line transmittance at 1 μm of $(Tb_{0.6}Y_{0.4})_2O_3$ and Tb_2O_3 ceramics with the thickness of 5 mm reached 81.1% and 80.4%, respectively, as shown in Fig. 19. The Verdet constants were confirmed to simply increased with the increase of Tb concentration in the TYO ceramics, and the maximum value of 154 $rad \cdot T^{-1} \cdot m^{-1}$ at 1064 nm was obtained for Tb_2O_3 ceramics. According to Ref. [213], the application advantage is emphasized that as the Verdet increases, the length of Faraday rotator elements required to give a Faraday rotation angle of 45° is minimized to 5.2 mm, making it possible to downsize the optical isolator. The total performance of TYO ceramics with optical-grade quality and extremely low scattering was described minutely in Ref. [222] published in 2019, and the in-line transmittance curves are shown in Fig. 19. The Verdet constant of Tb_2O_3 ceramics reached 154–495 $rad \cdot T^{-1} \cdot m^{-1}$ at the wavelength range of 633–1064 nm. The thermal lens effect of $(Tb_{0.6}Y_{0.4})_2O_3$ ($1/f$ = 0.40 m^{-1}) ceramics was slightly worse than that of the TGG crystal ($1/f$ = 0.35 m^{-1}) due to the remained trace amount of Tb^{4+} ions. The laser damage threshold of the fabricated $(Tb_{0.6}Y_{0.4})_2O_3$ ceramics was as high as 18 $J \cdot cm^{-2}$, better than that of TGG (10 $J \cdot cm^{-2}$), and they were resistant to pulsed laser damage (pulse width = 50 ps, power density = 78 $MW \cdot cm^{-2}$, and no damage during a 7000 h of durability test at 2 MHz). The extinction ratios of $(Tb_{0.6}Y_{0.4})_2O_3$ (8 mm) and Tb_2O_3 (5.1 mm) ceramic samples were 42 and 47 dB, respectively, higher than that of the TGG crystal (35 dB, 20 mm). The thermal conductivity and refractive indexes of TYO ceramics with different Tb concentrations were discussed. The thermal conductivity of TYO ceramics with Tb concentrations of 50%–100% was about 3.3–4.6 $W \cdot m^{-1} \cdot K^{-1}$, comparable to that of the commercial TGG single crystals. The thermal conductivity and the refractive index both increased with the increase of Tb concentration.

The research on Tb_2O_3-based ceramics in China began in 2019. Zhang *et al*. [223] reported the phase

transformation process of Tb_2O_3 at elevated temperatures under different atmospheres. When heating in air, Tb_2O_3 was firstly oxidized to $TbO_{1.81}$ at 500 ℃, and then deoxidized to $TbO_{1.714}$ at 600 ℃ and Tb_2O_3 at 988 ℃. $TbO_{1.81}$ rather than Tb_2O_3 was the most stable phase at room temperature. When calcined in vacuum, the reversible phase transition of Tb_2O_3 above 1600 ℃ made Tb_2O_3 crack from inside to outside. This work provides a deep understanding of controlling and avoiding the phase transformation of Tb_2O_3. In 2021, novel $(Tb_{1-x}Lu_x)_2O_3$ magneto-optical transparent ceramics were prepared by the solid-solution method via vacuum sintering and HIP [24]. The $(Tb_{1-x}Lu_x)_2O_3$ solid solution was formed during the vacuum pre-sintering period, and it could also effectively stabilize under high temperatures. As shown in Fig. 20(a), the in-line transmittance of the polished $(Tb_{0.5}Lu_{0.5})_2O_3$ ceramics with the thickness of 3 mm reached 73.6% at 633 nm and 78.8% at 1064 nm, and still needed to be improved. The Verdet constant of 50% Lu-doped ceramics was −224.33 rad·T^{-1}·m^{-1} at room temperature, which was 30% higher than that of TAG and nearly half of that of pure Tb_2O_3. The Verdet constant increased linearly with the increase of Tb^{3+} concentration, as shown in Fig. 20(c). The thermal conductivity of $(Tb_{0.5}Lu_{0.5})_2O_3$ ceramics was 5.88 W·m^{-1}·K^{-1} at room temperature, a little lower than that of TAG and higher than that of the $(Tb_{1-x}Y_x)_2O_3$ magneto-optical ceramics reported in Ref. [222]. When the Lu_2O_3 concentration was below 50%, the thermal conductivity at room temperature changed between 5.5 and 6.2 W·m^{-1}·K^{-1}, and then increased with the further increase of Lu_2O_3. Xin *et al*. [224] fabricated $(Tb_{0.7}Lu_{0.3})_2O_3$ ceramics and studied the effect of ZrO_2 doping contents on the microstructures

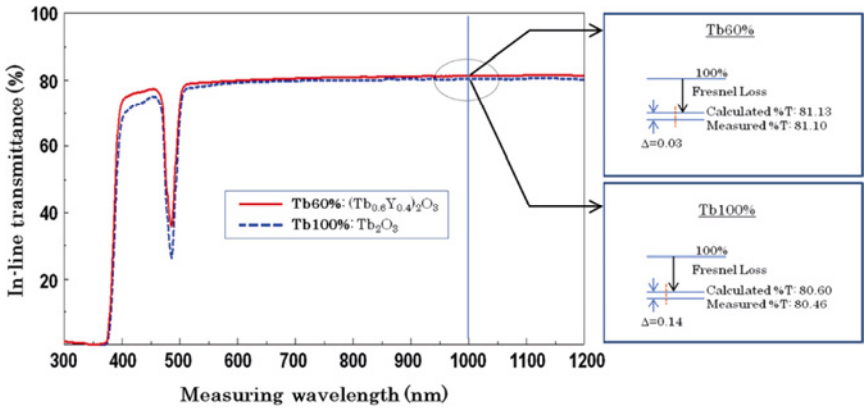


Fig. 19 In-line transmittance curves of $(Tb_{0.6}Y_{0.4})_2O_3$ and Tb_2O_3 ceramics (sample thickness = 5 mm). Reproduced with permission from Ref. [222], © the authors 2019.

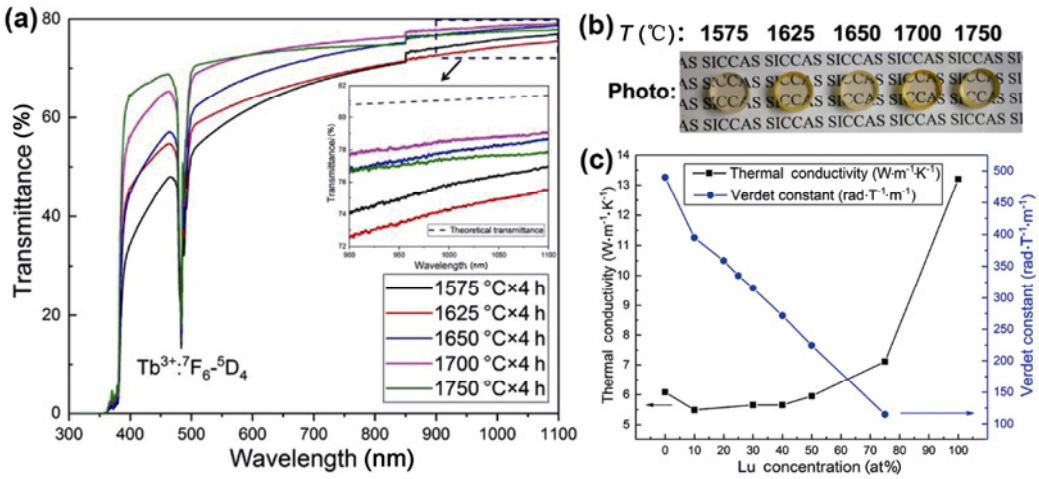


Fig. 20 (a) Optical transmittance spectra and (b) photographs of $(Tb_{0.5}Lu_{0.5})_2O_3$ transparent ceramics vacuum pre-sintered under different temperatures combined with HIP post-treatment at 1600 ℃ and double-side polished to 3 mm; (c) thermal conductivity and Verdet constant of $(Tb_{1-x}Lu_x)_2O_3$ ceramics vs. Lu concentration. Reproduced with permission from Ref. [24], © Elsevier Ltd. 2020.

and optical properties of ceramics. The results showed that the optimal ZrO_2 concentration was 3 at%, at which the in-line transmittance of $(Tb_{0.7}Lu_{0.3})_2O_3$ ceramics was 74.84% at 1064 nm, and the Verdet constant value was 275.58 rad·T^{-1}·m^{-1}.

In 2019, Yang *et al*. [225] prepared the $(Tb_{0.5}Y_{0.5})_2O_3$ transparent ceramics by the wet chemical co-precipitation method and the flowing H_2 atmosphere sintering without milling, sintering aids, or annealing. The prepared $(Tb_{0.5}Y_{0.5})_2O_3$ ceramics with a crystalline size of 35 μm and some micro-pores showed good transmittance from visible to near-IR range, reaching 67.5% at 632.8 nm and 71.9% at 1400 nm. The Verdet constant of $(Tb_{0.5}Y_{0.5})_2O_3$ ceramics at 633 nm was measured to be −220.19 rad·T^{-1}·m^{-1}, 1.64 times that of TGG single crystal. In 2023, Qi *et al*. [226] used lanthana (La_2O_3) as the sintering aid and Lu_2O_3 as the phase stabilizer, fabricating $(Tb_{0.8}Lu_{0.16}La_{0.04})_2O_3$ ceramics from wet co-precipitation nano-powders and by pressureless sintering in a H_2 atmosphere. The transmittance of Φ10 mm × 1 mm specimen reached 79.1% at 1400 nm (an optical loss of about 0.22% cm^{-1}) and 76.6% at 633 nm, and they fabricated ceramic specimens with different dimensions. The Verdet constant value of $(Tb_{0.8}Lu_{0.16}La_{0.04})_2O_3$ ceramics was measured to be 354 rad·T^{-1}·m^{-1}, which was 2.64 times that of TGG single crystals.

By introducing Y_2O_3 or Lu_2O_3 to form the solid solution of $(Tb_{1-x}R_x)_2O_3$ (R = Y or Lu), the lattice structure of Tb_2O_3 cell is effectively stabilized, and the phase transition temperature is raised. However, the occupation of non-magnetic active ions of Y^{3+} or Lu^{3+} leads to the decrease of Verdet constant. Pure Tb_2O_3 ceramics are possible to be obtained below the phase transition temperature by using the nano-powders with high sintering activity. In 2022, Tb_2O_3 nano-powders with high sintering activity were prepared by the liquid precipitation method with air calcination and subsequent reduction in the NH_3 flowing [227]. The two-dimensional needle- or flake-shaped precursor was transformed into the uniform particles with a near-spherical shape and an average particle size of 135 nm, as presented in Figs. 21(a)–21(c). Without RE ion doping, pure Tb_2O_3 ceramics with high optical quality and high Verdet constants were obtained via a two-step sintering method (< 1600 ℃). The Tb_2O_3 ceramics with 1.0 mm in thickness showed high in-line transmittance: 79.4% at 1400 nm, 78.1% at 1064 nm, and 70.3% at 633 nm, as shown in Fig. 21(d). The corresponding FESEM micrograph of the etching surface for Tb_2O_3 transparent ceramics is shown in Fig. 21(e). No secondary phase or abnormal growth existed, and the average grain size is only about 1.3 μm. There are some intergranular closed pores of nano-size seated at the trigeminal grain boundaries. The wavelength dependence of Verdet constant was measured at room temperature, as shown in Fig. 21(f). The Verdet constants of the obtained Tb_2O_3 ceramics were measured to be −427.3 rad·T^{-1}·m^{-1} at 633 nm and −123.7 rad·T^{-1}·m^{-1} at 1064 nm at room temperature, 3.1 and 3.4 times larger than those of the commercial TGG single crystal, respectively.

In 2022, the production of Tb_2O_3-based ceramics for Faraday isolators for 1.03 μm fiber lasers was launched at the IPG IRE-Polus, Russia. Figure 22 shows the photograph of Tb_2O_3 ceramics. The magneto-optical elements have a Verdet constant of −110 rad·T^{-1}·m^{-1}, are installed in lasers up to 10 W, and provide an isolation ratio of 25 dB in a wide temperature range of 20–45 ℃ with a loss of no more than 0.7 dB. To the best of our knowledge, this is the first mass production of magneto-optical ceramics. The interest of the world leader of the high-power fiber laser industry in Tb_2O_3 ceramics confirms its high potential.

Tb_2O_3 ceramics, owing to the great application prospects in a laser system, have attracted a lot of attention. Many researches on the fabrication and properties of Tb_2O_3 ceramics have been carried in recent years. Breakthroughs have achieved in application fields at present. However, it is clear that enhancing the allowable laser power of Faraday insulators on Tb_2O_3 ceramics requires increasing its size and reducing losses. This may be a challenge to achieve a balance between the absence of both oxygen vacancies and Tb^{4+} while maintaining high optical quality. Therefore, it seems that Tb_2O_3 ceramics are more suitable for miniaturizing and compact isolator devices, and in-depth studies of this material are forthcoming.

3.2 Dy_2O_3 ceramics

Tb_2O_3-based magneto-optical materials used in the visible and near-IR wavelength range have the highest Verdet constant. Because of the cost advantage, Dy_2O_3 and Ho_2O_3 sesquioxides also have the possibility to be used in this wavelength range despite of the lower Verdet constant. However, the most promising wavelength range of Dy_2O_3 and Ho_2O_3 is mid-IR, at which the Tb-based materials have absorptions,

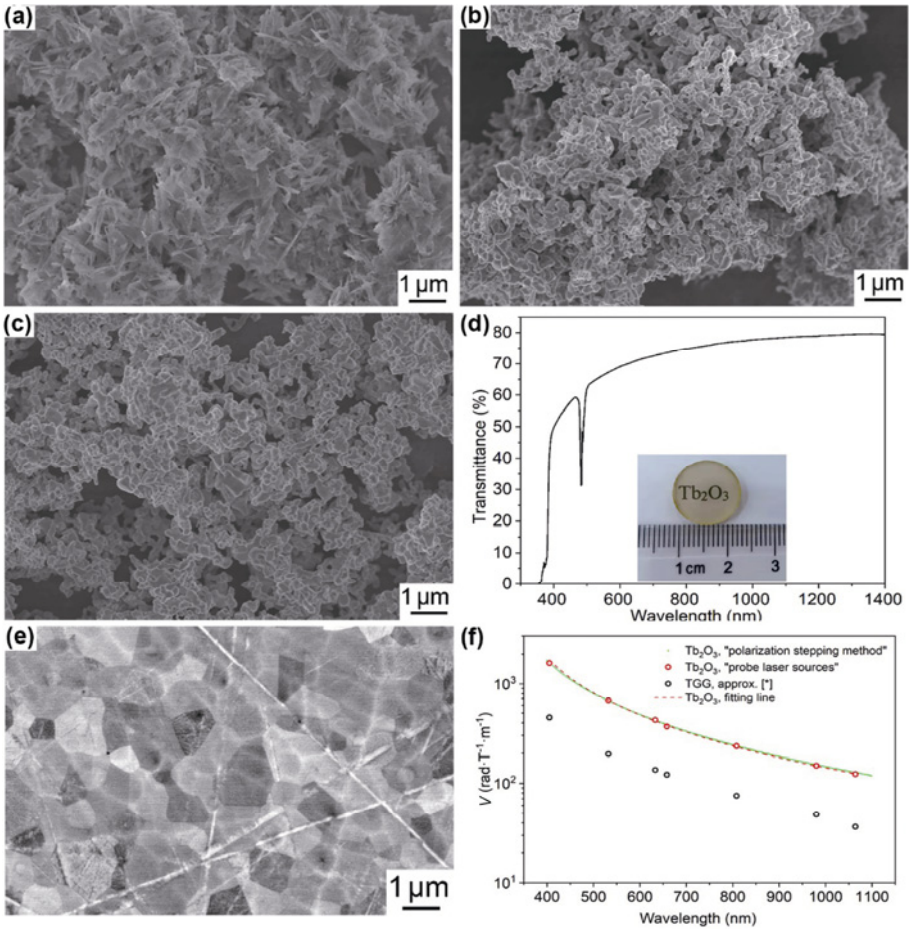


Fig. 21 FESEM images of (a) precursor, (b) air-calcined powders, and (c) Tb_2O_3 powders; (d) photograph and in-line transmission curve of synthesized Tb_2O_3 ceramics (thickness = 1.0 mm); (e) FESEM micrograph of surface of Tb_2O_3 ceramics; and (f) wavelength dependence of Verdet constant of Tb_2O_3 ceramics (the green dot and red circle) and TGG single crystal (the black circle). Reproduced with permission from Ref. [227], © the authors 2022.



Fig. 22 Photograph of Tb_2O_3 ceramics from IPG IRE-Polus.

Dy_2O_3 of 1.9–2.1 μm and Ho_2O_3 of 1.5 μm. Dy_2O_3 is considered to be a promising magneto-optical material with the second highest Verdet constant next to the Tb_2O_3. Dy_2O_3 ceramics were firstly mentioned in the pattern of the Konoshima Chemical Co. Ltd. in 2004 [228]. In 2011, Morales *et al*. [229] explored the current active pressure-assisted densification (CAPAD) for the production of nanocrystalline Dy_2O_3 with excellent magneto-optical properties. The crystallite grain size of the Dy_2O_3 transparent polycrystalline materials with the in-line transmittance of ~50% at 633 nm was in nanometer regime (< 100 nm). The value of measured Verdet constant was > 300 rad·T^{-1}·m^{-1} at 632.8 nm, more than twice that of TGG materials. The Dy_2O_3 ceramics have strong absorption at about 1 μm ascribed to $^6H_{15/2}$ to $^6H_{7/2}$ and $^6F_{9/2}$ energy transition, and thus Dy_2O_3 is inappropriate to use in the Yb- or Nd-based laser system.

In 2018, Snetkov *et al*. [230] reported dysprosium oxide-based ceramics ($(Dy_xY_{0.95-x}La_{0.05})_2O_3$, x = 0.7, 0.85, and 0.9) produced by high-temperature vacuum sintering and annealing from the highly dispersed submicron powders synthesized by SHS. The transparency of the $(Dy_xY_{0.95-x}La_{0.05})_2O_3$ ceramics increased, the amount of secondary phase decreased with the increase of the Y fraction, and $(Dy_{0.7}Y_{0.25}La_{0.05})_2O_3$ ceramics

with no secondary phase presented the best optical transparency and reached more than 70% transmittance in all the transparency windows: 500–730, 1900–2300, and 3500–7500 nm. However, the transmittance decreased significantly with the increasement of thickness. The Verdet constant of $(Dy_xY_{0.95-x}La_{0.05})_2O_3$ ceramics depended linearly on the concentration of Dy^{3+} ions and increased with the increase of Dy^{3+} ions, about twice that of TGG materials in visible and mid-IR ranges. Reference [230] proposes the promising candidate (Dy_2O_3) for Faraday devices used in the visible lasers and Tm^{3+} and Ho^{3+} lasers. The temperature dependence of the Verdet constant for $(Dy_xY_{0.95-x}La_{0.05})_2O_3$ (x = 0.7, 0.85, and 0.9) ceramics in the temperature range of 80–294 K at the wavelength range of 405–1064 nm was then described in Ref. [231], as shown in Fig. 23. The cryogenic cooling led to the increase in about 3.46 times of the Verdet constant, as shown in Eq. (2).

In 2019, Slezák *et al*. [232] measured the complete temperature and wavelength dependence of the Verdet constant of Dy_2O_3 transparent ceramics with the temperature range of 20–297 K and wavelength range from visible 0.6 μm to mid-IR 2.3 μm. These researches are beneficial to the creation of Faraday isolators working with cryogenic cooling for the laser operating in the transparent windows (visible and mid-IR range) of Dy_2O_3-based ceramics. In 2020, $(Dy_{0.7}Y_{0.25}La_{0.05})_2O_3$ ceramics also realized transparent by the pressureless sintering in a reductive H_2 atmosphere (PLSH) using the powders from SHS by Zhou *et al*. [233]. The transmittance values at 2000 nm reached 78%. However, the transmittance in the visible range is relatively low due to the nanoscale-submicron defects and abnormal grain growth. The FoM (= V/α_0) of the obtained $(Dy_{0.7}Y_{0.25}La_{0.05})_2O_3$ ceramics was 0.66584 rad·T^{-1} (38.15 (°)·T^{-1}), presenting good prospects for magneto-optical applications.

The reported optical quality and sizes of the Dy_2O_3 transparent ceramics are not enough for the practical application. There are urgent needs for the preparation of Dy_2O_3 ceramics with higher optical quality and larger sizes. In 2020, Aung *et al*. [234] fabricated Dy_2O_3 ceramics with a large dimension by vacuum pre-sintering and HIP post-treatment using 0.1% ZrO_2 as the sintering aid to suppress grain growth during sintering. The pictures of Dy_2O_3 ceramics are presented in Figs. 24(a) and 24(b). The difference of in-line transmittance of the prepared Dy_2O_3 ceramics

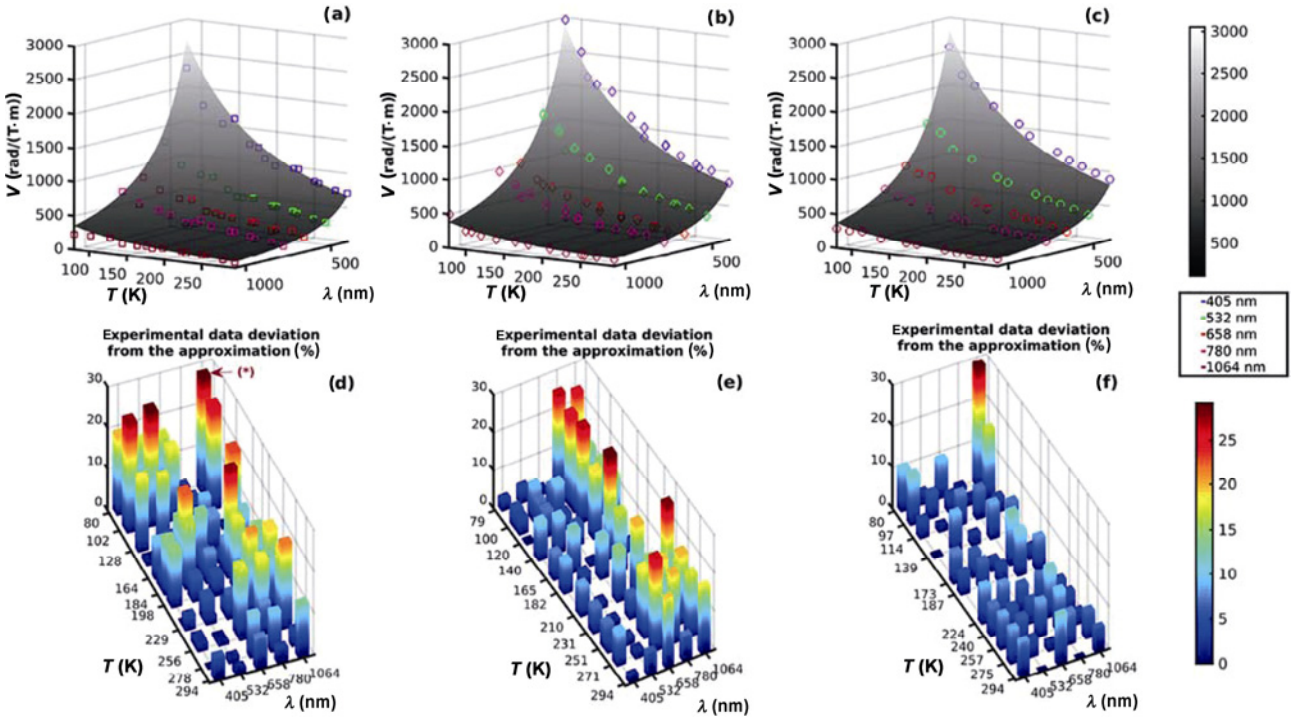


Fig. 23 *T*–*λ* dependence of *V* for $(Dy_xY_{0.95-x}La_{0.05})_2O_3$ samples (dots): (a) x = 0.7; (b) x = 0.85; and (c) x = 0.9. (d–f) Approximation and deviation (in %) between experimental dots and approximation. The symbol "*" shows the 55% experimental data deviation from the approximation at 80 K at 1064 nm. Reproduced with permission from Ref. [231], © Acta Materialia Inc. 2018.

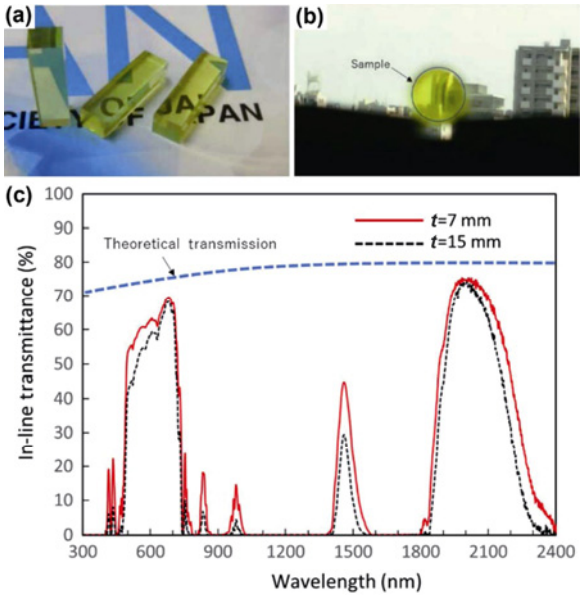


Fig. 24 (a) Appearance of produced Dy_2O_3 ceramics; (b) outside view via Dy_2O_3 ceramics with t = 15 mm; and (c) transmission spectra of Dy_2O_3 with different t: t = 7 mm (the solid line) and t = 15 mm (the dashed line). Reproduced with permission from Ref. [234], © Optical Society of America 2020.

with thicknesess between 8 and 15 mm was only 0.05% at the wavelengths between 680 and 2000 nm, as shown in Fig. 24(c). The Dy_2O_3 ceramics composed of uniform grains of 2–3 μm presented a Verdet constant of −422 rad·T^{-1}·m^{-1} at 633 nm and a large extinction ratio of 34 dB. When constructing a compact isolator device using the Dy_2O_3 ceramics, the needed length of ceramics was only 1.6 mm with a magnetic field of 1.16 T at 633 nm.

The reports about the fabrication of Dy_2O_3 ceramics above are mostly using La_2O_3 or ZrO_2 as sintering aids, which may increase the optical absorption and reduce the thermal conductivity and the Verdet constant. Hu *et al*. [235] prepared the pure Dy_2O_3 transparent ceramics by vacuum sintering from Dy_2O_3 nano-powders synthesized by the liquid precipitation method without any sintering aids. The influences of the calcination temperatures on the morphologies and phase compositions of Dy_2O_3 powders and the optical quality of Dy_2O_3 ceramics were studied in that work. Dy_2O_3 powders calcined at 1000 ℃ for 4 h had an average particle size of 143.2 nm and was superior for the fabrication of Dy_2O_3 ceramics, and the FESEM micrograph is shown in Fig. 25(a). The in-line transmittance values of the optimal Dy_2O_3 ceramics (1.0 mm thick) were 67.9% and 75.3% at the wavelength of 633 and 2000 nm, respectively, presenting a relatively high transmittance, as presented in Fig. 25(c). The large grain size of Dy_2O_3 transparent ceramics, as shown in Fig. 25(d),

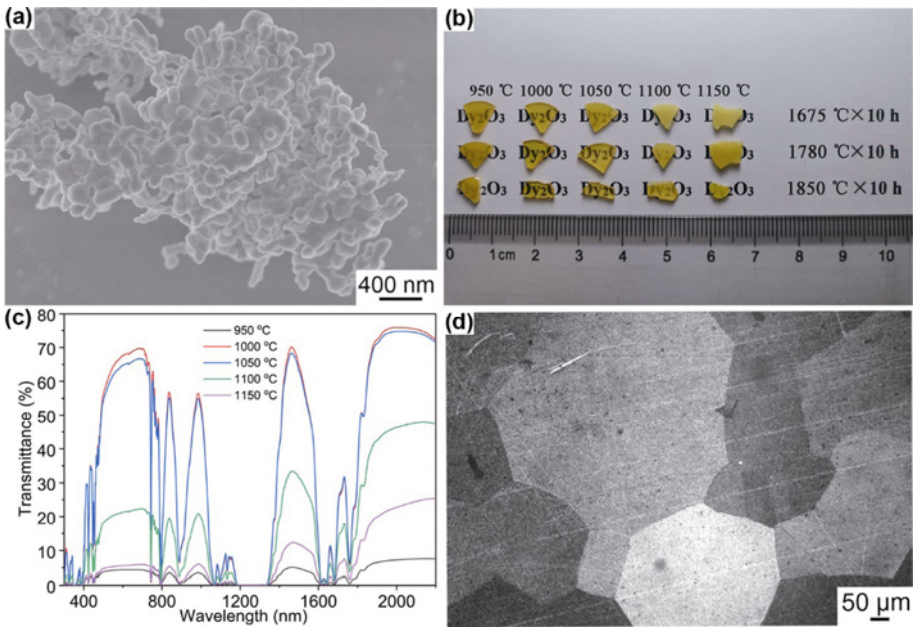


Fig. 25 (a) FESEM image of 1000 ℃-calcined Dy_2O_3 powders; (b) photographs of Dy_2O_3 ceramics sintered at 1675–1850 ℃ for 10 h and air annealed at 1400 ℃ for 10 h from 950–1150 ℃-calcined Dy_2O_3 powders; (c) in-line transmittance curves of Dy_2O_3 ceramics sintered at 1850 ℃ for 10 h and air annealed at 1400 ℃ for 10 h from 950–1150 ℃-calcined Dy_2O_3 powders; and (d) FESEM micrograph of Dy_2O_3 ceramics sintered at 1850 ℃ for 10 h and air annealed at 1400 ℃ for 10 h from 1000 ℃-calcined Dy_2O_3 powders. Reproduced with permission from Ref. [235], © the authors 2020.

was ascribed to the high sintering temperature and the high sintering activity of the as-synthesized Dy_2O_3 nano-powders. The Verdet constant was measured to be −325.3 rad·T^{-1}·m^{-1} at 633 nm, 2.4 times larger than that of TGG single crystals. High optical quality and large Verdet constants make Dy_2O_3 transparent ceramics promising for the Faraday isolator used in visible and 2 μm range. However, the aperture is not sufficient for the practical application and still need to be increased.

The optical quality and the magneto-optical properties of Dy_2O_3 ceramics are the most discussed. Nevertheless, when applied in high-power laser systems, the materials also need to have more strict requirements: the high thermal conductivity and other characteristics such as certain parameters of P, Q, and ξ and the mechanical properties. Balabanov *et al*. [236] prepared the Dy_2O_3- and Ho_2O_3-based ceramics by hot pressing from the improved SHS powders by preliminary calcination and planetary milling. They investigated the thermal conductivity, linear thermal expansion coefficient, microhardness (*HV*), elastic modulus (*E*), and crack resistance (K_{IC}). The measured characteristics of $(Dy_{0.7}Y_{0.25}La_{0.05})_2O_3$ ceramics were as following: *HV* = 7.2±0.5 GPa, *E* = 173±3 GPa, K_{IC} = 0.81± 0.09 MPa·m$^{0.5}$, k = 3.0±0.2 W·m^{-1}·K^{-1} at room temperature, and coefficient of linear thermal expansion (α) = 8.21×10^{-6} K^{-1}. The in-line transmittance of the $(Dy_{0.7}Y_{0.25}La_{0.05})_2O_3$ ceramics with a thickness of 4.5 mm was 72% at 4.5 μm and do not exceeded 55% at the visible range due to the high scattering of the pores. This work proposes a detailed description of the synthesis by HP and increased the thickness of ceramicsl; however, further improvement of the optical quality is needed.

At present, the reports about Dy_2O_3 transparent ceramics mainly focus on the preparation and the property study. Though researches have confirmed that Dy_2O_3 transparent ceramics are promising materials used in mid-IR range, there are no Dy_2O_3 ceramics with high optical quality available for practical applications. In current studies, the optical quality of Dy_2O_3 ceramics still needs to be further improved, especially in the visible range. In the near future, with the mass production of Dy_2O_3 transparent ceramics with high optical quality, it is believed that the magneto-optical devices based on Dy_2O_3 ceramics will be developed soon.

3. 3 Ho_2O_3 ceramics

Besides the discussed Tb_2O_3 and Dy_2O_3 materials, Ho_2O_3 also presents great application potential for Faraday devices in about 1 μm high-average power lasers and 1.5 μm telecom lasers due to its appropriate transparent windows and the relatively low cost. The fabrication and characterization of magneto-optical properties of transparent Ho_2O_3 ceramics were firstly reported in 2017 by Furuse and Yasuhara [237]. The transparent Ho_2O_3 ceramics fabricated by spark plasma sintering (SPS) and air annealing from commercial Ho_2O_3 powders had an in-line transmittance of 58% at 1064 nm (thickness = 0.6 mm), much lower than the ideal transmittance of 81.3% at 1064 nm. The Verdet constants of Ho_2O_3 ceramics were −178.1 and −46.3 rad·T^{-1}·m^{-1} at 600 and 1064 nm, respectively, and was 1.3 times higher than that of TGG and close to that of TAG ceramics at 1064 nm. After the publication of Ref. [237], the research upsurge of Ho_2O_3 ceramics has started. In 2018, Voina *et al*. [238] investigated the temperature dependence of the Verdet constant of Ho_2O_3 ceramics, as well as the Verdet constant dispersion of Ho_2O_3 and Ho_2O_3 ceramics doped with Tb^{3+} (0.2 at%) and Ce^{3+} (0.1 at%) in the wavelength range of 0.5–1 μm and 1064 nm, as shown in Fig. 26. The results showed that the relatively low doping concentration had no significant boosting impact on the Faraday effect in Ho_2O_3 materials.

In 2019, Lu *et al*. [239] prepared the Ho_2O_3 transparent ceramics with an in-line transmittance of 73% at 1000 nm (1.0 mm thick) and an average grain size of 28 μm by vacuum sintering. The highly sinterable Ho_2O_3 powders obtained from the freezing-temperature co-precipitation method showed an average particle size of 48 nm and a narrow particle size distribution. Subsequently, Cheng *et al*. [240] deepened the research and fabricated Ho_2O_3 ceramics by vacuum sintering using the self-reactive resultant HoOF as the sintering aid. The obtained Ho_2O_3 ceramics had the in-line transmittance of 72% at 1550 nm and Verdet constants of −182±8, −46±3, and −22±2 rad·T^{-1}·m^{-1} at 633, 1064, and 1550 nm, respectively, comparable to those of the previous reports, indicating that the F-additive had no significant impact on the Faraday effect of Ho_2O_3 ceramics. The FoM, which presented the magneto-optical properties of the materials, was abnormally low at 633 nm due to the high absorption caused by the intra-4f^{10} transition of Ho^{3+}, leading the application limitation at the visible range.

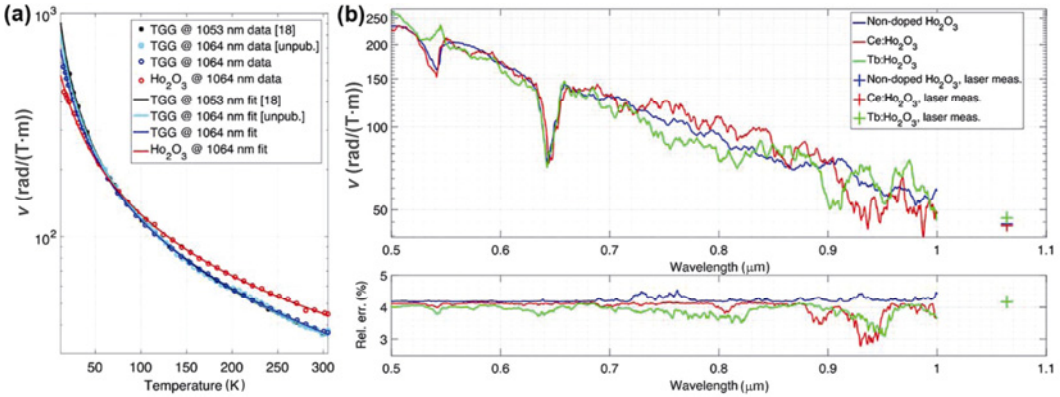


Fig. 26 (a) Results for laser measurement of Verdet constant temperature dependence of Ho_2O_3 ceramics; (b) Verdet constant dispersion of Ho_2O_3 ceramic-based MO materials. Reproduced with permission from Ref. [238], © The Author(s) 2018.

The increase of Verdet constant by the co-doping of Ce^{3+}, Pr^{3+}, Ho^{3+}, Nd^{3+}, Dy^{3+}, Tm^{3+}, or Ti^{3+} ions has been reported in TGG and TAG materials. According to the Ho_2O_3–Dy_2O_3 phase diagram, Dy_2O_3 and Ho_2O_3 can dissolve in any proportion to form continuous solid solution. In 2021, Lu *et al*. [241] fabricated the binary $(Ho_{1-x}Dy_x)_2O_3$ (x = 0.01–1) ceramics to investigate the possible superexchange interaction. The $(Ho_{1-x}Dy_x)_2O_3$ (x = 0.01–1) ceramics prepared by vacuum sintering from layered rare-earth hydroxide (LRH) compounds of $(Ho,Dy)_2(OH)_5NO_3{\cdot}nH_2O$ precursor had in-line transmittance of 67%–77% at 700 nm and 77%–84% at 5.5 μm. The Verdet constant of $(Ho_{1-x}Dy_x)_2O_3$ ceramics increased with the increase of Dy^{3+} content, and the Verdet constant at 533 nm was about 1.2, 1.35, 1.4, 1.7, 2.1, and 2.2 times higher than those of the commercial TGG single crystal with x = 0.01, 0.1, 0.25, 0.5, 0.75, and 1, respectively. The superexchange interaction was not found in the $(Ho_{1-x}Dy_x)_2O_3$ ceramics.

Highly dispersed nano-powders with high activity are one of the key points for the fabrication of transparent ceramics with high optical quality. Besides, sintering aids also contribute to forming the desired faultless microstructure of ceramics. In 2019, Balabanov *et al*. [242] prepared the weakly agglomerated $(Ho_{1-x}La_x)_2O_3$ powders by the SHS and the following air annealing, ball milling, and sedimentation. In 2020, $(Ho_{1-x}La_x)_2O_3$ transparent ceramics were prepared by vacuum sintering using the $(Ho_{1-x}La_x)_2O_3$ nano-powders by the SHS method to investigate the influence of lanthanum on the ceramic microstructure [243]. All the $(Ho_{1-x}La_x)_2O_3$ ceramics showed the secondary phase grains both at the boundary and the triple points. The amount of secondary phase increased, and the grain size decreased with the increase of the La_2O_3 concentration. After annealing, the secondary phase had vanished completely, but the lanthanum (La) content at the boundaries slightly increased compared with that at the unannealed samples. Annealing at high temperatures could lead to the elimination of secondary phase and the increase of transparency of the $(Ho_{1-x}La_x)_2O_3$ ceramics. The 5% La:Ho_2O_3 ceramics prepared by vacuum sintering had a transmittance of 76% at 1 μm with 1.0 mm in thickness [244] and 1.3-time larger Verdet constant values than TGG in the entire measured range. The adding of La_2O_3 brought only 5% decrease of the Verdet constant at 1064 nm and an increase of the in-line transmittance in the near-IR wavelength range. The prepared Ho_2O_3 ceramics had relatively high mechanical properties (HV = 8.4 GPa, E = 182 GPa, and K_{IC} = 0.95 MPa·$m^{0.5}$).

Later, Balabanov *et al*. [236] consolidated the same 5% La:Ho_2O_3 SHS powders by hot pressing. The sample sizes were significantly larger than those obtained by vacuum sintering and were Φ20 mm × 4.5 mm; the transmittance of the ceramics was 78% at 4.5 μm. The mechanical characteristics of the ceramics were not significantly different from those obtained by vacuum sintering. The thermal conductivity of 5% La:Ho_2O_3 ceramics was k = 4.8±0.2 W·m^{-1}·K^{-1} at 298 K and reached a maximum k (= 7.3 W·m^{-1}·K^{-1}) at 130 K; $\alpha = 8.19\times10^{-6}$ K^{-1}.

In 2020, Hu *et al*. [245] fabricated pure Ho_2O_3 ceramics by vacuum sintering plus HIP post-treatment without any sintering aids. The influences of pre-sintering temperature and the HIP temperature on the microstructure and optical quality of Ho_2O_3 ceramics were studied. The optimal Ho_2O_3 ceramics with an average grain size of 0.77 μm presented a high

in-line transmittance: 80.7% at 1550 nm and 76.7% at 1064 nm, as shown in Fig. 27(a), and the corresponding ceramic micrograph is shown in Fig. 27(b). The wavelength dependence of Verdet constant for Ho_2O_3 ceramics were measured at room temperature, as presented in Fig. 27(e). The Verdet constant of Ho_2O_3 ceramic sample showed large values: −47.4 rad·T^{-1}·m^{-1} at 1064 nm and −15.4 rad·T^{-1}·m^{-1} at 1561 nm, 1.3 and 1.7 times that of TGG, respectively. The decrease of in-line transmittance with the decrease of wavelength is usually due to the oxygen vacancy defects caused by vacuum sintering or the pores with nano-size in the ceramics. The air annealing temperature had an important effect on the optical quality and microstructures of Ho_2O_3 ceramics, and the in-line transmittance curves of Ho_2O_3 ceramics with different annealing temperature are presented in Fig. 27(c). The in-line transmittance was further decreased after air annealing due to the expansion of the compressed nano-pores formed during HIP process, as displayed the microstructure of 1200 ℃ air-annealed Ho_2O_3 ceramics (Fig. 27(d)), which needed to be further improved. The high transparency and large Verdet constant make Ho_2O_3 a promising candidate for the Faraday devices used in ~1 μm (lasers based on Yb- and Nd-doped materials) or 1.3 and 1.5 μm (telecom lasers based on Er-doped materials).

In general, the current reports about Ho_2O_3 ceramics mainly focus on the improvement of optical quality. However, the size of the reported Ho_2O_3 ceramics or the optical quality of the large-sized Ho_2O_3 ceramic samples is still unsatisfactory and far from the application

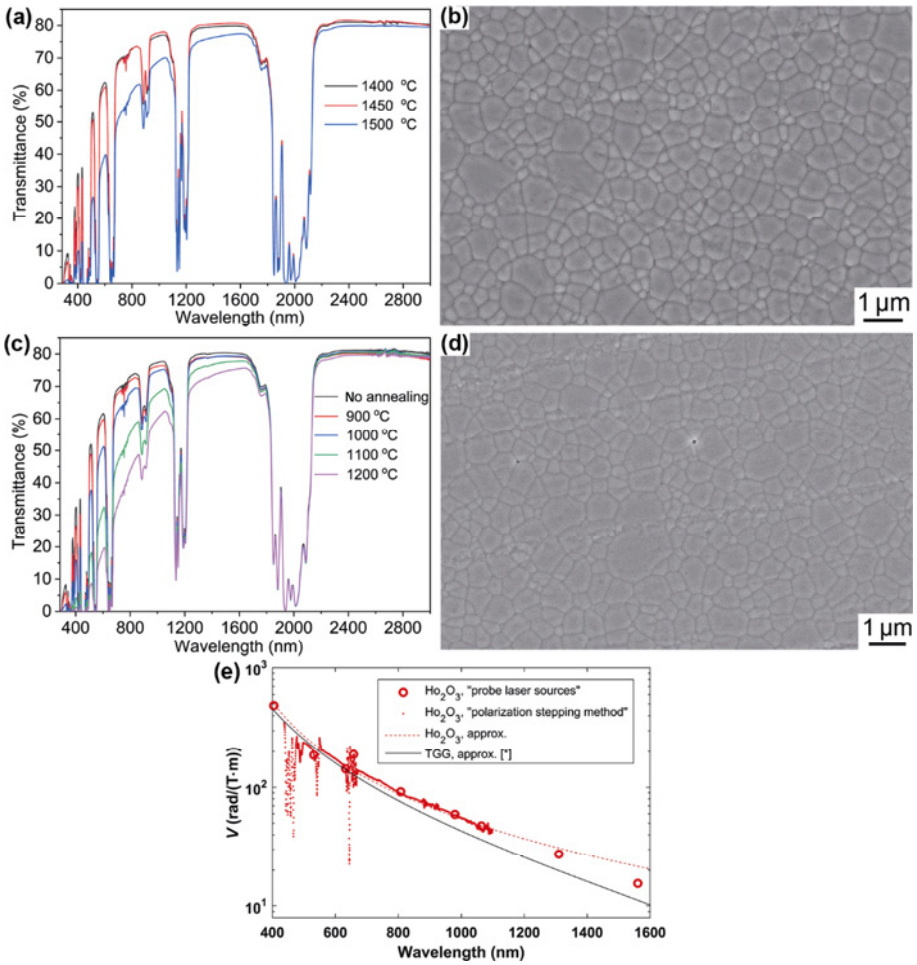


Fig. 27 (a) In-line transmittance curves of Ho_2O_3 ceramics pre-sintered at 1250 ℃ for 2 h and HIP post-treated at 1400–1500 ℃ for 3 h (1.0 mm thick); (b) FESEM image of thermally etched surfaces of Ho_2O_3 ceramics pre-sintered at 1250 ℃ for 2 h with HIP post-treated at 1450 ℃ for 3 h; (c) in-line transmittance curves of Ho_2O_3 ceramics before and after annealing at 900–1200 ℃ for 10 h (0.9 mm thick); (d) FESEM image of Ho_2O_3 ceramics after air annealing at 1200 ℃ for 10 h; and (e) wavelength dependence of Verdet constants of Ho_2O_3 ceramics at 400–1600 nm. Reproduced with permission from Ref. [245], © Elsevier Ltd. 2020.

requirements. In addition, there is no research on the thermo-optical properties of Ho_2O_3 ceramics, including thermo-optical constant and thermally-induced depolarization. As one of the excellent candidate materials that can be applied in the 1.5 μm telecom laser, the comprehensive properties of Ho_2O_3 materials need more research to further evaluate its application potential.

3.4 Er_2O_3 ceramics

As a magnetically active element, Er-based materials can also be employed in the magneto-optical fields. Er_2O_3 transparent ceramics were firstly mentioned in the patent of Konoshima Chemical Co. Ltd. in 2004 [228]. Highly transparent Er_2O_3 ceramics using lanthanum as a sintering aid (0, 3%, 5%, 7%, and 10%) were fabricated by Balabanov *et al*. [246] in 2020. The submicron powders from SHS had cubic single-phases, and were composed of substitutional solid solution of Er_2O_3 and La_2O_3. The 5% La:Er_2O_3 ceramics presented the best combination characteristics: in-line transmittance of 81.3% at 1.8 μm with t = 1.0 mm, HV = 8.6 GPa, E = 190 GPa, K_{IC} = 0.98 MPa·$m^{0.5}$, and k = 6 W·m^{-1}·K^{-1} at 298 K. The magneto-optical properties of Er_2O_3-based ceramics ($(Er_{0.93}La_{0.07})_2O_3$, $(Er_{0.95}La_{0.05})_2O_3$, $(Er_{0.97}La_{0.03})_2O_3$, and Er_2O_3) were reported in Ref. [247]. The transparent windows of La:Er_2O_3 ceramics were near 427, 467, 565–626, 685–780, 851–920, 1030–1370, and 1800–8000 nm. The wavelength dependence of the Verdet constant of Er_2O_3-based ceramics was identified by the polarization-stepping method. The value of $V(Er_2O_3)/V(TGG)$ was about 0.56 at 1064 nm, and the Verdet constant at 1950 nm was about 2.2 less than that of Dy_2O_3. However, the materials like Dy_2O_3 have obvious absorption at 3 μm. Therefore, Er_2O_3-based ceramics having a wide transparent band at 1800–8000 nm range are presenting huge potential for the Faraday application used in 3 μm range.

In conclusion, the reports on Er_2O_3 ceramics mainly focus on the preparation and characterization of fundamental properties, while the reports on the magneto-optical properties are rare. The current researches show that the Verdet constants of Er_2O_3 ceramics at ~1 and 2 μm have no advantages compared with those of other garnet and sesquioxide ceramics. Nevertheless, Er_2O_3 ceramics have a transparent window at 3000 nm, which makes it possible to be applied in this band. More relevant in-depth research on the magneto-optical properties of Er_2O_3 ceramics is in urgent need.

3.5 RE:Y_2O_3 ceramics

Benefited from the high chemical stability, wide optical band gap, large UV–IR transmittance, and low α, Y_2O_3 is usually used as the host material of optical activator. Kruk and Ziewiec focus on the fundamental research of RE:Y_2O_3 ceramics, such as Ce or Pr:Y_2O_3 [248], Sm:Y_2O_3 [249,250], and La,Nd:Y_2O_3 [10] ceramics, and the magneto-optical properties of these ceramics were reported. However, the Verdet constant of the RE:Y_2O_3 ceramics has no superiority compared with that of TGG materials, and the currently reported optical quality of the RE:Y_2O_3 ceramics still needs improvement for application. Kruk and Mrózek [10,11] also proposed to determine the relationship between the wavelength dispersion and Verdet constant around the absorption band by the Kramers–Kronig relation. The measurement and prediction of the Verdet constant across the absorption band may help deepen the understanding of MO effects and instruct the design of future MO materials.

4 $A_2B_2O_7$ magneto-optical ceramics

$A_2B_2O_7$ materials with a pyrochlore or defect fluorite structure have been widely studied for catalyst [251], thermal barrier coating [252], solid oxide fuel cell (SOFC) [253], scintillator [254], fluorescent material [255], nuclear waste immobilization [256], optical lens [257], fundamental physics research [258], etc. $A_2B_2O_7$ MO crystals have also been studied for many years, such as $Ho_2Ti_2O_7$ [259], $Dy_2Ti_2O_7$ [70,260], $Tb_2Ti_2O_7$ [72,261,262], and $Gd_2Ti_2O_7$ [263]. Few $RE_2Hf_2O_7$ or $RE_2Zr_2O_7$ crystals were reported possibly because of the high melting points (> 2000 ℃ [264]). Almost all the reported $A_2B_2O_7$ crystals possess a small size that is generally not sufficient for advanced Faraday isolators. $A_2B_2O_7$ MO ceramics are emerging materials, and only a few researches have studied on them, including $Tb_2Hf_2O_7$-based ceramics, $Tb_2Ti_2O_7$ ceramics, $Ho_2Zr_2O_7$ ceramics, and $Tb_2Zr_2O_7$ ceramics.

4.1 $Tb_2Hf_2O_7$-based ceramics

In 2019, Yasuhara and Ikesue [265] reported $Tb_2Hf_2O_7$ ceramics. The ceramic sample was over 14 mm in

length and 5 mm in diameter. The transmittance of the 14.6 mm sample was 77.5% at 1064 nm, and the transmittance value was almost independent of sample thickness, which indicated that the $Tb_2Hf_2O_7$ ceramic sample possesses high optical quality. The wavelength dependence of the Verdet constant was also investigated. The Verdet constant value of $Tb_2Hf_2O_7$ ceramics was measured to be 50 rad·T^{-1}·m^{-1} at 1064 nm, 1.4 times higher than that of TGG ceramics. Aung *et al*. [266] further improved the optical quality of $Tb_2Hf_2O_7$ ceramics in 2020. The samples were fabricated by the solid-state reaction method. After pre-sintered in vacuum, HIP treated in argon, and annealed in H_2, the obtained $Tb_2Hf_2O_7$ ceramics (Φ6 mm × 15 mm) possessed high optical quality, as shown in Fig. 28. The annealing process helped improve the optical homogeneity and reduce point defect, so the absorption band in 600–1000 nm was eliminated.

According to Eq. (3), the Verdet constant of MO material increases with the increasing N. In $Tb_2Hf_2O_7$ ceramics, there is a large solid solution range of cubic phase, so non-stoichiometric $Tb_2(Hf_{1-x}Tb_x)_2O_{7-x}$ ceramics with higher Tb^{3+} concentrations are expected to be achieved. Zhang *et al*. [267] fabricated $Tb_{2.45}Hf_2O_{7.68}$ ceramics by solid state reactive sintering with HIP post-treatment. The transmittance of $Tb_{2.45}Hf_2O_{7.68}$ ceramics reached 79.4% at 1064 nm (2.0 mm thick), as shown in Fig. 29(a). From the Faraday rotation angle vs. magnetic strength (Fig. 29(b)), the Verdet constant of $Tb_{2.45}Hf_2O_{7.68}$ ceramics at 633 nm was −165.6 rad·T^{-1}·m^{-1}, 23.6% higher than that of TGG crystals and 8.4% higher than that of $Tb_2Hf_2O_7$ ceramics. Zhang *et al*. [268] further investigated the phase composition, densification process, microstructure, optical transmittance, and Verdet constant of $Tb_2(Hf_{1-x}Tb_x)_2O_{7-x}$ ceramics. The Verdet constant of $Tb_2(Hf_{1-x}Tb_x)_2O_{7-x}$ ceramics is −153.4, −155.8, and −181.2 rad·T^{-1}·m^{-1} when x = −0.07, 0, and 0.1 at 633 nm, respectively. The results showed that increasing the Tb^{3+} concentration can enlarge the Verdet constant effectively. When x = −0.07, the transmittance of the sample reached 74.6% at 1064 nm, but the optical quality decreased when x was higher. When $x \geqslant 0.1$, a Tb-rich secondary phase was detected. They noted that further work about the improvement of powder homogeneity, the use of non-reactive sintering method, and the supplements of HfO_2–Tb_2O_3 diagram is well worth consideration.

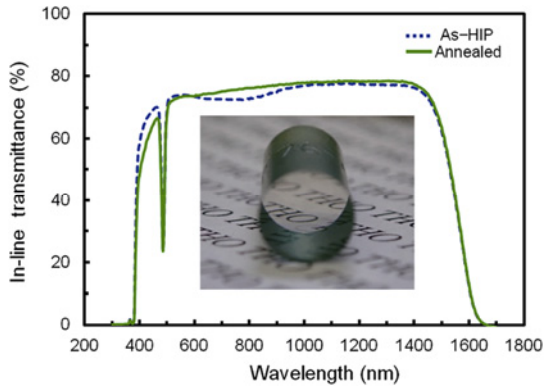


Fig. 28 Transmission spectra of as-HIP sample (the dashed line) and annealed sample (the solid line); the inset is the appearance of produced $Tb_2Hf_2O_7$ ceramics (Φ6 mm × 15 mm). Reproduced with permission from Ref. [266], © Elsevier B.V. 2020.

4. 2 $Tb_2Ti_2O_7$ ceramics

$Tb_2Ti_2O_7$ crystals have been studied and shown an outstanding MO property [72,261,262]. The Verdet constant of $Tb_2Ti_2O_7$ crystal was measured to be −225 rad·T^{-1}·m^{-1} at 633 nm, 68% higher than that of TGG crystals. However, the grown $Tb_2Ti_2O_7$ crystals were in small size, and cracking occurred in some attempts of growing $Tb_2Ti_2O_7$ crystals [72].

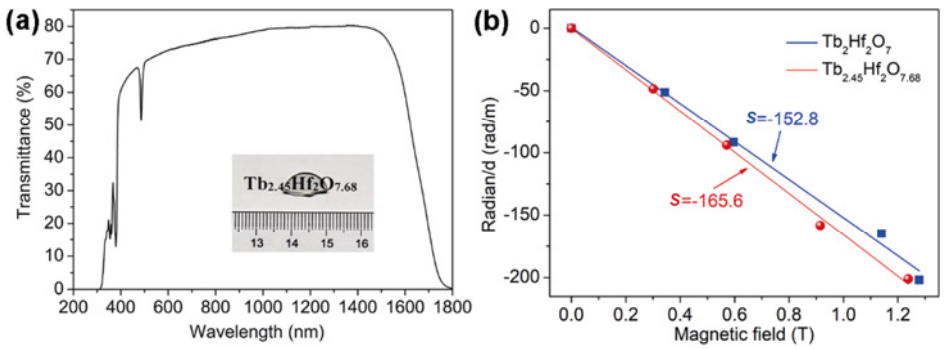


Fig. 29 (a) Photograph and in-line transmittance of $Tb_{2.45}Hf_2O_{7.68}$ ceramics (2.0 mm thick); (b) graph of Faraday rotation angle vs. magnetic strength. Reproduced with permission from Ref. [267], © Acta Materialia Inc. 2021.

In 2021, Zhang *et al*. [269] reported $Tb_2Ti_2O_7$ ceramics from co-precipitated nano-powders. The decomposition of the precursor and the morphology of powders calcined at different temperatures were investigated. After pre-sintered in vacuum, HIP post-treated in argon, and annealed in a NH_3 atmosphere, $Tb_2Ti_2O_7$ ceramics showed a transmittance of 65.5% at 1064 nm (1.5 mm thick), as shown in Fig. 30. The Verdet constant of $Tb_2Ti_2O_7$ ceramics reached −229 rad·T^{-1}·m^{-1} at 633 nm, 71% higher than that of TGG crystals, and the required length of the $Tb_2Ti_2O_7$ ceramics in Faraday isolators can be miniaturized to about 58.5% compared with that using TGG crystals.

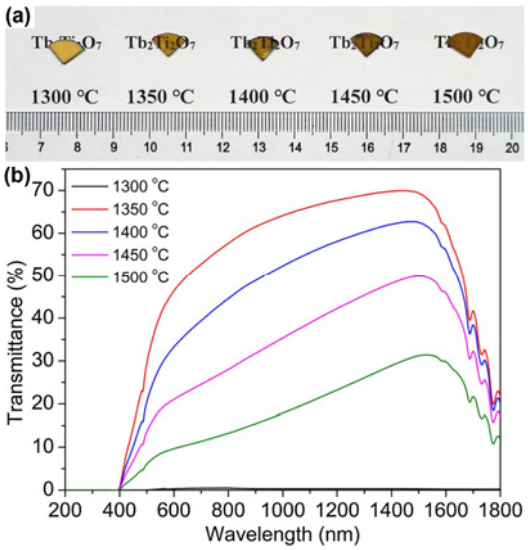


Fig. 30 (a) Photographs and (b) in-line transmittance curves of $Tb_2Ti_2O_7$ ceramics pre-sintered at different temperatures and after HIP and annealing. Reproduced with permission from Ref. [269], © Elsevier Ltd. 2021.

However, it should be noted that the optical quality and the sample size of $Tb_2Ti_2O_7$ ceramics still need further improvement.

4. 3 $Tb_2Zr_2O_7$ ceramics

In 2023, Lai *et al*. [270] reported $Tb_2Zr_2O_7$ ceramics with a defect fluorite structure. The $Tb_2Zr_2O_7$ ceramics were fabricated by a solid-state reaction sintering method in vacuum from Tb_2O_3 and ZrO_2 nano-powders. The obtained specimens with a thickness of 1.1 mm had a transmittance of 76.2% at 635 nm, as shown in Figs. 31(a) and 31(b). According to the refractive index of about 2.1 at 635 nm measured by themselves, the transmittance of the $Tb_2Zr_2O_7$ ceramic samples reached about 98.2% of the theoretical value. They also measured optical basicity (Λ_n) of 0.985± 0.015, and the electronic polarizability of O^{2-} of 2.45±0.06 Å^3 in the $Tb_2Zr_2O_7$ ceramics. Both of them were higher than those of Tb_2O_3 materials. The Verdet constants of the $Tb_2Zr_2O_7$ ceramics were −400, −260, and −62 rad·T^{-1}·m^{-1} at 515, 635, and 1064 nm, respectively, as shown in Fig. 31(c). These values are about 1.9 times of the values of TGG crystals and are much higher than those of the $Tb_2Hf_2O_7$.

4. 4 $Ho_2Zr_2O_7$ ceramics

Hu *et al*. [271] fabricated $Ho_2Zr_2O_7$ MO ceramics by a co-precipitation strategy. Detailed characterization of the precursor and calcined powders were carried out. The optical transmittance, refractive index, Λ_n, MO properties, and thermal properties of $Ho_2Zr_2O_7$ ceramics were studied, as shown in Fig. 32. The transmittance of

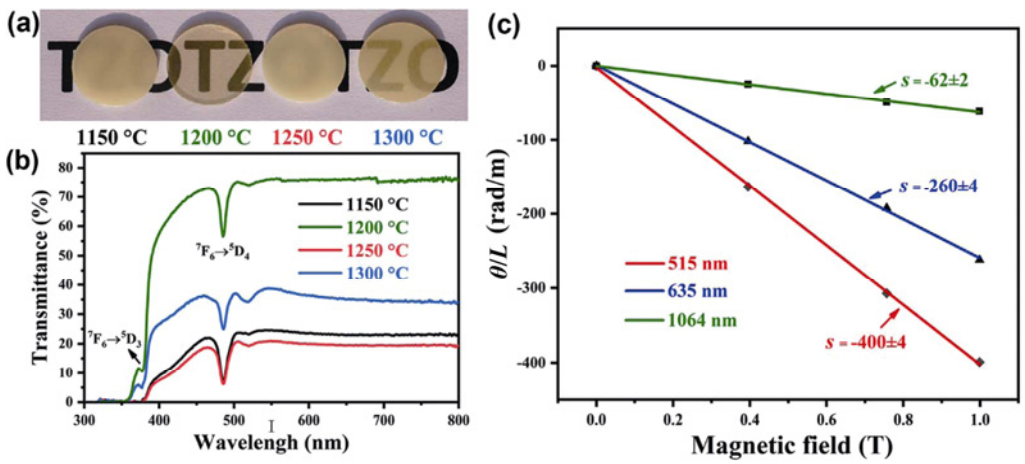


Fig. 31 (a) Photographs and (b) transmittance curves of $Tb_2Zr_2O_7$ ceramics fabricated from powders calcined at different temperatures; (c) θ of $Tb_2Zr_2O_7$ ceramics per length vs. magnetic strength at different wavelengths. Reproduced with permission from Ref. [270], © Acta Materialia Inc. 2023.

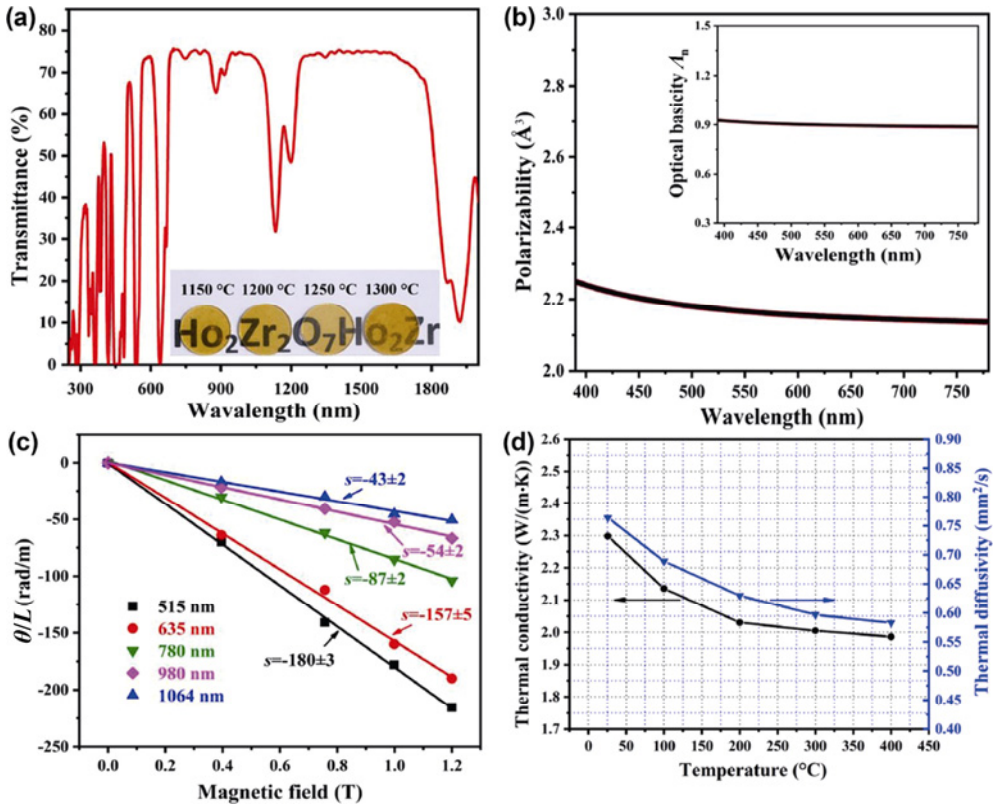


Fig. 32 (a) Photographs and in-line transmittance; (b) O^{2-} polarizability (the inset is Λ_n); (c) θ/L vs. B at different wavelengths; and (d) thermal diffusivity and thermal conductivity of transparent $Ho_2Zr_2O_7$ ceramics. Reproduced with permission from Ref. [271], © Published by Elsevier Ltd on behalf of The editorial office of Journal of Materials Science & Technology 2023.

the $Ho_2Zr_2O_7$ ceramics with a thickness of 0.9 mm reached 74.4% at 1000 nm, which was about 97.4% of the theoretical value. The Λ_n of $Ho_2Zr_2O_7$ ceramics was approximately 0.90, which was lower than that of Ho_2O_3 (0.95). The Verdet constant of $Ho_2Zr_2O_7$ ceramics was comparable with that of Ho_2O_3 and was about 1.2-fold higher than that of commercial TGG crystals, as shown in Fig. 32(c). They noted that a design idea on high-Verdet-constant materials should comprehensively consider Λ_n, the distance between the atoms, the first ionization energy of atom, and the magnetizability. Figure 32(d) shows the thermal conductivity and thermal diffusivity of the $Ho_2Zr_2O_7$ ceramics at different temperatures. The thermal conductivity of $Ho_2Zr_2O_7$ ceramics at room temperature was 2.30 $W \cdot m^{-1} \cdot K^{-1}$, which was lower than those of $(Ho_{0.95}La_{0.05})_2O_3$, HoAG, and TGG materials.

As far as we know, there is little study about the thermo-optical performances of $A_2B_2O_7$ MO ceramics, such as thermo-optical constant, thermally induced depolarization property, and thermal lens performance. In view of the thermal conductivity value of $Ho_2Zr_2O_7$ ceramics reported in Ref. [271] and that of other $A_2B_2O_7$ materials [272], it seems that $A_2B_2O_7$ MO ceramics may possess lower thermal conductivity compared with most of garnet and sesquioxide ceramics. From this perspective alone, $A_2B_2O_7$ ceramics may not be an ideal choice for high-performance Faraday isolators. However, there are other important parameters for the isolator applications, such as optical loss, thermo-optical constant, and thermally induced depolarization property. As an emerging material, more characterizations of these properties are much-needed to further assess the prospects of $A_2B_2O_7$ MO ceramics. In addition, the balance between oxygen vacancies and Tb^{4+} is also necessary to pay attention to $Tb_2Hf_2O_7$, $Tb_2Zr_2O_7$, and $Tb_2Ti_2O_7$ ceramics, which is rarely mentioned and is similar to the problem in Tb_2O_3 ceramics.

5 Conclusions and outlook

This review discusses the research progress of several MO ceramics. Table 1 summarizes the values of the Verdet constant, thermal conductivity, and experimental

P_{las} of paramagnetic MO ceramics. Among the existing MO materials, MO ceramics possess good comprehensive performance, including high Verdet constant, high thermal conductivity, high laser damage threshold, good thermo-optical properties, and outstanding size scalability. In addition, the characteristic of ceramic synthesis technology makes it possible to fabricate high-melting-point materials like Tb_2O_3 and incongruent melting materials like TAG and YIG, and the segregation problem of doping ions is simplified in doped YIG ceramics. Up to now, TGG and TAG ceramics have been proved to be applicable in Faraday isolators operated at the laser power of hundreds to thousands of watts, which means great practical potential. The flexibility of ceramic synthesis technology makes it possible to manufacture MO materials with various properties and select the most suitable one for each specific task. And also, in the future, it will allow replacing existing commercially available MO materials with similar ceramic materials at a lower price or with materials with better properties. However, up to now, there are only a few institutions succeeded in fabricating MO ceramics with applicable optical quality and sizes, and ceramic materials are only at the beginning of the way to conquer the market. Optical quality is still an important technical difficulty at present for magneto-optical ceramics. Some institutions succeeded in fabricating ceramics with a high in-line transmittance, but the thickness was usually less than 3 mm, which was insufficient to meet the application requirements for many MO ceramics. When researchers try to increase the dimension of ceramics without further adjustment of process parameters, the optical transmittance often decreases significantly in practice, so further studies should pay more attention to the optical quality optimization of the ceramic samples with larger dimensions. Meanwhile, the preparation cost, productivity, and reproducibility of their fabrication processes should also be considered. Fabrication and study of the properties of newly developed MO materials, e.g. $A_2B_2O_7$ ceramics, and implementations of MO ceramics for practical applications in real working conditions are expected. Ceramic synthesis technology also has a convenience of preparing composite structure ceramics, which has been widely studied in laser ceramics [90,273,274]. For MO ceramics, the research on composite structures is just beginning. References [101,170] have calculated the improvement of heat dissipation and thermally-induced depolarization property by optimizing the MO material geometry and composite structure, but there is no report about the experimental measurement of composite MO ceramics so far. In conclusion, MO ceramics have shown their potential for high-performance Faraday isolators, while further study and development of the preparation process and the device design for MO ceramics are still needed.

Table 1 Verdet constant, thermal conductivity, and experimental P_{las} of paramagnetic MO ceramics at ~298 K

Ceramics	Verdet constant (rad·T^{-1}·m^{-1})				Thermal conductivity (W·m^{-1}·K^{-1})	Experimental P_{las}
	532 nm	633 nm	808 nm	1064 nm		
TGG [9]	~210	~140	~80	~38	4.94 [111]	0.74 kW–35 dB at 1070 nm [119]/ 0.8 kW–30 dB at 1070 nm [145]
TAG [176]	~270	~170	~95	~52	6.5 [150]	0.3 kW–38 dB at 1070 nm [163]/ 0.4 kW–33 dB at 1070 nm [174]
DyAG [188]	—	~128	—	—	—	—
HoAG [189]	—	~154	—	~36	10.5 [189]	—
Tb_2O_3 [215]	~741	~470	~261	~143	4.6 [222]	0.09 kW–30 dB at 1070 nm [219]
$(Tb_{0.6}Y_{0.4})_2O_3$ [222]	—	~295	~180	~100	3.4 [222]	—
$(Tb_{0.5}Lu_{0.5})_2O_3$ [223]	—	~224	—	—	5.88 [223]	—
Dy_2O_3 [232]	—	~347	—	—	—	—
$(Dy_{0.7}Y_{0.25}La_{0.95})_2O_3$ [230]	~361	~228	~139	~78	3.0 [236]	—
Ho_2O_3 [245]	~186	~156	~92	~47	—	—
$(Ho_{0.95}La_{0.05})_2O_3$ [244]	—	—	~94	~44	4.8 [236]	—
Er_2O_3 [247]	—	~75	~50	~21	~7.6 [246]	—
$Tb_2Hf_2O_7$ [265]	~250	~155	~85	~50	—	—
$Tb_2Ti_2O_7$ [269]	—	~229	—	—	—	—
$Tb_2Zr_2O_7$ [270]	—	~260	—	~400	—	—
$Ho_2Zr_2O_7$ [271]	—	~157	—	~43	2.3 [271]	—

Acknowledgements

This work was supported by the General Program of Shanghai Natural Science Foundation (Grant No. 22ZR1471500), the International Partnership Program of Chinese Academy of Sciences (Grant No. 121631KYSB20200039), and the International Cooperation Project of Shanghai Science and Technology Commission (Grant No. 20520750200). The IChHPS RAS work was supported by the Russian Science Foundation (Grant No. 18-13-00355).

Declaration of competing interest

The authors have no competing interests to declare that are relevant to the content of this article.

References

[1] Liu GQ, Le ZQ, Shen DF. *Magnetooptics*. Shanghai: Shanghai Scientific and Technical Publishers, 2001. (in Chinese)

[2] Golovina TG, Konstantinova AF, Evdishchenko EA. Magneto-optical effects in various crystalline materials, films, and meso- and nanostructures. *Crystallogr Rep* 2021, **66**: 323–348

[3] Ikesue A, Aung YL. Magneto-optic transparent ceramics. In: *Processing of Ceramics: Breakthroughs in Optical Materials*. Ikesue A, Ed. Hoboken, USA: John Wiley & Sons, 2021: 143–185.

[4] Hossain M, Qin B, Li B, *et al*. Synthesis, characterization, properties and applications of two-dimensional magnetic materials. *Nano Today* 2022, **42**: 101338.

[5] Shi LY, Kumar Srivastava A, Chigrinov VG, *et al*. Kerr effect and Kerr constant enhancement in vertically aligned deformed helix ferroelectric liquid crystals. *Chin Phys B* 2016, **25**: 094212.

[6] Motokawa M. Physics in high magnetic fields. *Rep Prog Phys* 2004, **67**: 1995–2052.

[7] Vinogradov AP, Dorofeenko AV, Merzlikin AM, *et al*. Enhancement of the Faraday and other magneto-optical effects in magnetophotonic crystals. In: *Magnetophotonics: From Theory to Applications*. Inoue M, Levy M, Baryshev AV, Eds. Berlin, Germany: Springer Berlin, Heidelberg, 2013: 1–17.

[8] Maiman TH. Stimulated optical radiation in ruby. *Nature* 1960, **187**: 493–494.

[9] Slezák O, Yasuhara R, Lucianetti A, *et al*. Temperature-wavelength dependence of terbium gallium garnet ceramics Verdet constant. *Opt Mater Express* 2016, **6**: 3683–3691.

[10] Kruk A. Structural and magneto-optical characterization of La,Nd:Y_2O_3 powders obtained via a modified EDTA sol–gel process and HIP-treated ceramics. *Materials* 2020, **13**: 4928.

[11] Kruk A, Mrózek M. The measurement of Faraday effect of translucent material in the entire visible spectrum. *Measurement* 2020, **162**: 107912.

[12] Van Vleck JH, Hebb MH. On the paramagnetic rotation of tysonite. *Phys Rev* 1934, **46**: 17–32.

[13] Borrelli NF. Faraday rotation in glasses. *J Chem Phys* 1964, **41**: 3289–3293.

[14] Khazanov EA, Kulagin OV, Yoshida S, *et al*. Investigation of self-induced depolarization of laser radiation in terbium gallium garnet. *IEEE J Quantum Elect* 1999, **35**: 1116–1122.

[15] Kumari S, Chakraborty S. Study of different magneto-optic materials for current sensing applications. *J Sens Sens Syst* 2018, **7**: 421–431.

[16] Tien PK, Martin RJ, Wolfe R, *et al*. Switching and modulation of light in magneto-optic waveguides of garnet films. *Appl Phys Lett* 1972, **21**: 394–396.

[17] Kriegel I, Scotognella F. Magneto-optical switching in microcavities based on a TGG defect sandwiched between periodic and disordered one-dimensional photonic structures. *Optik* 2017, **142**: 249–255.

[18] Fang XL, Yang QH, Zhang HW. Magneto-optical materials and their applications in magneto-optical switch. *J Magn Mater Devices* 2013, **44**: 68–72. (in Chinese)

[19] Stadler BJH, Mizumoto T. Integrated magneto-optical materials and isolators: A review. *IEEE Photonics J* 2014, **6**: 0600215.

[20] Vojna D, Slezák O, Yasuhara R, *et al*. Faraday rotation of Dy_2O_3, CeF_3 and $Y_3Fe_5O_{12}$ at the mid-infrared wavelengths. *Materials* 2020, **13**: 5324.

[21] Boulnois JL. Photophysical processes in recent medical laser developments: A review. *Laser Med Sci* 1986, **1**: 47–66.

[22] Müller GJ, Berlien P, Scholz C. The medical laser. *Med Laser Appl* 2006, **21**: 99–108.

[23] Shukla A, Vaghasia J, Mistry M. Effect of laser ignition on combustion and performance of internal combustion engine: A review. *Energ Convers Manage X* 2022, **13**: 100166.

[24] Zhang JY, Chen HT, Wang JP, *et al*. Preparation of $(Tb_{1-x}Lu_x)_2O_3$ transparent ceramics by solid solution for magneto-optical application. *J Eur Ceram Soc* 2021, **41**: 2818–2825.

[25] Yavetskiy RP, Balabanov AE, Parkhomenko SV, *et al*. Effect of starting materials and sintering temperature on microstructure and optical properties of Y_2O_3:Yb^{3+} 5 at% transparent ceramics. *J Adv Ceram* 2021, **10**: 49–61.

[26] Palashov OV, Starobor AV, Perevezentsev EA, *et al*. Thermo-optical studies of laser ceramics. *Materials* 2021, **14**: 3944.

[27] Li Q, Wang Y, Wang J, *et al*. High transparency Pr:Y_2O_3 ceramics: A promising gain medium for red emission solid-state lasers. *J Adv Ceram* 2022, **11**: 874–881.

[28] Yang CL, Huang JQ, Huang QF, *et al*. Optical, thermal, and mechanical properties of $(Y_{1-x}Sc_x)_2O_3$ transparent

ceramics. *J Adv Ceram* 2022, **11**: 901–911.
[29] Montross CS, Wei T, Ye L, *et al*. Laser shock processing and its effects on microstructure and properties of metal alloys: A review. *Int J Fatigue* 2002, **24**: 1021–1036.
[30] Abbott BP, Abbott R, Abbott TD, *et al*. Observation of gravitational waves from a binary black hole merger. *Phys Rev Lett* 2016, **116**: 061102.
[31] Park HS, Hurricane OA, Callahan DA, *et al*. High-adiabat high-foot inertial confinement fusion implosion experiments on the national ignition facility. *Phys Rev Lett* 2014, **112**: 055001.
[32] Liu XM, Ge YT. Analysis of development of high energy laser weapon. *Tactical Missile Technol* 2014, **1**: 5–9. (in Chinese)
[33] Ding Y, Jiang F, Zheng RS, *et al*. Overview of high energy laser weapon development in USA (invited). *Electro-Opt Technol Appl* 2021, **36**: 1–9. (in Chinese)
[34] Chen JE, Zhou SM. Review of magneto-optic materials for high power laser isolators (invited). *Infrared Laser Eng* 2020, **49**: 20201072. (in Chinese)
[35] Mironov EA, Palashov OV, Balabanov SS. High-purity CVD-ZnSe polycrystal as a magneto-active medium for a multikilowatt Faraday isolator. *Opt Lett* 2021, **46**: 2119–2122.
[36] Yang ZM, Xu SQ, Jiang ZH, *et al*. Overview of research on magneto-optical glass applied to all-optical fiber sensor. *J Chin Rare Earth Soc* 2003, **21**: 115–122. (in Chinese)
[37] Yin HR, Zhang CX, Liu LY, *et al*. New progress in research on Faraday magneto-optical glass containing rare-earth. *Mater Rev* 2008, **22**: 7–10, 23. (in Chinese)
[38] Elisa M, Stefan RC, Vasiliu IC, *et al*. A new zinc phosphate–tellurite glass for magneto-optical applications. *Nanomaterials* 2020, **10**: 1875.
[39] Li Y, Zhang YX, Chen QL. Surface plasmon resonance effect, nonlinearity and Faraday rotation properties of magneto optical glass: Influence of diamagnetic Ag@ZrO_2 nanoparticles. *J Non-Cryst Solids* 2021, **553**: 120498.
[40] Chen QL, Ma QH, Wang H, *et al*. Diamagnetic tellurite glass and fiber based magneto-optical current transducer. *Appl Opt* 2015, **54**: 8664–8669.
[41] Chen QP, Chen QL, Ferraris M. Effect of ceramic crucibles on magneto-optical PbO–Bi_2O_3–B_2O_3 glasses properties. *New J Glass Ceram* 2012, **2**: 41–50.
[42] Shen Y, Lu YH, Liu Z, *et al*. Performance of magneto-optical glass in optical current transducer application. *J Magn Magn Mater* 2015, **389**: 180–185.
[43] Yin HR, Gao Y, Guo HW, *et al*. Effect of B_2O_3 content and microstructure on Verdet constant of Tb_2O_3-doped GBSG magneto-optical glass. *J Phys Chem C* 2018, **122**: 16894–16900.
[44] Collocott SJ, Taylor KNR. Magneto-optical properties of neodymium-doped soda glass. *J Phys C Solid State Phys* 1980, **13**: 3473–3481.
[45] Babkina A, Kulpina E, Sgibnev Y, *et al*. Terbium concentration effect on magneto-optical properties of ternary phosphate glass. *Opt Mater* 2020, **100**: 109692.
[46] Yang HH, Zhu ZL. Magneto-optical glass mixed with Tb^{3+} ions: High Verdet constant and luminescence properties. *J Lumin* 2021, **231**: 117804.
[47] Tanaka K, Tatehata N, Fujita K, *et al*. The Faraday effect and magneto-optical figure of merit in the visible region for lithium borate glasses containing. *J Phys D Appl Phys* 1998, **31**: 2622–2627.
[48] Petrovskii GT, Edelman IS, Zarubina TV, *et al*. Faraday effect and spectral properties of high-concentrated rare earth oxide glasses in visible and near UV region. *J Non-Cryst Solids* 1991, **130**: 35–40.
[49] Vojna D, Slezák O, Lucianetti A, *et al*. Verdet constant of magneto-active materials developed for high-power Faraday devices. *Appl Sci* 2019, **9**: 3160.
[50] Stevens KT, Schlichting W, Foundos G, *et al*. Promising materials for high power laser isolators: Growth of large single-crystals for Faraday rotator and isolator applications. *Laser Technik J* 2016, **13**: 18–21.
[51] Zhang ZH, Wu Z, Zhang Z, *et al*. Characteristics and recent development of fluoride magneto-optical crystals. *Magnetochemistry* 2023, **9**: 41.
[52] Snetkov IL, Voitovich AV, Palashov OV, *et al*. Review of Faraday isolators for kilowatt average power lasers. *IEEE J Quantum Elect* 2014, **50**: 434–443.
[53] Yoshikawa A, Kagamitani Y, Pawlak DA, *et al*. Czochralski growth of $Tb_3Sc_2Al_3O_{12}$ single crystal for Faraday rotator. *Mater Res Bull* 2002, **37**: 1–10.
[54] Snetkov IL, Yasuhara R, Starobor AV, *et al*. Thermo-optical and magneto-optical characteristics of terbium scandium aluminum garnet crystals. *IEEE J Quantum Elect* 2015, **51**: 7000307.
[55] Starobor AV, Snetkov IL, Yasuhara R, *et al*. Faraday isolators based on TSAG crystal for multikilowatt lasers. In: Proceedings of the 2017 Conference on Lasers and Electro-Optics Europe & European Quantum Electronics Conference, Munich, Germany, 2017: 1.
[56] Weber MJ, Morgret R, Leung SY, *et al*. Magneto-optical properties of KTb_3F_{10} and $LiTbF_4$ crystals. *J Appl Phys* 1978, **49**: 3464–3469.
[57] Vojna D, Duda M, Yasuhara R, *et al*. Verdet constant of potassium terbium fluoride crystal as a function of wavelength and temperature. *Opt Lett* 2020, **45**: 1683–1686.
[58] Zelmon DE, Erdman EC, Stevens KT, *et al*. Optical properties of lithium terbium fluoride and implications for performance in high power lasers. *Appl Opt* 2016, **55**: 834–837.
[59] Duan MQ, Xu Y. A theoretical investigation on the magneto-optical effect of CeF_3 and NdF_3. *J Magn Magn Mater* 1992, **115**: 1–8.
[60] Zhao G, Zhao CC, Yang YL, *et al*. Magneto-optical performances of novel neodymium-doped CeF_3 crystal. *Mater Lett* 2021, **300**: 130134.
[61] Starobor A, Mironov E, Snetkov I, *et al*. Cryogenically cooled CeF_3 crystal as media for high-power magneto-optical devices. *Opt Lett* 2017, **42**: 1864–1866.

[62] Jiang GC, Zhang ZH, Li HF, *et al*. TGT growth and magneto-optical properties of PrF_3 crystal. *Physica B* 2021, **614**: 413031.
[63] Slack GA, Oliver DW. Thermal conductivity of garnets and phonon scattering by rare-earth ions. *Phys Rev B* 1971, **4**: 592–609.
[64] Chen X, Calemczuk R, Salce B, *et al*. Long-transient conoscopic pattern technique. *Solid State Commun* 1999, **110**: 431–434.
[65] Ganschow S, Klimm D, Reiche P, *et al*. On the crystallization of terbium aluminium garnet. *Cryst Res Technol* 1999, **34**: 615–619.
[66] Geho M, Sekijima T, Fujii T. Growth of terbium aluminum garnet ($Tb_3Al_5O_{12}$; TAG) single crystals by the hybrid laser floating zone machine. *J Cryst Growth* 2004, **267**: 188–193.
[67] Shimamura K, Kito T, Castel E, *et al*. Growth of $\{Tb_3\}[Sc_{2-x}Lu_x](Al_3)O_{12}$ single crystals for visible- infrared optical isolators. *Cryst Growth Des* 2010, **10**: 3466–3470.
[68] Sekijima T, Satoh H, Tahara K, *et al*. Growth of fibrous YIG single crystals by the self-adjusting solvent FZ method. *J Cryst Growth* 1998, **193**: 446–450.
[69] Liu HP, Zhan GX, Wu GH, *et al*. Improved edge-defined film-fed growth of incongruent-melting $Tb_3Al_5O_{12}$ crystal with high magneto-optical and thermal performances. *Cryst Growth Des* 2019, **19**: 1525–1531.
[70] Prabhakaran D, Boothroyd AT. Crystal growth of spin-ice pyrochlores by the floating-zone method. *J Cryst Growth* 2011, **318**: 1053–1056.
[71] Li QJ, Xu LM, Fan C, *et al*. Single crystal growth of the pyrochlores $R_2Ti_2O_7$ (R = rare earth) by the optical floating-zone method. *J Cryst Growth* 2013, **377**: 96–100.
[72] Klimm D, Guguschev C, Kok DJ, *et al*. Crystal growth and characterization of the pyrochlore $Tb_2Ti_2O_7$. *CrystEngComm* 2017, **19**: 3908–3914.
[73] Dou RQ, Zhang HT, Zhang QL, *et al*. Growth and properties of TSAG and TSLAG magneto-optical crystals with large size. *Opt Mater* 2019, **96**: 109272.
[74] Veber P, Velázquez M, Gadret G, *et al*. Flux growth at 1230 ℃ of cubic Tb_2O_3 single crystals and characterization of their optical and magnetic properties. *CrystEngComm* 2015, **17**: 492–497.
[75] Carothers KJ, Norwood RA, Pyun J. High Verdet constant materials for magneto-optical Faraday rotation: A review. *Chem Mater* 2022, **34**: 2531–2544.
[76] Vandendriessche S, Van Cleuvenbergen S, Willot P, *et al*. Giant Faraday rotation in mesogenic organic molecules. *Chem Mater* 2013, **25**: 1139–1143.
[77] Vleugels R, Steverlynck J, Brullot W, *et al*. Faraday rotation in discotic liquid crystals by long-range electron movement. *J Phys Chem C* 2019, **123**: 9382–9387.
[78] Nelson Z, Delage-Laurin L, Peeks MD, *et al*. Large Faraday rotation in optical-quality phthalocyanine and porphyrin thin films. *J Am Chem Soc* 2021, **143**: 7096–7103.
[79] Koeckelberghs G, Vangheluwe M, van Doorsselaere K, *et al*. Regioregularity in poly(3-alkoxythiophene)s: Effects on the Faraday rotation and polymerization mechanism. *Macromol Rapid Commun* 2006, **27**: 1920–1925.
[80] Araoka F, Abe M, Yamamoto T, *et al*. Large Faraday rotation in a π-conjugated poly(arylene ethynylene) thin film. *Appl Phys Express* 2009, **2**: 011501.
[81] Wang P, Lin SB, Lin Z, *et al*. A semiconducting conjugated radical polymer: Ambipolar redox activity and Faraday effect. *J Am Chem Soc* 2018, **140**: 10881–10889.
[82] Delage-Laurin L, Nelson Z, Swager TM. C-term Faraday rotation in metallocene containing thin films. *ACS Appl Mater Interfaces* 2021, **13**: 25137–25142.
[83] Martinez L, Cecelja F, Rakowski R. A novel magneto-optic ferrofluid material for sensor applications. *Sensor Actuat A-Phys* 2005, **123–124**: 438–443.
[84] Miles A, Gai Y, Gangopadhyay P, *et al*. Improving Faraday rotation performance with block copolymer and FePt nanoparticle magneto-optical composite. *Opt Mater Express* 2017, **7**: 2126–2140.
[85] Pavlopoulos NG, Kang KS, Holmen LN, *et al*. Polymer and magnetic nanoparticle composites with tunable magneto-optical activity: Role of nanoparticle dispersion for high Verdet constant materials. *J Mater Chem C* 2020, **8**: 5417–5425.
[86] Carothers KJ, Lyons NP, Pavlopoulos NG, *et al*. Polymer-coated magnetic nanoparticles as ultrahigh Verdet constant materials: Correlation of nanoparticle size with magnetic and magneto-optical properties. *Chem Mater* 2021, **33**: 5010–5020.
[87] Dai JW, Li J. Promising magneto-optical ceramics for high power Faraday isolators. *Scripta Mater* 2018, **155**: 78–84.
[88] Li J, Dai JW, Pan YB. Research progress on magneto-optical transparent ceramics. *J Inorg Mater* 2018, **33**: 1–8. (in Chinese)
[89] Ming WY, Jiang ZW, Luo GF, *et al*. Progress in transparent nano-ceramics and their potential applications. *Nanomaterials* 2022, **12**: 1491.
[90] Tian F, Ikesue A, Li J. Progress and perspectives on composite laser ceramics: A review. *J Eur Ceram Soc* 2022, **42**: 1833–1851.
[91] Li J, Tian F, Liu ZY. Research progress and prospect of mid-infrared laser ceramics. *J Synth Cryst* 2020, **49**: 1467–1487. (in Chinese)
[92] Snetkov I, Li J. Selection of magneto-optical material for a Faraday isolator operating in high-power laser radiation. *Magnetochemistry* 2022, **8**: 168.
[93] Ikesue A, Aung YL, Wang J. Progress of magneto-optical ceramics. *Prog Quantum Electron* 2022, **86**: 100416.
[94] Huang ZY, Shi Y, Zhang YT, *et al*. An effective strategy for preparing transparent ceramics using nanorod powders based on pressure-assisted particle fracture and rearrangement. *J Adv Ceram* 2022, **11**: 1976–1987.

[95] Permin DA, Boldin MS, Belyaev AV, *et al*. IR-transparent $MgO–Gd_2O_3$ composite ceramics produced by self-propagating high-temperature synthesis and spark plasma sintering. *J Adv Ceram* 2021, **10**: 237–246.
[96] Liu X, Qian XL, Zheng P, *et al*. Composition and structure design of three-layered composite phosphors for high color rendering chip-on-board light-emitting diode devices. *J Adv Ceram* 2021, **10**: 729–740.
[97] Zhou TY, Hou C, Zhang L, *et al*. Efficient spectral regulation in $Ce:Lu_3(Al,Cr)_5O_{12}$ and $Ce:Lu_3(Al,Cr)_5O_{12}$/$Ce:Y_3Al_5O_{12}$ transparent ceramics with high color rendering index for high-power white LEDs/LDs. *J Adv Ceram* 2021, **10**: 1107–1118.
[98] Zhu DY, Nikl M, Chewpraditkul W, *et al*. Development and prospects of garnet ceramic scintillators: A review. *J Adv Ceram* 2022, **11**: 1825–1848.
[99] Kruk A, Madej D. Structural properties and Faraday effect of arc melted magnesia transparent polycrystal. *Opt Mater* 2020, **108**: 110245.
[100] Guerrero H, Escudero JL, Bernabeu E. Polycrystalline materials for magneto-optical devices. *Opt Lett* 1992, **17**: 760–762.
[101] Khazanov EA. Thermooptics of magnetoactive media: Faraday isolators for high average power lasers. *Physics-Uspekhi* 2016, **59**: 886–909.
[102] Trénec G, Volondat W, Cugat O, *et al*. Permanent magnets for Faraday rotators inspired by the design of the magic sphere. *Appl Opt* 2011, **50**: 4788–4797.
[103] Kagan MA, Khazanov EA. Thermally induced birefringence in Faraday devices made from terbium gallium garnet-polycrystalline ceramics. *Appl Opt* 2004, **43**: 6030–6039.
[104] Starobor A, Zheleznov D, Palashov O, *et al*. Study of the properties and prospects of Ce:TAG and TGG magnetooptical ceramics for optical isolators for lasers with high average power. *Opt Mater Express* 2014, **4**: 2127–2132.
[105] Snetkov IL. Features of thermally induced depolarization in magneto-active media with negative optical anisotropy parameter. *IEEE J Quantum Elect* 2018, **54**: 1–8.
[106] Snetkov I, Yakovlev A, Starobor A, *et al*. Thermo-optical properties of terbium sesquioxide (Tb_2O_3) ceramics at room temperature. *Opt Lett* 2021, **46**: 3592–3595.
[107] Villaverde AB, Donatti DA, Bozinis DG. Terbium gallium garnet Verdet constant measurements with pulsed magnetic field. *J Phys C Solid State Phys* 1978, **11**: L495–L498.
[108] Mironov EA, Zheleznov DS, Starobor AV, *et al*. Large-aperture Faraday isolator based on a terbium gallium garnet crystal. *Opt Lett* 2015, **40**: 2794–2797.
[109] Long Y, Shi ZB, Ding YC *et al*. Growth and characterization of large-size terbium gallium garnet single crystal. *Piezoelectrics & Acoustooptics* 2016, **38**: 433–436.
[110] Khazanov EA. Investigation of Faraday isolator and Faraday mirror designs for multi-kilowatt power lasers. In: Proceedings of the High-Power Lasers and Applications, San Jose, USA, 2003: 115–126.
[111] Yasuhara R, Tokita S, Kawanaka J, *et al*. Cryogenic temperature characteristics of Verdet constant on terbium gallium garnet ceramics. *Opt Express* 2007, **15**: 11255–11261.
[112] Yoshida H, Tsubakimoto K, Fujimoto Y, *et al*. Optical properties and Faraday effect of ceramic terbium gallium garnet for a room temperature Faraday rotator. *Opt Express* 2011, **19**: 15181–15187.
[113] Yasuhara R, Furuse H. Thermally induced depolarization in TGG ceramics. *Opt Lett* 2013, **38**: 1751–1753.
[114] Yasuhara R, Nozawa H, Yanagitani T, *et al*. Temperature dependence of thermo-optic effects of single-crystal and ceramic TGG. *Opt Express* 2013, **21**: 31443–31452.
[115] Yasuhara R, Snetkov I, Starobor A, *et al*. Terbium gallium garnet ceramic Faraday rotator for high-power laser application. *Opt Lett* 2014, **39**: 1145–1148.
[116] Snetkov I, Mukhin I, Palashov O, *et al*. Compensation of thermally induced depolarization in Faraday isolators for high average power lasers. *Opt Express* 2011, **19**: 6366–6376.
[117] Snetkov IL, Yasuhara R, Starobor AV, *et al*. TGG ceramics based Faraday isolator with external compensation of thermally induced depolarization. *Opt Express* 2014, **22**: 4144–4151.
[118] Snetkov IL, Palashov OV. Compensation of thermal effects in Faraday isolator for high average power lasers. *Appl Phys B* 2012, **109**: 239–247.
[119] Yasuhara R, Snetkov I, Starobor A, *et al*. Terbium gallium garnet ceramic-based Faraday isolator with compensation of thermally induced depolarization for high-energy pulsed lasers with kilowatt average power. *Appl Phys Lett* 2014, **105**: 241104.
[120] Feng Y, Lin H, Chen C, *et al*. Fabrication of transparent $Tb_3Ga_5O_{12}$ ceramic. *Chin Opt Lett* 2015, **13**: 031602.
[121] Liu ZY, Ikesue A, Li J. Research progress and prospects of rare-earth doped sesquioxide laser ceramics. *J Eur Ceram Soc* 2021, **41**: 3895–3910.
[122] Liu ZY, Toci G, Pirri A, *et al*. Fabrication and optical property of $Nd:Lu_2O_3$ transparent ceramics for solid-state laser applications. *J Inorg Mater* 2021, **36**: 210–216.
[123] Huang XY, Liu YM, Liu Y, *et al*. Fabrication and characterizations of Yb:YAG transparent ceramics using alcohol–water co-precipitation method. *J Inorg Mater* 2021, **36**: 217–224.
[124] Chen PH, Liu Q, Li XY, *et al*. Influence of terminal pH value on co-precipitated nanopowders for yttria-stabilized ZrO_2 transparent ceramics. *Opt Mater* 2019, **98**: 109475.
[125] Liu Q, Chen PH, Jiang N, *et al*. Fabrication and characterizations of 8.7 mol% $Y_2O_3–ZrO_2$ transparent ceramics using co-precipitated nanopowders. *Scripta Mater* 2019, **171**: 98–101.
[126] Liu ZY, Toci G, Pirri A, *et al*. Fabrication,

microstructures, and optical properties of Yb:Lu_2O_3 laser ceramics from co-precipitated nano-powders. *J Adv Ceram* 2020, **9**: 674–682.

[127] Wei JB, Toci G, Pirri A, *et al*. Fabrication and property of Yb:CaF_2 laser ceramics from co-precipitated nanopowders. *J Inorg Mater* 2019, **34**: 1341–1348.

[128] Jing YQ, Liu Q, Su S, *et al*. Fabrication of highly transparent Co:$MgAl_2O_4$ ceramic saturable absorber for passive *Q*-switching at 1.5 μm. *J Inorg Mater* 2021: 877–882.

[129] Liu Q, Wu LF, Li XY, *et al*. Fabrication and characterization of Dy,Tb:LuAG transparent ceramics for yellow lasers. *Chin J Lumin* 2022, **43**: 1733–1740.

[130] Liu ZY, Toci G, Pirri A, *et al*. Fabrication and characterizations of Tm:Lu_2O_3 transparent ceramics for 2 μm laser applications. *Opt Mater* 2022, **131**: 112705.

[131] Chen PH, Li XY, Tian F, *et al*. Fabrication, microstructure, and properties of 8 mol% yttria-stabilized zirconia (8YSZ) transparent ceramics. *J Adv Ceram* 2022, **11**: 1153–1162.

[132] Liu ZY, Wei JB, Toci G, *et al*. Microstructure and laser emission of Yb:CaF_2 transparent ceramics fabricated by air pre-sintering and hot isostatic pressing. *Opt Mater* 2022, **129**: 112540.

[133] Li XY, Liu Q, Jiang N, *et al*. Fabrication and characterizations of highly transparent $Tb_3Ga_5O_{12}$ magneto-optical ceramics. *Opt Mater* 2019, **88**: 238–243.

[134] Li XY, Liu Q, Hu ZW, *et al*. Influence of ammonium hydrogen carbonate to metal ions molar ratio on co-precipitated nanopowders for TGG transparent ceramics. *J Inorg Mater* 2019, **34**: 791–796.

[135] Li XY, Liu Q, Pan HM, *et al*. Transparent $Tb_3Ga_5O_{12}$ magneto-optical ceramics sintered from co-precipitated nano-powders calcined at different temperatures. *Opt Mater* 2019, **90**: 26–32.

[136] Zhang XJ, Liu HS, Zhu HG, *et al*. Preparation and thermal and optical properties of terbium gallium garnet ceramics. *J Chin Ceram Soc* 2018, **46**: 910–914.

[137] Jin WZ, Gai LY, Chen J, *et al*. Fabrication and magneto-optical properties of TGG transparent ceramics. *Physica B* 2019, **555**: 96–98.

[138] Chen Z, Yang L, Hang Y, *et al*. Faraday effect improvement by Dy^{3+}-doping of terbium gallium garnet single crystal. *J Solid State Chem* 2016, **233**: 277–281.

[139] Chen Z, Yang L, Hang Y, *et al*. Improving characteristic of Faraday effect based on the Tm^{3+} doped terbium gallium garnet single crystal. *J Alloys Compd* 2016, **661**: 62–65.

[140] Chen Z, Yang L, Wang XY, *et al*. Wavelength dependence of Verdet constant of Pr doped terbium gallium garnet crystal. *Opt Mater* 2016, **62**: 475–478.

[141] Chen Z, Yang L, Hang Y, *et al*. Growth and magneto-optical characteristics of cerium-doped terbium gallium garnet by the floating zone method. *Cryst Res Technol* 2015, **50**: 528–531.

[142] Chen Z, Yang L, Wang XY, *et al*. High magneto-optical characteristics of holmium-doped terbium gallium garnet crystal. *Opt Lett* 2016, **41**: 2580–2583.

[143] Wang XY, Yang L, Chen Z, *et al*. Growth and Faraday rotation characteristics of $Tb_{3-x}Nd_xGa_5O_{12}$ single crystal. *Opt Mater* 2015, **47**: 157–160.

[144] Li XY, Liu Q, Liu X, *et al*. Novel $(Tb_{0.99}Ce_{0.01})_3Ga_5O_{12}$ magneto-optical ceramics for Faraday isolators. *Scripta Mater* 2020, **177**: 137–140.

[145] Li XY, Snetkov IL, Yakovlev A, *et al*. Fabrication and performance evaluation of novel transparent ceramics RE:$Tb_3Ga_5O_{12}$ (RE = Pr, Tm, Dy) toward magneto-optical application. *J Adv Ceram* 2021, **10**: 271–278.

[146] Chen C, Zhou SM, Lin H, *et al*. Fabrication and performance optimization of the magneto-optical $(Tb_{1-x}R_x)_3Al_5O_{12}$ (R = Y, Ce) transparent ceramics. *Appl Phys Lett* 2012, **101**: 131908.

[147] Ganschow S, Klimm D, Epelbaum BM, *et al*. Growth conditions and composition of terbium aluminum garnet single crystals grown by the micro pulling down technique. *J Cryst Growth* 2001, **225**: 454–457.

[148] Geho M, Sekijima T, Fujii T. Growth mechanism of incongruently melting terbium aluminum garnet ($Tb_3Al_5O_{12}$; TAG) single crystals by laser FZ method. *J Cryst Growth* 2005, **275**: e663–e667.

[149] Ikesue A, Aung YL. (Invited) magneto-optical performance of $(LuTb)_3Al_5O_{12}$ single crystal by SSCG method. *Opt Mater X* 2022, **13**: 100139.

[150] Lin H, Zhou SM, Teng H. Synthesis of $Tb_3Al_5O_{12}$ (TAG) transparent ceramics for potential magneto-optical applications. *Opt Mater* 2011, **33**: 1833–1836.

[151] Chen C, Yi XZ, Zhang S, *et al*. Vacuum sintering of $Tb_3Al_5O_{12}$ transparent ceramics with combined TEOS+MgO sintering aids. *Ceram Int* 2015, **41**: 12823–12827.

[152] Hao DM, Shao XC, Tang YR, *et al*. Effect of Si^{4+} doping on the microstructure and magneto-optical properties of TAG transparent ceramics. *Opt Mater* 2018, **77**: 253–257.

[153] Zhang SY, Liu P, Xu XD, *et al*. Effect of the MgO on microstructure and optical properties of TAG ($Tb_3Al_5O_{12}$) transparent ceramics using hot isostatic pressing. *Opt Mater* 2018, **80**: 7–11.

[154] Chen C, Li XL, Feng Y, *et al*. Optimization of CeO_2 as sintering aid for $Tb_3Al_5O_{12}$ Faraday magneto-optical transparent ceramics. *J Mater Sci* 2015, **50**: 2517–2521.

[155] Chen J, Lin H, Hao DM, *et al*. Exaggerated grain growth caused by ZrO_2-doping and its effect on the optical properties of $Tb_3Al_5O_{12}$ ceramics. *Scripta Mater* 2019, **162**: 82–85.

[156] Chen J, Tang YR, Chen C, *et al*. Roles of zirconia-doping in the sintering process of high quality $Tb_3Al_5O_{12}$ magneto-optic ceramics. *Scripta Mater* 2020, **176**: 83–87.

[157] Furuse H, Yasuhara R, Hiraga K, *et al*. High Verdet constant of Ti-doped terbium aluminum garnet (TAG) ceramics. *Opt Mater Express* 2016, **6**: 191–196.

[158] Hao DM, Chen J, Ao G, *et al*. Effect of Tb_4O_7 excess on the microstructure and magneto-optical properties of TAG transparent ceramic. *Opt Mater* 2019, **94**: 47–52.
[159] Duan PP, Liu P, Xu XD, *et al*. Fabrication of transparent $Tb_3Al_5O_{12}$ ceramics by hot isostatic pressing sintering. *J Am Ceram Soc* 2017, **100**: 2893–2900.
[160] Huang XY, Zuo L, Li XY, *et al*. Fabrication and characterization of $Tb_3Al_5O_{12}$ magneto-optical ceramics by solid-state reactive sintering. *Opt Mater* 2020, **102**: 109795.
[161] Dai JW, Snetkov IL, Palashov OV, *et al*. Fabrication, microstructure and magneto-optical properties of $Tb_3Al_5O_{12}$ transparent ceramics. *Opt Mater* 2016, **62**: 205–210.
[162] Dai JW, Pan YB, Chen HH, *et al*. Synthesis of Tb_4O_7 nanopowders by the carbonate-precipitation method for $Tb_3Al_5O_{12}$ magneto-optical ceramics. *Opt Mater* 2017, **73**: 706–711.
[163] Zheleznov D, Starobor A, Palashov O, *et al*. High-power Faraday isolators based on TAG ceramics. *Opt Express* 2014, **22**: 2578–2583.
[164] Dai JW, Pan YB, Chen HH, *et al*. Fabrication of $Tb_3Al_5O_{12}$ transparent ceramics using co-precipitated nanopowders: The influence of ammonium hydrogen carbonate to metal ions molar ratio. *Ceram Int* 2017, **43**: 14457–14463.
[165] Dai JW, Pan YB, Wang W, *et al*. Fabrication of $Tb_3Al_5O_{12}$ transparent ceramics using co-precipitated nanopowders. *Opt Mater* 2017, **73**: 38–44.
[166] Dai JW, Pan YB, Xie TF, *et al*. Highly transparent $Tb_3Al_5O_{12}$ magneto-optical ceramics sintered from co-precipitated powders with sintering aids. *Opt Mater* 2018, **78**: 370–374.
[167] Li XY, Zhang LX, Hu DJ, *et al*. Fabrication and characterizations of $Tb_3Al_5O_{12}$-based magneto-optical ceramics. *Int J Appl Ceram Technol* 2023, **20**: 493–499.
[168] Li XY, Liu QA, Liu X, *et al*. Sintering parameter optimization of $Tb_3Al_5O_{12}$ magneto-optical ceramics by vacuum sintering and HIP post-treatment. *J Am Ceram Soc* 2021, **104**: 2116–2124.
[169] Aung YL, Ikesue A. Development of optical grade $(Tb_xY_{1-x})_3Al_5O_{12}$ ceramics as Faraday rotator material. *J Am Ceram Soc* 2017, **100**: 4081–4087.
[170] Hamamoto K, Nishio M, Tokita S, *et al*. Properties of TAG ceramics at room and cryogenic temperatures and performance estimations as a Faraday isolator. *Opt Mater Express* 2021, **11**: 434–441.
[171] Duan PP, Liu P, Xu XD, *et al*. Fabrication and properties of $(Tb_xY_{1-x})_3Al_5O_{12}$ transparent ceramics by hot isostatic pressing. *Opt Mater* 2017, **72**: 58–62.
[172] Ikesue A, Kamata K. Role of Si on Nd solid-solution of YAG ceramics. *J Ceram Soc Jpn* 1995, **103**: 489–493.
[173] Maître A, Sallé C, Boulesteix R, *et al*. Effect of silica on the reactive sintering of polycrystalline Nd:YAG ceramics. *J Am Ceram Soc* 2008, **91**: 406–413.
[174] Starobor A, Palashov O, Zhou SM. Thermo-optical properties of terbium–aluminum garnet ceramics doped with silicon and titanium. *Opt Lett* 2016, **41**: 1510–1513.
[175] Starobor A, Palashov O. The temperature dependence of thermooptical properties of magnetooptical TAG ceramics doped with silicon and titanium. *Opt Mater* 2018, **78**: 15–20.
[176] Yakovlev AI, Snetkov IL, Palashov OV, *et al*. Magneto-optical and thermo-optical properties of Ce, Pr, and Ho doped TAG ceramics. *IEEE J Quantum Elect* 2019, **55**: 7000108.
[177] Liu Q, Li XY, Dai JW, *et al*. Fabrication and characterizations of $(Tb_{1-x}Pr_x)_3Al_5O_{12}$ magneto-optical ceramics for Faraday isolators. *Opt Mater* 2018, **84**: 330–334.
[178] Dai JW, Pan YB, Li XY, *et al*. Fabrication and properties of $(Tb_{1-x}Ce_x)_3Al_5O_{12}$ magneto-optical ceramics with different doping concentrations. *Scripta Mater* 2018, **155**: 46–49.
[179] Dai JW, Pan YB, Xie TF, *et al*. A novel $(Tb_{0.995}Ho_{0.005})_3Al_5O_{12}$ magneto-optical ceramic with high transparency and Verdet constant. *Scripta Mater* 2018, **150**: 160–163.
[180] Xin XH, Hao YK, Liu L, *et al*. $Tb_3Al_3Ga_2O_{12}$: A novel visible–infrared Faraday crystal exhibiting a superior magneto-optical performance. *Cryst Growth Des* 2022, **22**: 5535–5541.
[181] Chen C, Ni Y, Zhou SM, *et al*. Preparation of $(Tb_{0.8}Y_{0.2})_3Al_5O_{12}$ transparent ceramic as novel magneto-optical isolator material. *Chin Opt Lett* 2013, **11**: 021601.
[182] Wu YH, Sun ZC, Feng GQ, *et al*. Preparation and properties of novel $Tb_3Sc_2Al_3O_{12}$ (TSAG) magneto-optical transparent ceramic. *J Eur Ceram Soc* 2021, **41**: 195–201.
[183] Tanaka K, Ikari M. Paramagnetic garnet type transparent ceramics, magneto optical material and magneto optic device. JP2019202916A. Available at https://www.j-platpat.inpit.go.jp/c1800/PU/JP-2019-202916/DB4A53-548B46CD8FFD8A8F43AE3D49C14D8EDC32D45A-47F34B312C74EF62202E/11/ja.
[184] Masanori I. Paramagnetic garnet type transparent ceramics, magneto optical material and magneto optic device. JP2019199386A. Available at https://www.j-platpat.inpit.go.jp/c1800/PU/JP-2019-199386/9F64255CD6992-22E68C63B70FFC8BA8E45F09716C5EC114C9AC01-ADC380B5E1D/11/ja.
[185] Masanori I. Paramagnetic garnet type transparent ceramics, magneto optical materials and magneto optic devices. JP2019199387A. Available at https://www. j-platpat.inpit.go.jp/c1800/PU/JP-2019-199387/37BDEAEE7B070D2F-807010DA690680F8D1E5C52B0D9ADCEDD3DD107F-B5CC202B/11/ja.
[186] Hao DM, Feng YE, Tang YR, *et al*. $Tb_3Al_{2.5}Ga_{2.5}O_{12}$ transparent ceramic for magneto-optical application. *Int J Appl Ceram Technol* 2017, **14**: 399–403.
[187] Li R, Numazawa T, Hashimoto T, *et al*. Magnetic and

thermal properties of $Dy_3Al_5O_{12}$ as a magnetic refrigerant. In: *Advances in Cryogenic Engineering Materials*. Reed RP, Clark AF, Eds. New York, USA: Springer New York, 1986: 287–294.

[188] Hu S, Qin XP, Lu CH, *et al*. Fabrication of transparent dysprosium aluminum garnet ($Dy_3Al_5O_{12}$) ceramics via a solid-state reaction method. *J Am Ceram Soc* 2015, **98**: 1714–1716.

[189] Wang MY, Lu B. Manufacture and Faraday magneto-optical effect of highly transparent novel holmium aluminum garnet ceramics. *Scripta Mater* 2021, **195**: 113729.

[190] Blankenship AC, Huntt RL. Microwave characteristics of fine-grain high-power garnets and spinels. *J Appl Phys* 1966, **37**: 1066–1068.

[191] Paladino AE, Maguire EA. Microstructure development in yttrium iron garnet. *J Am Ceram Soc* 1970, **53**: 98–102.

[192] Akhtar MN, Bakar Sulong A, Khan MA, *et al*. Structural and magnetic properties of yttrium iron garnet (YIG) and yttrium aluminum iron garnet (YAIG) nanoferrites prepared by microemulsion method. *J Magn Magn Mater* 2016, **401**: 425–431.

[193] Durčok S, Pollert E, Šimša Z, *et al*. Growth of YIG and BiGdIG single crystals for magnetooptical applications. *Mater Chem Phys* 1996, **45**: 124–129.

[194] Kamada O, Nakaya T, Higuchi S. Magnetic field optical sensors using Ce:YIG single crystals as a Faraday element. *Sensor Actuat A-Phys* 2005, **119**: 345–348.

[195] Van Hook HJ. Phase relations in the ternary system Fe_2O_3–FeO–$YFeO_3$. *J Am Ceram Soc* 1962, **45**: 162–165.

[196] Zhao WZ. Magneto-optic properties and sensing performance of garnet YbBi:YIG. *Sensor Actuat A-Phys* 2001, **89**: 250–254.

[197] Zhuang NF, Chen WB, Shi LJ, *et al*. A new technique to grow incongruent melting Ga:YIG crystals: The edge-defined film-fed growth method. *J Appl Crystallogr* 2013, **46**: 746–751.

[198] Thiery N, Naletov VV, Vila L, *et al*. Electrical properties of epitaxial yttrium iron garnet ultrathin films at high temperatures. *Phys Rev B* 2018, **97**: 064422.

[199] Dubs C, Surzhenko O, Linke R, *et al*. Sub-micrometer yttrium iron garnet LPE films with low ferromagnetic resonance losses. *J Phys D Appl Phys* 2017, **50**: 204005.

[200] Yang YM, Li XY, Liu ZY, *et al*. Pressureless sintering of YIG ceramics from coprecipitated nanopowders. *Magnetochemistry* 2021, **7**: 56.

[201] Ikesue A, Aung YL. Development of optical grade polycrystalline YIG ceramics for Faraday rotator. *J Am Ceram Soc* 2018, **101**: 5120–5126.

[202] Ikesue A, Aung YL. Synthesis of transparent YIG ceramics by pressureless sintering. *J Eur Ceram Soc* 2022, **42**: 6762–6765.

[203] Chung KH, Takahashi K, Takagi H, *et al*. Magnetic and magneto-optic properties of Bi:YIG film for a magneto-optic spatial light modulator. *J Ceram Process Res* 2007, **8**: 187–190.

[204] Berzhansky V, Mikhailova T, Shaposhnikov A, *et al*. Magneto-optics of nanoscale Bi:YIG films. *Appl Opt* 2013, **52**: 6599–6606.

[205] Aung YL, Ikesue A, Watanabe T, *et al*. Bi substituted YIG ceramics isolator for optical communication. *J Alloys Compd* 2019, **811**: 152059.

[206] Zou S, He XY, Zeng X, *et al*. Microstructure and properties of Bi-doped yttrium iron garnet magneto-optical ceramics prepared by hot-pressing sintering process. *J Inorg Mater* 2022, **37**: 773–779. (in Chinese)

[207] Huang M, Zhang SY. Growth and characterization of cerium-substituted yttrium iron garnet single crystals for magneto-optical applications. *Appl Phys A* 2002, **74**: 177–180.

[208] Higuchi S, Furukawa Y, Takekawa S, *et al*. Magnetooptical properties of cerium-substituted yttrium iron garnet single crystals for magnetic-field sensor. *Sensor Actuat A-Phys* 2003, **105**: 293–296.

[209] Onbasli MC, Beran L, Zahradník M, *et al*. Optical and magneto-optical behavior of cerium yttrium iron garnet thin films at wavelengths of 200–1770 nm. *Sci Rep* 2016, **6**: 23640.

[210] Ikesue A, Aung YL, Yasuhara R, *et al*. Giant Faraday rotation in heavily ce-doped YIG bulk ceramics. *J Eur Ceram Soc* 2020, **40**: 6073–6078.

[211] Tao JW, Zou S, He DH, *et al*. Fabrication and characteristics of Ce-doped $Y_3Fe_5O_{12}$ ceramics by hot-press sintering with oxygen/nitrogen atmosphere. *J Am Ceram Soc* 2023, **106**: 381–388.

[212] Aung YL, Ikesue A. Transparent $Tb_3Fe_5O_{12}$ ceramics as mid-IR isolator. *J Alloys Compd* 2019, **773**: 739–742.

[213] Makikawa S, Yahagi A, Ikesue A. Transparent ceramic, method for manufacturing same, and magneto-optical device. U.S. Patent 9 470 915, Oct. 2016.

[214] Snetkov IL, Permin DA, Balabanov SS, *et al*. Wavelength dependence of Verdet constant of Tb^{3+}:Y_2O_3 ceramics. *Appl Phys Lett* 2016, **108**: 161905.

[215] Snetkov IL, Palashov OV. Cryogenic temperature characteristics of Verdet constant of terbium sesquioxide ceramics. *Opt Mater* 2016, **62**: 697–700.

[216] Balabanov SS, Permin DA, Rostokina EY, *et al*. Synthesis and structural characterization of ultrafine terbium oxide powders. *Ceram Int* 2017, **43**: 16569–16574.

[217] Balabanov SS, Permin DA, Rostokina EY, *et al*. Sinterability of nanopowders of terbia solid solutions with scandia, yttria, and lutetia. *J Adv Ceram* 2018, **7**: 362–369.

[218] Balabanov SS, Permin DA, Rostokina EY, *et al*. Characterizations of REE:Tb_2O_3 magneto-optical ceramics. *Phys Status Solidi B* 2020, **257**: 1900474.

[219] Snetkov I, Starobor A, Palashov O, *et al*. Thermally

induced effects in a Faraday isolator on terbium sesquioxide (Tb_2O_3) ceramics. *Opt Mater* 2021, **120**: 111466.

[220] Yakovlev A, Snetkov I, Palashov O. Thermo-optical properties of cryogenically cooled $(Tb_{0.9}Y_{0.1})_2O_3$ ceramics. *Opt Commun* 2022, **504**: 127508.

[221] Ikesue A, Aung YL, Makikawa S, *et al*. Polycrystalline $(Tb_XY_{1-X})_2O_3$ Faraday rotator. *Opt Lett* 2017, **42**: 4399–4401.

[222] Ikesue A, Aung YL, Makikawa S, *et al*. Total performance of magneto-optical ceramics with a bixbyite structure. *Materials* 2019, **12**: 421.

[223] Zhang JY, Chen HT, Wang JP, *et al*. Phase transformation process of Tb_2O_3 at elevated temperature. *Scripta Mater* 2019, **171**: 108–111.

[224] Xin Y, Xu T, Wang YZ, *et al*. Effect of ZrO_2 content on microstructure evolution and sintering properties of $(Tb_{0.7}Lu_{0.3})_2O_3$ magneto-optic transparent ceramics. *Magnetochemistry* 2022, **8**: 175.

[225] Yang MQ, Zhou D, Xu JY, *et al*. Fabrication and magneto-optical property of yttria stabilized Tb_2O_3 transparent ceramics. *J Eur Ceram Soc* 2019, **39**: 5005–5009.

[226] Qi HB, Zhou D, Li XH, *et al*. Fabrication of 4 at.% La^{3+} ion doped $(Tb_xLu_{0.96-x})_2O_3$ transparent ceramics by using NC–PLSH technology and characterisation of their magneto-optical properties. *J Eur Ceram Soc* 2023, **43**: 1156–1160.

[227] Hu DJ, Li XY, Zhang LX, *et al*. Terbium (III) oxide (Tb_2O_3) transparent ceramics by two-step sintering from precipitated powder. *Magnetochemistry* 2022, **8**: 73.

[228] Hideki Y, Takagimi Y. Translucent rare earth oxide sintered article and method for production thereof. U.S. Patent 6 825 144, Nov. 2004.

[229] Morales JR, Amos N, Khizroev S, *et al*. Magneto-optical Faraday effect in nanocrystalline oxides. *J Appl Phys* 2011, **109**: 093110.

[230] Snetkov IL, Yakovlev AI, Permin DA, *et al*. Magneto-optical Faraday effect in dysprosium oxide (Dy_2O_3) based ceramics obtained by vacuum sintering. *Opt Lett* 2018, **43**: 4041–4044.

[231] Yakovlev A, Snetkov I, Permin D, *et al*. Faraday rotation in cryogenically cooled dysprosium based (Dy_2O_3) ceramics. *Scripta Mater* 2019, **161**: 32–35.

[232] Slezák O, Yasuhara R, Vojna D, *et al*. Temperature-wavelength dependence of Verdet constant of Dy_2O_3 ceramics. *Opt Mater Express* 2019, **9**: 2971–2981.

[233] Zhou D, Li XH, Wang T, *et al*. Fabrication and magneto-optical property of $(Dy_{0.7}Y_{0.25}La_{0.05})_2O_3$ transparent ceramics by PLSH technology. *Magnetochemistry* 2020, **6**: 70.

[234] Aung YL, Ikesue A, Yasuhara R, *et al*. Magneto-optical Dy_2O_3 ceramics with optical grade. *Opt Lett* 2020, **45**: 4615–4617.

[235] Hu DJ, Liu X, Liu ZY, *et al*. Fabrication of Dy_2O_3 transparent ceramics by vacuum sintering using precipitated powders. *Magnetochemistry* 2020, **7**: 6.

[236] Balabanov S, Filofeev S, Kaygorodov A, *et al*. Hot pressing of Ho_2O_3 and Dy_2O_3 based magneto-optical ceramics. *Opt Mater X* 2022, **13**: 100125.

[237] Furuse H, Yasuhara R. Magneto-optical characteristics of holmium oxide (Ho_2O_3) ceramics. *Opt Mater Express* 2017, **7**: 827–833.

[238] Vojna D, Yasuhara R, Furuse H, *et al*. Faraday effect measurements of holmium oxide (Ho_2O_3) ceramics-based magneto-optical materials. *High Power Laser Sci* 2018, **6**: e2.

[239] Lu B, Cheng HM, Xu XX, *et al*. Preparation and characterization of transparent magneto-optical Ho_2O_3 ceramics. *J Am Ceram Soc* 2019, **102**: 118–122.

[240] Cheng HM, Lu B, Liu YX, *et al*. Transparent magneto-optical Ho_2O_3 ceramics: Role of self-reactive resultant oxyfluoride additive and investigation of vacuum sintering kinetics. *Ceram Int* 2019, **45**: 14761–14767.

[241] Lu B, Wu SF, Cheng HM, *et al*. Binary transparent $(Ho_{1-x}Dy_x)_2O_3$ ceramics: Compositional influences on particle properties, sintering kinetics and Faraday magneto-optical effects. *J Eur Ceram Soc* 2021, **41**: 2826–2833.

[242] Balabanov SS, Filofeev SV, Ivanov MG, *et al*. Self-propagating high-temperature synthesis of $(Ho_{1-x}La_x)_2O_3$ nanopowders for magneto-optical ceramics. *Heliyon* 2019, **5**: e01519.

[243] Balabanov S, Demidova K, Filofeev S, *et al*. Influence of lanthanum concentration on microstructure of $(Ho_{1-x}La_x)_2O_3$ magneto-optical ceramics. *Phys Status Solidi B* 2020, **257**: 1900500.

[244] Balabanov S, Filofeev S, Ivanov M, *et al*. Fabrication and characterizations of holmium oxide based magneto-optical ceramics. *Opt Mater* 2020, **101**: 109741.

[245] Hu DJ, Li XY, Snetkov I, *et al*. Fabrication, microstructure and optical characterizations of holmium oxide (Ho_2O_3) transparent ceramics. *J Eur Ceram Soc* 2021, **41**: 759–767.

[246] Balabanov S, Filofeev S, Ivanov M, *et al*. Fabrication and characterizations of erbium oxide based optical ceramics. *Opt Mater* 2020, **101**: 109732.

[247] Yakovlev A, Balabanov S, Permin D, *et al*. Faraday rotation in erbium oxide based ceramics. *Opt Mater* 2020, **101**: 109750.

[248] Kruk A. Optical and structural properties of arc melted Ce or Pr-doped Y_2O_3 transparent ceramics. *Ceram Int* 2017, **43**: 16909–16914.

[249] Kruk A, Ziewiec K. Preparation, characterization and magneto-optical properties of Sm-doped Y_2O_3 polycrystalline material. *Micromachines* 2022, **13**: 2254.

[250] Kruk A. Impact of Sm ions on microstructure and

magneto-optical effects of Y_2O_3 ceramics obtained by arc plasma melting. *J Phys Conf Ser* 2022, **2407**: 012009.

[251] Tong YP, Xue PP, Jian FF, *et al*. Preparation and characterization of $Y_2Zr_2O_7$ nanocrystals and their photocatalytic properties. *Mater Sci Eng B-Adv* 2008, **150**: 194–198.

[252] Clarke DR, Phillpot SR. Thermal barrier coating materials. *Mater Today* 2005, **8**: 22–29.

[253] Kumar M, Raj IA, Pattabiraman R. $Y_2Zr_2O_7$ (YZ)–pyrochlore based oxide as an electrolyte material for intermediate temperature solid oxide fuel cells (ITSOFCs)—Influence of Mn addition on YZ. *Mater Chem Phys* 2008, **108**: 102–108.

[254] Ji YM, Jiang DY, Shi JL. $La_2Hf_2O_7$:Ti^{4+} ceramic scintillator for X-ray imaging. *J Mater Res* 2005, **20**: 567–570.

[255] Wang ZJ, Zhou GH, Zhang JA, *et al*. Effect of Gd content on luminescence properties of Eu^{3+}-doped $La_{2-x}Gd_xZr_2O_7$ transparent ceramics. *J Am Ceram Soc* 2015, **98**: 2476–2479.

[256] He ZS, Zhang KB, Xue JL, *et al*. Self-propagating chemical furnace synthesis of nanograin $Gd_2Zr_2O_7$ ceramic and its aqueous durability. *J Nucl Mater* 2018, **512**: 385–390.

[257] Wang XJ, Xie JJ, Wang ZJ, *et al*. Fabrication and properties of $Y_2Ti_2O_7$ transparent ceramics with excess Y content. *Ceram Int* 2018, **44**: 9514–9518.

[258] Sibille R, Lhotel E, Ciomaga Hatnean M, *et al*. Coulomb spin liquid in anion-disordered pyrochlore $Tb_2Hf_2O_7$. *Nat Commun* 2017, **8**: 892.

[259] Kang JB, Xu WM, Zhang WH, *et al*. Growth and magneto-optical characteristic of $Ho_2Ti_2O_7$ crystal. *J Cryst Growth* 2014, **395**: 104–108.

[260] Kang JB, Fang ZX, Chen X, *et al*. Effect of oxygen vacancy concentration on the absorption spectra of $Dy_2Ti_2O_7$ crystal. *J Alloys Compd* 2014, **599**: 170–174.

[261] Gardner JS, Gaulin BD, Paul DM. Single crystal growth by the floating-zone method of a geometrically frustrated pyrochlore antiferromagnet, $Tb_2Ti_2O_7$. *J Cryst Growth* 1998, **191**: 740–745.

[262] Guo FY, Sun YL, Yang XS, *et al*. Growth, Faraday and inverse Faraday characteristics of $Tb_2Ti_2O_7$ crystal. *Opt Express* 2016, **24**: 5734–5743.

[263] Guo FY, Zhang WH, Ruan M, *et al*. Czochralski growth of $Gd_2Ti_2O_7$ single crystals. *J Cryst Growth* 2014, **402**: 94–98.

[264] Andrievskaya ER. Phase equilibria in the refractory oxide systems of zirconia, hafnia and yttria with rare-earth oxides. *J Eur Ceram Soc* 2008, **28**: 2363–2388.

[265] Yasuhara R, Ikesue A. Magneto-optic pyrochlore ceramics of $Tb_2Hf_2O_7$ for Faraday rotator. *Opt Express* 2019, **27**: 7485–7490.

[266] Aung YL, Ikesue A, Yasuhara R, *et al*. Optical properties of improved $Tb_2Hf_2O_7$ pyrochlore ceramics. *J Alloys Compd* 2020, **822**: 153564.

[267] Zhang LX, Li XY, Hu DJ, *et al*. Transparent non-stoichiometric $Tb_{2.45}Hf_2O_{7.68}$ magneto-optical ceramics with high Verdet constant. *Scripta Mater* 2021, **204**: 114158.

[268] Zhang LX, Li XY, Hu DJ, *et al*. Fabrication and properties of non-stoichiometric $Tb_2(Hf_{1-x}Tb_x)_2O_{7-x}$ magneto-optical ceramics. *J Adv Ceram* 2022, **11**: 784–793.

[269] Zhang LX, Li XY, Hu DJ, *et al*. Fabrication and properties of transparent $Tb_2Ti_2O_7$ magneto-optical ceramics. *J Eur Ceram Soc* 2021, **41**: 7208–7214.

[270] Lai YQ, Lu B, Wang M. Optical properties and Faraday magneto-optical effects of highly transparent novel $Tb_2Zr_2O_7$ fluorite ceramics. *Scripta Mater* 2023, **227**: 115282.

[271] Hu LB, Lu B, Xue BW, *et al*. Production and characterization of highly transparent novel magneto-optical $Ho_2Zr_2O_7$ ceramics with anion-deficient fluorite structures. *J Mater Sci Technol* 2023, **150**: 217–224.

[272] Che JW, Wang XZ, Liu XY, *et al*. Thermal transport property in pyrochlore-type and fluorite-type $A_2B_2O_7$ oxides by molecular dynamics simulation. *Int J Heat Mass Tran* 2022, **182**: 122038.

[273] Ikesue A, Aung YL. Origin and future of polycrystalline ceramic lasers. *IEEE J Sel Top Quant* 2018, **24**: 1601507.

[274] Ikesue A, Aung YL. Ceramic laser materials. *Nat Photonics* 2008, **2**: 721–727.

Open Access This article is licensed under a Creative Commons Attribution 4.0 International License, which permits use, sharing, adaptation, distribution and reproduction in any medium or format, as long as you give appropriate credit to the original author(s) and the source, provide a link to the Creative Commons licence, and indicate if changes were made.

The images or other third party material in this article are included in the article's Creative Commons licence, unless indicated otherwise in a credit line to the material. If material is not included in the article's Creative Commons licence and your intended use is not permitted by statutory regulation or exceeds the permitted use, you will need to obtain permission directly from the copyright holder.

To view a copy of this licence, visit http://creativecommons.org/licenses/by/4.0/.